THE UNIVERSITY OF MICHIGAN
COLLEGE OF LITERATURE, SCIENCE, AND THE ARTS
Department of Physics

Final Report

IONIZED MERCURY GAS IN THE HEATED SHOCK TUBE: THE MEASUREMENTS OF RELAXATION TIMES AND ABSOLUTE INTENSITIES

Yong Wook Kim
Otto Laporte, Project Director

ORA Project 01095

under grant from:

AIR FORCE OFFICE OF SCIENTIFIC RESEARCH
GRANT NO. AF-AFOSR-934-67
ARLINGTON, VIRGINIA

administered through:

OFFICE OF RESEARCH ADMINISTRATION ANN ARBOR

August 1968

ACKNOWLEDGEMENTS

The author wishes to express his deepest gratitude to Professor Otto Laporte for his inspiring guidance throughout the entire course of this research with encouragements as well as criticisms. The advice given by Professors E. E. Hucke, H. Merte, Jr., and D. Sinclair in the initial phase of the shock tube construction is gratefully acknowledged. The author wishes to thank his colleague, M. John Yoder, for his help and advice in many different phases of this research.

To William A. Brown and James R. Roberts go special thanks for giving the benefit of their experiences with the shock tube spectroscopy. The able assistance of Patricia Petraitis, John Brimm, and H. Michael Macksey is greatly appreciated. Thanks goes also to Mrs. Pruim for her careful typing of the final copy of the manuscript.

The author wishes to thank the United States Air Force, Office of Scientific Research for its generous financial support of the research.

TABLE OF CONTENTS

TABLE OF CONTENTS (continued)

LIST OF TABLES

LIST OF FIGURES

LIST OF FIGURES (continued)

ABSTRACT

A heated shock tube has been constructed as a new fluid-dynamical device, in order to study strong shocks in the mercury gas, to investigate the relaxation phenomenon in thermally ionized mercury via shock heating, and to utilize the shock tube flow as a spectroscopic source for the measurement of atomic constants of metallic elements.

Extensive theoretical calculations of the Rankine-Hugoniot relation in mercury and mercury-neon mixtures have been performed for a wide range of shock strengths, extending far beyond the scope of heated shock tube. Two stages of ionization are fully considered in the calculations. Various partition functions and degrees of ionization as well as the equation of state in ionized mercury gas have also been calculated for temperatures from 5,000° to 30,000 °K, all irrespective of shock relations.

A performance study of the heated shock tube has been made with shocks in mercury and mercury-neon mixtures. The usual discrepancy between the ideal shock tube theory and the observed shock strength has been noticed in the heated shock tube. A novel observation of the reflected shock bifurcation in the monatomic gas of mercury has been made, and a detailed quantitative analysis of bifurcated shocks is presented. A " γ-model" of the reflected shock bifurcation in monatomic gases is proposed and the criterion for the disappearance of the bifurcation discussed.

The approach toward ionization equilibrium has been investigated by measuring the ionizational relaxation times. The activation energy of ionization in shocked mercury gas is determined and is found to coincide with the resonance energy of neutral mercury in the temperature regime of 7,300° to 11,000 °K. The important mechanism in achieving the ionization equilibrium is shown to be a two-step process of electron-atom collisions in the electron density regime where the present measurements are made. It is demonstrated that the heated shock tube is particularly suitable for this type of investigation.

The absolute gf-values have been determined in the heated shock tube for 37 neutral mercury lines, using the method of "curves of growth". Photographic photometry has been employed for absolute intensity measurements. Modified high speed photographic photometry has been devised, which can be used in the spectral region of $\lambda < 2800$ Å. It is shown that many other metallic elements can be worked on with relative ease for similar measurements.

Related future researches are suggested.

CHAPTER I

INTRODUCTION

1. Shock Tube Spectroscopy—A Historical Note

The shock tube is a fluid-dynamical device which basically consits of two or more chambers separated by means of one or more diaphragms. The chambers are assembled in such a manner that their longer axes are lined up along a straight line. The characteristic width of a chamber is substantially smaller than its length. The chambers are filled with the same gas or gases of different kinds. The pressure in a chamber at one end is much higher than in other chambers. In order to generate a sequence of shocks and rarefaction waves of interest, one would cause the diaphragm(s) to rupture by suitable means.

The origin of the shock tube goes back to 1899 when Vieille[1] observed that the compression wave generated by breaking a diaphragm separating two chambers containing gases of different pressures travels with a speed greater than the local sound speed. Many different versions of the shock tube came into general use with varying purposes during and after World War II. Its use ranged from the investigation of supersonic flow patterns past various models within the tube[2] to studies of the structure of shocks[3] and of the boundary layer growth in uniform flow,[4] and even to the calibration of pressure measuring devices.[5] Developments of optical techniques[6] such as shadowgraph, schlieren system, and interferogram; of high speed photography by means of the

rotating drum camera[7] and pulsed light source of submicrosecond rise time[8]; and of various electronic counter chronographs all helped to bring shock tube research into the realm of exact science.

A decisive turning point in the research came about in 1952 when Laporte and associates[9] at The University of Michigan observed a "faint yellow flash" in a two chamber shock tube of constant rectangular cross section (2" x 7")*, which turned out to be due to a moderately strong shock in nitrogen. At the same time two other independent groups reported similar observations, one at Cornell University under the direction of Kantrowitz[10] and the other by Shreffler and Christian[11] at the Los Alamos Scientific Laboratory.

The one-dimensional flow in a shock tube of constant cross section is shown in the x-t-p diagram of Fig. 1. At the time $t = t_o$ the expansion and compression tubes are filled to pressures of p_o and p_c, respectively, where $p_o \ll p_c$. From the instant of the bursting of the diaphragm, there develops a rarefaction moving from the diaphragm position into the compression tube, its pressure profile being a smooth curve between p_c and p_1 as shown for $t = t_1$. As a

---

*From this point on we will deal exclusively with two chamber shock tubes of constant rectangular cross section.

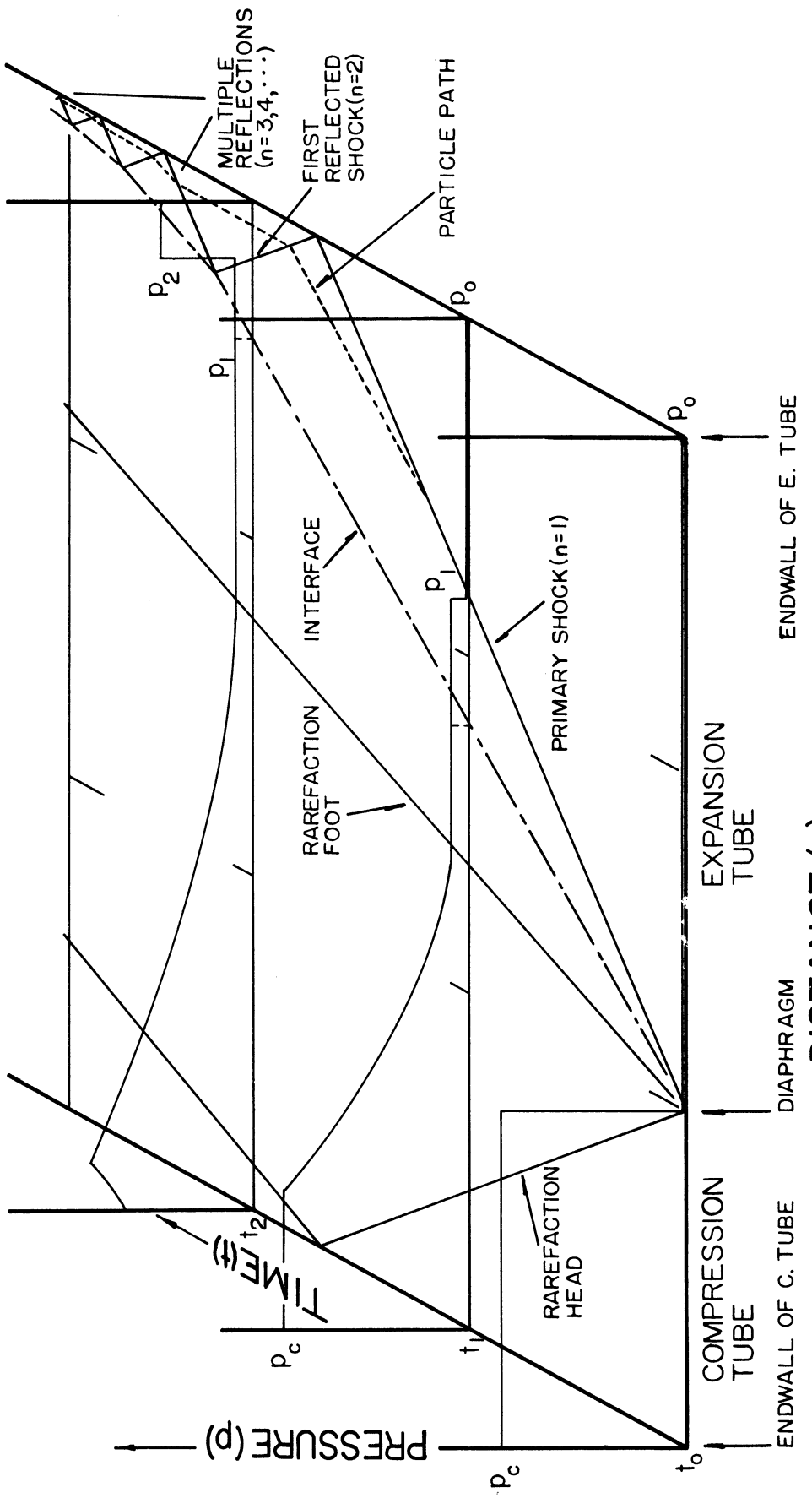

Figure 1. x-t-p diagram

result, an interface between the gases which were originally on either side of the diaphragm moves at high speed into the expansion tube. As it moves it pushes the gas in the expansion tube as a piston would. A primary shock is then generated in the form of a compression front traveling into the gas contained in the expansion tube. The shock is a discontinuity in pressure, density, and temperature, moving supersonically followed by the gas at high speed. The interface, on the other hand, is a discontinuity surface in density and temperature but not in pressure, since the gas ahead of it is shock-compressed and consequently heated, while the gas behind it has been expanded and cooled, both resulting in one pressure, p_1. Both the rarefaction head and the primary shock proceed toward either end of the shock tube and are reflected. The effect of respective reflections on the pressure distribution is seen in the plot of pressure distribution at $t = t_2$. The reflected shock will again undergo reflection at the interface. In this manner multiple reflections take place between the interface and endwall.*

It is this region of reflected shocks that was responsible for the observed luminosity mentioned earlier. In 1953, Turner[12] at Michigan built a so-called "luminous shock tube" (inner cross section 2.625" x 1.625") expressly for the

---

* As the reflected shock meets the interface to undergo its second reflection, also a shock will be transmitted into the cold gas.

strong shocks, and investigated such problems as spectral line broadening of H_β in partially ionized hydrogen-neon mixtures and ionizational relaxation in shocked xenon. Turner's investigation established a few noteworthy facts, which now characterize shock tube spectroscopy. They are the following: i) the luminosity in the shock tube is due to the spectral emission of the shocked medium, although impurities from the walls and in the gas will also contribute; ii) the boundary layer growth behind the strong shock is not severe enough to complicate the optical uniformity of the shocked zone, if the medium is of noble gases*; iii) it is, in fact, possible to obtain high temperature gas in a local thermodynamic equilibrium, which may last as long as one hundred microseconds; and iv) strong shocks can produce temperatures as high as 18,000 ^{o}K in the region of reflected shocks. The third point together with the fact that thermodynamic variables of shocked gases can be adequately evaluated by well-established shock theory[13] constitutes the basis essential for quantitative spectroscopy, and establishes the pressure driven shock tube as a spectroscopic source.

Doherty[14] at Michigan developed a program of measuring oscillator strengths of spectral lines of gaseous elements by applying the astrophysical method of "curves of growth" to shock-tubery. Wilkerson[15] and Charatis[16] refined the method and extended it to the measurement of similar quantities for metallic elements by introducing them into shocked

---

* See Chapter III for a detailed description.

neon via metallo-organic compounds evaporable at room temperature. They also produced much experimental evidence indicating the success of the shock theory, e.g., in providing level populations, by using methods of pressure transducers and spectral line reversal. Brown[17] further elaborated the technique involving metallo-organic compounds as additives, aided by a simple scheme of measuring electron pressures based upon the calculated H_β line profile.[18]

Following the work of Turner, some metallic elements have been introduced in the shocked zone by suspending powdered solid compounds near the test section. This method is widely used, especially for the quantitative study of molecular spectra.[19]

2. Heated Shock Tube*

The observation of shock luminosity described in the previous section actually did not come as a total surprise because of the existence of a one-dimensional ideal shock tube formula developed by Geiger and Mautz,[2] using earlier developments by Schardin[20] and by Taub.[5] This formula relates the initial pressure ratio p_c/p_o to the shock strength p_1/p_o:

---

* The heated shock tube was conceived by Laporte far back in 1958, specifically for the study of shocks in mercury gas. For this reason, it used to be called the "mercury shock tube" in the earlier stages of present undertaking.

$$\frac{p_c}{p_o} = \frac{p_1}{p_o}\left[1 - \frac{s_o}{s_c}\frac{\mu_o - 1}{\mu_c - 1}\frac{(p_1/p_o - 1)}{\sqrt{(\mu_o + 1)(\mu_o p_1/p_o + 1)}}\right]^{-(\mu_c+1)} \quad (I.1)^{21} \ *$$

where $\mu = (\gamma + 1)/(\gamma - 1)$. Subscripts o and c refer to the gases in the expansion and compression tubes at $t = t_o$, respectively. s stands for the sound speed in the gas and γ the specific heat ratio. Note that μ equals 4 for monatomic gases and 6 for diatomic gases at room temperature.

Equation (I.1) states that for a given combination of the driving and driven gases, a stronger shock can be obtained the greater the initial pressure ratio, p_c/p_o. This notion, however, has only a limited usefulness because p_1/p_o is a very slow function of p_c/p_o. p_c can not be made indefinitely large due to the technical limit in the structural strength of the compression tube and accessories, and p_o must not be too small or the duration of the shocked zone will be too short to be of any value.

For a given pressure ratio, p_c/p_o, on the other hand, a stronger shock can be produced the lower the sound speed in the shocked gas. For attaining strong and high temperature shocks, the best driving gas is obviously hydrogen. Helium is commonly used as driving gas also. Neon, argon, krypton, and xenon proved to be acceptable as driven gas because they

---

* Taub's relation predicts p_1/p_o consistently too large roughly by a factor of 2, where p_1/p_o of actual primary shocks are measured mostly about three meters downstream from the diaphragm positions. See Chapter III.

all are monatomic gases,* heavy, and readily available. Shock strengths in respective gases increase in the order of atomic weight. (See Table I.)

As was stated by earlier investigators, especially by Turner, the temperature attainable in an ordinary luminous shock tube is limited to about 18,000 ^{o}K, even with the best combination of gases dealt with thus far and the pressure ratio. This temperature limit of course refers to the region of multiply reflected shocks. It would be, however, highly desirable to have in a shock tube a high density plasma in a local thermodynamic equilibrium at a temperature far above 20,000 ^{o}K behind the first reflected shock, especially now that other plasmas of medium densities and higher temperatures (as high as 10^{5} ^{o}K) such as those in the electric shock tube** are being severely challenged over the question of local thermodynamic equilibrium. This directed our attention to mercury gas as a shock medium. Mercury is much

---

* In order to minimize the boundary layer growth in the hot flow behind the primary shock, the driven gas must be of monatomic molecules or at least dominated by monatomic gases. For detailed discussion, see Chapter III.

** The electric shock tube was invented by R. G. Fowler[23] at The University of Oklahoma back in 1952, elaborated by many investigators,[24,25] and is known to effectively produce highly ionized gases at low pressures. The shock (?) in the tube moves at a speed as high as a few cm/μsec, but lacks a bearing to the shock theory.[25] There is a growing opinion that the shock is not entirely responsible for the plasma in the electric shock tube and the plasma may not be in a local thermodynamic equilibrium at all,[26,27] in spite of the fact that there are a great number of investigators who explosively claimed otherwise.[28,29]

heavier than those inert gases (Table I), a practically monatomic gas, and the boiling point of liquid mercury is reasonably low. At low temperatures, mercury vapor of course consists of diatomic molecules of mercury, but the dissociation potential of Hg_2 is so small (less than 0.06 eV[22]) that it decomposes fully into mercury atoms above room temperature. Numerical calculations show that the temperature of mercury gas behind the primary shock can be as high as 18,000 ^{o}K within the limit of laboratory practice (see Chapter II). Table I compares various monatomic gases.

Table I

Atomic Constants of Monatomic Gases

Element i	At. No. A_i	At. Weight* i	Ionization Potential (eV)** χ_{iI}	iII	χ_{iIII}	χ_{iIV}
Ne	10	20.183	21.559	40.96	63.43	96.90
A	18	39.944	15.736	27.62	40.68	61
Kr	36	83.80	13.996	26.5	36.94	68
Xe	54	131.30	12.127	21.20	32.12	~46
Hg	80	200.61	10.434	18.75	34.5	~72

It is quite clear now that the shock tube must be heated if mercury gas is to be used as a shock medium.

---

* Handbook of Chemistry and Physics 44th edition (1963); based on 1959 International Unit of O_2 = 16.000.

** Coincidence Table for Atomic Spectroscopy, Edited by Kubor, et. al. (Elsevier Publishing Co., Amsterdam, 1965)

Saturated vapor pressures of mercury are tabulated up to its critical temperature in Table II. The tube temperature of 200° to 400 °C turns out to be suitable for dealing with shocks in mercury gas, noting the fact that p_o must lie in the vicinity of one cm Hg or greater in order to have an appreciably long duration of the shock luminosity and at the

Table II

Vapor Pressure and Critical Data of Mercury

T °C	$P_{sat.\ vap.}$ cm Hg	T °C	$P_{sat.\ vap.}$ cm Hg
0	1.85×10^{-5} *	400	1.611×10^{2} ***
50	1.267×10^{-3} *	500	6.351×10^{2} ***
100	2.729×10^{-2} *	600	1.828×10^{3} ***
150	2.807×10^{-1} *	800	8.158×10^{3} ***
200	1.7287 *	1,000	2.386×10^{4} ***
250	7.4405 **	1,200	5.111×10^{4} ***
300	2.474×10^{1} **	1,400	9.121×10^{4} ***

M. P. = -38.87 °C, * B. P. = 356.58 °C *

Critical Temperature = 1,490 ± 15 °C ***

Critical Pressure = $(1.13 \pm 0.02) \times 10^{5}$ cm Hg ***

---

* Handbook of Chemistry and Physics, 44th Edition (Chemical Rubber Publishing Co., Cleveland, Ohio, 1963).

** Spedding, F. H. and Dye, J. L., J. Phys. Chem. 59,581 (1955).

*** Heusel, F. and Franck, E. H., Ber. Bunsenges. Phys. Chem. 70,1154 (1966).

same time p_o must be substantially smaller than the saturated vapor pressure so as not to complicate the situation through van der Waals correction.[30]

Speaking of a metallic element as a shock medium, it should be pointed out that the technique of using metallo-organic compounds as additives has a definite drawback in that since these compounds are usually unstable, it is often questionable how much metal is actually present in the shocked zone. On the other hand, the heated shock tube could handle directly as additives a number of metallic elements such as cesium, cadmium, sodium, and potassium besides mercury for spectroscopic measurements.

Extensive baking of the entire tube helps reduce the impurity level on the inner wall of the tube and make the mechanism of collisional excitation behind the shock front simpler. This turned out to be a very significant contribution (see Chapters III and IV).

The construction of the heated shock tube at The University of Michigan began in June, 1965, and was completed at the end of 1966, followed by a few months' debugging efforts. Preliminary observations were reported to the 6th International Symposium on Shock Tubes, Freiburg, Germany, in March, 1967.[31] Initial constructional details are described in a report to the U. S. Air Force Office of Scientific Research.[30]

3. Outline of the Dissertation.

The general theory of shock is described in Chapter II. The internal dissipative processes in the shocked gas, such as the ionization, are extensively discussed. Calculational schemes involving strongly ionized gases are suggested for three representative types of shock media—namely, one-component monatomic gas, two-component monatomic gas, and mixtures of monatomic and polyatomic gases. Numerical calculations for shocked mercury and neon-mercury mixtures are summarized in the last section.

In Chapter III a brief description of the heated shock tube is given, together with that of accompanying equipment. Fluid-dynamical observations of strong shocks in mercury gas are described. A bifurcation of the reflected shock in a monatomic gas is observed for the first time and its connection with the boundary layer growth is discussed in detail. A theoretical model of shock bifurcation in monatomic gases, which we will call the "γ-model", is proposed and its generalization to gases other than mercury considered. A possible method of removing the shock bifurcation in the regime of very strong shocks in monatomic gases is suggested, based upon the γ-model.

The ionizational relaxation in shocked mercury gas is discussed in Chapter IV. Measured relaxation times (τ) are plotted as a function of temperature, and are related to the resonance energy. The comparison with available data for argon, krypton, cesium, and xenon is made. The influence

of impurities upon the radiation level from the shocked gas is discussed in the light of measurements showing that radiation overshoot is absent when the tube is baked thoroughly.

In Chapter V, measurements of oscillator strengths of neutral mercury lines are described. Measurements are made for 37 lines of neutral mercury which range from 2537 A^{o} to 5491 A^{o}, using the method of curves of growth. To measure the absolute intensity of far ultraviolet lines a somewhat modified photographic technique had to be used.

Results of our investigations on ionized mercury gas are summarized in Chapter VI and related future researches are proposed.

CHAPTER II

THEORY OF SHOCK

1. Introduction

The formation of a plane shock does not take place in the immediate neighborhood of the diaphragm due to a finite time of diaphragm opening and to the attenuation of shock for reasons which will be discussed later. The plane primary shock emerges when the attenuation diminishes a few feet downstream from the diaphragm, with speed nearly constant but now substantially smaller than predicted from the ideal shock tube formula of eq. (I.1).

Let us turn our attention to this plane shock after it has reached the approximately constant speed regime. Experimental observations of strong shocks indicate that there exist steady-state flows behind the shock front and that the influence of the growing boundary layer on thermodynamic variables of respective flows is small within a limited region of observation. This renders possible the treatment of the shock tube flow as a one dimensional steady-state problem in a non-viscous fluid, — an approximation which promises to have a potential merit of simplicity.[13]

The shock transition from a state of low pressure and low temperature to another of high pressure and high temperature is governed by the conservation laws of mass, momemtum, and energy[32]: across the shock front

$$\rho v = \text{const.} \tag{II.1}$$

$$\rho v^2 + p = \text{const.} \tag{II.2}$$

$$\rho v \left(h + \tfrac{1}{2} v^2\right) = \text{const.} \tag{II.3}$$

where the specific enthalpy, h, is

$$h = e + p/\rho \tag{II.4}$$

ρ, v, p, and e are the density, the flow velocity in the local coordinate system fixed to the shock front, the hydrostatic pressure, and the specific internal energy. The equation of state

$$p = n\, k\, T \tag{II.5}$$

where n, k, and T are the particle number density, Boltzmann constant, and the temperature, respectively. If n were a constant, or if the gas particle had no internal degrees of freedom, eq.'s (II.1) to (II.5) would be sufficient to determine the numberical values of the variables behind the shock in terms of those in front. Since in all practical cases this is not so, the following developments are necessary.

At temperatures above 5,000 ^{o}K, which a weaker shock of our interest is capable of generating, most gases are internally excited. Therefore all real gas effects must be fully taken into account. Let us consider the specific internal energy of a general shock medium which consists of several different gases of varying degrees of freedom and define an effective molecular weight, σ, by

$$\sigma \equiv \sum_i \sigma_i \eta_i \quad , \quad \sum_i \eta_i = 1 \tag{II.6}$$

where σ_i is the molecular weight of the i^{th} species and η_i its fractional abundance (by particle number densities). Then

$$e = e_T + e_R + e_V + e_E + e_D$$
$$= \frac{N^o kT}{2\sigma} \sum_i \left(f_{Ti} + f_{Ri} + f_{Vi} + f_{Ei} \right) + \sum_i \chi_i \alpha_i \delta_i \qquad \text{(II.7)}$$

where f_{Ti}, f_{Ri}, f_{Vi}, and f_{Ei} are the effective translational, rotational, vibrational, and electronic degrees of freedom of the i^{th} species. N^o is Avogdro's number; χ_i, α_i, and δ_i are the dissociation or ionization potential, the degree of dissociation or ionization, and the number of particles of the i^{th} species per unit mass available for dissociation or ionization, respectively. At the ambient temperature of the shock tube the vibrational and electronic degrees of freedom are not fully excited for most gases, while the translational and rotational degrees of freedom are. Therefore f_{Vi} and f_{Ei} have to be evaluated as functions of state variables by taking an ensemble average of energy levels for each mode:

$$f_{Vi} \equiv \frac{2\langle E_{Vi} \rangle}{kT} = \frac{2\,\Theta_{Vi}/T}{\exp(\Theta_{Vi}/T) + 1} \qquad \text{(II.8)}$$

$$f_{Ei} \equiv \frac{2\langle E_{Ei} \rangle}{kT} = 2T \frac{\partial}{\partial T} \ln\left(\sum_j g_{ij} e^{-E_{ij}/kT} \right) \qquad \text{(II.9)}$$

where the vibrational constant $\Theta_V = h\nu/k$, h being Planck's

constant. E_{ij} is the energy level difference (from the normal state) of the i^{th} species and g_{ij} its quantum weight.

2. Shock Relations

As described in Chapter I, the arrival of the primary shock flow at the endwall immediately generates a reflected shock, which moves upstream until it encounters the interface. Another shock reflection takes place at the interface. Many more similar shock reflections follow between the endwall and interface as the "hot region" becomes narrower and narrower. Labeling these shocks which remain on the hotter side of the interface by n = 1, 2, 3, ····· in their chronological order, one observes that eq.'s (II.1), (II.2), and (II.3) apply to each of these shocks: for nth shock

$$\rho_{n-1} v_{n-1} = \rho_n v_n \quad , \tag{II.10}$$

$$\rho_{n-1} v_{n-1}^2 + p_{n-1} = \rho_n v_n^2 + p_n \quad , \tag{II.11}$$

$$h_{n-1} + \tfrac{1}{2} v_{n-1}^2 = h_n + \tfrac{1}{2} v_n^2 \quad , \tag{II.12}$$

and

$$h_n(\rho_n, p_n) = \tfrac{1}{2} \frac{p_n}{\rho_n} (\beta_n + 1) + \tfrac{1}{2} D_n \quad , \tag{II.13}$$

where

$$\beta_n = 4 + \sum_i (f_{Ri} + f_{vi} + f_{Ei}) \eta_i \tag{II.14}$$

$$D_n = 2 \sum_i \chi_i \alpha_i \delta_i \quad . \tag{II.15}$$

The quantities with subscript (n - 1) must be known and, in fact, these establish a set of initial conditions together with the shock speed.* Equations (II.10), (II.11), and (II.12) can be solved for ρ_n/ρ_{n-1} expressed in terms of p_n/p_{n-1} by eliminating v_n, i.e.

$$\frac{\rho_n}{\rho_{n-1}} = \frac{\beta_n p_n/p_{n-1} + 1}{p_n/p_{n-1} + K_{n,n-1}} \qquad \text{(II.16)}$$

where

$$K_{n,n-1} = \beta_{n-1} - (\Delta_n - \Delta_{n-1}) \frac{\rho_{n-1}}{p_{n-1}} \qquad \text{(II.17)}$$

The equation (II.16) is generally known as the Rankine-Hugoniot relation. Eliminating ρ_n/ρ_{n-1} from equations (II.11) and (II.16) and solving for p_n/p_{n-1}, one gets

$$\frac{p_n}{p_{n-1}} = \frac{1}{2\beta_n}\left[(\beta_n - 1)(1 + r_{n-1}) + \sqrt{(\beta_n - 1)^2(1 + r_{n-1})^2 + 4\beta_n(1 + r_{n-1} - r_{n-1}K_{n,n-1})}\right] \qquad \text{(II.19)}$$

where

$$r_n = (U_{n+1} + u_n)^2 \frac{\rho_n}{p_n}, \quad u_0 = 0 \qquad \text{(II.20)}$$

U_{n+1} is the shock speed of the $(n + 1)^{th}$ shock and u_n the speed ahead of the $(n + 1)^{th}$ shock, both in the laboratory

---

* It should be noted that this treatment differs from the usual presentation of shock reflection in that e.g. for the first reflection (n = 2) the condition that the fluid be at rest is not used. Instead, the speed of the reflected shock is regarded as known through observation.

coordinate system. Therefore one can write

$$\frac{T_n}{T_{n-1}} = \left(\frac{\sigma_n}{\sigma_{n-1}}\right)\left(\frac{p_n}{p_{n-1}}\right)\left(\frac{\rho_{n-1}}{\rho_n}\right). \qquad \text{(II.20)}$$

In view of the fact that quanties such as β_n and $K_{n,n-1}$ appearing as they do on the right hand sides of eq.'s (II.16) and (II.18) call for the knowledge of the n^{th} state variables, it seems almost inevitable to achieve the evaluation of the n^{th} state variables from the (n - 1)th state variables by means of an iterative process between eq.'s (II.16), (II.18), and (II.20).

It has to be pointed out that the role of the measured shock speed in the success of the theory is very vital because any fluid-dynamical non-ideality in the shock tube flow is strongly indicated in this quantity once the plane shock is formed some distance away from the burst diaphragm. For instance, the attenuation of the shock, which is caused by the leakage of the shocked gas into the region behind the interface through the boundary layers, does not complicate matters because it is then closely monitored by the measured shock speed at a specific point of observation. Furthermore, any non-uniformity in the flow field near the endwall into which a reflected shock peneratrates will result in a systematic variation in shock speed.

One obvious underlying assumption throughout the development is that there exists a local thermodynamic equilibrium behind the shock, which in essence states that the collisional processes establish the Maxwellian

distribution in each ensemble of various modes of the shocked gas. In coming to the state of local thermodynamic equilibrium, the complex system of shocked gas undergoes several stages of relaxation: the translational relaxation emerges in about 0.01 μsec after the passage of the shock front,[33] followed by the rotational and vibrational relaxations if these modes are present in the gas. Concurrently to the vibrational relaxation there comes the dissociation, and finally the ionizational relaxation together with the relaxation in the electronic mode takes place. In the crudest approximation it can be said that the characteristic time of each relaxation is governed by the inherent energy associated with each mode.

One can readily anticipate that the fully-relaxed translational temperature of the gas immediately behind the shock front is much higher than the equilibrium temperature. In fact, this translational temperature can be predicted from eq.'s (II.16) through (II.20) if one neglects all those internal structure dependent terms. This temperature gradually decreases as the translational energy is pumped into various internal modes until the complete local thermodynamic equilibrium is established. Other thermodynamic variables go through similar readjustments during the entire period of relaxation.

It becomes self-evident that any experimental measurement which calls for the advantage of the shock theory should be performed well synchronized to the region of local

thermodynamic equilibrium.

3. Ionization Equilibrium

A) Law of mass action[34]

Let us consider a very general reaction in the form of

$$\sum_i \nu_i A_i = 0 \qquad \text{(II.21)}$$

where A_i is the i^{th} reactant and ν_i the number of molecules of the i^{th} reactant necessary to complete one reaction. In an equilibrium one observes that the specific thermodynamic potential at given pressure and temperature tends to be a minimum, i.e., the thermodynamic potential (the Gibbs free energy)

$$\varphi = h - Ts$$

satisfies the extremum conditions

$$\sum_i \frac{\partial \varphi}{\partial n_i} \frac{dn_i}{dn_j} = 0 \quad , \quad j = 1, 2, \cdots i \qquad \text{(II.22)}$$

where n_i is the number of i^{th} particles, say, per unit volume participating in the reaction and s the specific entropy. From the constraint conditions (II.21), one gets

$$\frac{dn_i}{dn_j} = \frac{\nu_i}{\nu_j}$$

to arrive at

$$\sum_i \frac{\partial \varphi}{\partial n_i} \frac{\nu_i}{\nu_j} = 0 \quad \text{or} \quad \sum_i \mu_i \nu_i = 0 \qquad \text{(II.23)}$$

where the chemical potential of the i^{th} species

$$\mu_i \equiv \frac{\partial \varphi}{\partial n_i} .$$

For a multicomponent system, one may write out the canonical ensemble partition function in the following form:

$$Q = \prod_i \frac{(Z_i')^{n_i}}{n_i!} , \tag{II.24}$$

where the partition function for an isolated particle of a microcanonical ensemble is given by

$$Z' = Z_T \, Z_R \, Z_V \, Z_E, \tag{II.25}$$

the index T standing for translation, etc.

The specific chemical potential can be deduced from Q, i.e.,

$$\mu_i = -kT \frac{\partial}{\partial n_i} \ln Q$$

$$\cong -kT \frac{Z_i'}{n_i} , \tag{II.26}$$

where Stirling's approximation is used because n_i is large. Substituting (II.26) in (II.23), one gets

$$\sum_i \ln \left(\frac{Z_i'}{n_i}\right)^{\nu_i} = 0 . \tag{II.27}$$

Now we turn to the specific reaction of interest, namely, thermal ionization. Denoting the neutral atom by AI and its first ion by AII, we have for the first stage of ionization taking place in the system of a heavy monatomic gas

$$AI \overset{\chi_{AI}}{\rightleftharpoons} AII + e .$$

One can identify the quantities in (II.21) as below:

$$A_1 = AI,\ A_2 = AII,\ A_3 = e$$

$$\nu_1 = 1,\ \nu_2 = -1,\ \nu_3 = -1\ .$$

For the first ionization the equation (II.27) reduces to

$$\frac{n_{AII}\, n_e}{n_{AI}} = \frac{(Z_T)_e\,(Z_E)_{AII}\,(Z_E)_e}{(Z_E)_{AI}}\ , \qquad \text{(II.28)}$$

since if $m_{AI} = m_{AII}$,

$$(Z_T)_{AI} = (Z_T)_{AII} = \left(\frac{2\pi m_A kT}{h^2}\right)^{3/2}\ .$$

Note that the volume has been taken to be unity for convenience. m_A stands for the nuclear mass of the species A. Likewise for the second ionization one can write out

$$\frac{n_{AIII}\, n_e}{n_{AII}} = \frac{(Z_T)_e\,(Z_E)_{AIII}\,(Z_E)_e}{(Z_E)_{AII}} \qquad \text{(II.29)}$$

and so forth. Let the discussion be limited, however, to only two stages of ionization in view of the probable temperature range in the shock tube. In equilibrium the relations (II.28) and (II.29) should hold true simultaneously.

The electronic partition function of isolated atomic or ionic species ($(Z_E)_{AI}$, $(Z_E)_{AII}$, $(Z_E)_{AIII}$, etc.) diverges due to the convergence of the discrete states toward the ionization potential. But in the presence of neighboring particles, charged or neutral, the upper states near the ionization potential merge into the continuum because of

various perturbing mechanisms, the most significant being the Stark effect, resulting in the lowering of ionization potential and, in turn, in the finite partition functions. In the system of an ionized gas where the average number of electrons per Debye sphere is less than one, the extent of lowering of ionization potential is best expressed by the Debye-Hückel formula

$$\Delta\chi_z = \frac{(z+1)e^2}{\rho_D} , \quad \rho_D = \sqrt{\frac{kT}{4\pi e^2\left(n_e + \sum_i z^2 n_{i,z}\right)}} , \tag{II.30}$$

taking, of course, the Stark effect as the major mechanism of perturbation. ρ_D is the Debye radius and z = 0, 1, 2,$\cdots$ for the neutral atoms, singly ionized ions and so forth, respectively (or according to spectroscopic notation, z = I, II, III, $\cdots$). See Appendix A for more discussions on various models for the lowering of ionization potential.

Now we define a function, $F_{i,z}(p,t)$ by

$$F_{i,z}(p,T) \equiv kT \frac{(Z_T)_e (Z_E)_{i,z+1} (Z_E)_e}{(Z_E)_{i,z}}$$

$$= 2kT\left(\frac{2\pi m_e kT}{h^2}\right)^{3/2} \frac{(Z_E^\circ)_{i,z+1}}{(Z_E^\circ)_{i,z}} e^{-\frac{\chi^*_{i,z}}{kT}} , \tag{II.31}$$

where the zero point of the energy scale in each partition function is taken at the ground state of each atomic or ionic species and each partition function is labeled so by the superscript $^\circ$. Notice that $(Z_E)_e = 2$. m_e stands for

the electron mass. The pressure dependence of $F_{i,z}(p,t)$ is, of course, indirect and rather weak, coming from the lowering of ionization potential. Here

$$\chi_{i,z}^{*} = \chi_{i,z} - \Delta\chi_{z} \quad . \tag{II.32}$$

From now on, and for the sake of simplicity, the notation will be simplified by writing $Z_{i,z}$ for $(Z^{o}_{E})_{i,z}$ unless otherwise stated.

The numerical evaluation of relations (II.28) and (II.29) needs some further elaboration with a few specific examples because the method of calculation may depend on the type of mixture of gases.

B) Ionization equilibrium in one-component monatomic gas

We define the degrees of first and second ionizations of the species A by

$$\alpha_{A1} \equiv \frac{n_{AII} + n_{AIII}}{n_{AI} + n_{AII} + n_{AIII}} \quad , \qquad \alpha_{A2} \equiv \frac{n_{AIII}}{n_{AII} + n_{AIII}} \quad , \tag{II.33}$$

respectively. Noting that the total number density

$$n_{t} = n_{AI} + n_{AII} + n_{AIII} + n_{e} = \frac{p}{kT} \quad ,$$

one may write

$$n_{AI} = \frac{1 - \alpha_{A1}}{1 + \alpha_{A1} + \alpha_{A1}\alpha_{A2}} \frac{p}{kT} \quad ,$$

$$n_{AII} = \frac{\alpha_{A1} - \alpha_{A1}\alpha_{A2}}{1 + \alpha_{A1} + \alpha_{A1}\alpha_{A2}} \frac{p}{kT} \quad ,$$

$$n_{AIII} = \frac{\alpha_{A1}\alpha_{A2}}{1 + \alpha_{A1} + \alpha_{A1}\alpha_{A2}} \frac{p}{kT} \quad ,$$

and

$$n_e = n_{AII} + 2n_{AIII} = \frac{\alpha_{A1} + \alpha_{A1}\alpha_{A2}}{1 + \alpha_{A1} + \alpha_{A1}\alpha_{A2}} \frac{p}{kT}$$

The equations (II.28) and (II.29) then reduce to

$$\frac{\alpha_{A1}(1-\alpha_{A2})(\alpha_{A1} + \alpha_{A1}\alpha_{A2})}{(1-\alpha_{A1})(1+\alpha_{A1}+\alpha_{A1}\alpha_{A2})} = \frac{F_{AI}(p,T)}{p} \qquad \text{(II.34)}$$

and

$$\frac{\alpha_{A2}(\alpha_{A2} + \alpha_{A1}\alpha_{A2})}{(1-\alpha_{A1})(1+\alpha_{A1}+\alpha_{A1}\alpha_{A2})} = \frac{F_{AII}(p,T)}{p} \qquad \text{(II.35)}$$

respectively. The elimination of α_{A2} (or α_{A1}) from the above two equations leads to a cubic equation in α_{A1} (or α_{A2}), which is rather disagreeable to deal with. Instead one may proceed to solve for the α_A's by a successive approximation, i.e., in solving for α_{A1} one can assert $\alpha_{A2} = 0$ and $\chi^*_{i,z} \cong \chi_{i,z}$, lifting the pressure dependence of $F_{AI}(p,T)$. Similarly, α_{A2} can be found by asserting $\alpha_{A1} = 1$. Then $\alpha^{(o)}_{A2}$ and $\alpha^{(o)}_{A1}$ of the zeroth order approximation can be used to find, respectively, $\alpha^{(1)}_{A1}$ and $\alpha^{(1)}_{A2}$ of, say, the first order approximation, now taking $\chi^*_{i,z} = \chi_{i,z} - \Delta\chi_z$. And so forth. In fact, only one iteration of this sort is sufficient to give rise to the true α_A's within 0.1% (see Appendix A).

Alternatively one can introduce the notion of the electron pressure here and proceed to calculate α_A's for given p and T using the scheme of approximation described in

the next example. Under any circumstances, the iterative process is necessary, considering the fact that the lowering of the ionization potential depends on the α_A's. A fortunate break is the fast convergence of the successive approximation, as mentioned, which stems from the weak dependence of $F_{i,z}(p,T)$ on $\Delta\chi_z$.*

C) Ionization equilibrium in the binary mixture of monatomic gases

It is often convenient for spectroscopic studies to mix a small amount of the species of interest, perhaps a heavy element, in the bath of an inert gas. Imagine a case in which this heavy element, A, undergoes two stages of ionization while the inert gas, B, experiences only the first stage. Define the concentration of A in the gas by

$$C_A^\circ \equiv \frac{n_{AI} + n_{AII} + n_{AIII}}{n_t - n_e} = \frac{p_A^\circ}{p_A^\circ + p_B^\circ}, \qquad \text{(II.37)}$$

where p_A° and p_B° are the partial pressures of nuclei of the species A and B, respectively. The total number density is

---

* We should like to refer back to Section 2 of this chapter, where successive reflections were discussed and distinguished by an index n. In eq. (II.6) we defined the effective molecular weight σ. For a one-component gas σ_n/σ_{n-1} of eq. (II.20) can be expressed in the following fashion:

$$\frac{1}{\sigma_{n,0}} \equiv \frac{\sigma_0}{\sigma_n} = \frac{\sigma_{n-1}}{\sigma_n}\frac{\sigma_{n-2}}{\sigma_{n-1}} \cdots \frac{\sigma_0}{\sigma_1}$$
$$= 1 + \alpha_{A1} + \alpha_{A1}\alpha_{A2} \Big|_{n^{th}\,state} \qquad \text{(II.36)}$$

given by

$$n_t = n_{AI} + n_{AII} + n_{AIII} + n_{BI} + n_{BII} + n_e = \frac{p}{kT} .$$

Keeping the definition of the degrees of ionization shown earlier in mind, we may write down the electron pressure in the following manner:

$$p_e = n_e kT = \frac{c_A^\circ(\alpha_{A1} + \alpha_{A1}\alpha_{A2}) + (1 - c_A^\circ)\alpha_{B1}}{1 + c_A^\circ(\alpha_{A1} + \alpha_{A1}\alpha_{A2}) + (1 - c_A^\circ)\alpha_{B1}} \quad \text{(II.38)}$$

Then we obtain three simultaneous equations of ionization equilibrium:

$$\frac{\alpha_{A1}(1-\alpha_{A2})}{1-\alpha_{A1}} = \frac{F_{AI}(p,T)}{p_e} , \quad \text{(II.39)}$$

$$\frac{\alpha_{A2}}{1-\alpha_{A2}} = \frac{F_{AII}(p,T)}{p_e} , \quad \text{(II.40)}$$

and

$$\frac{\alpha_{B1}}{1-\alpha_{B1}} = \frac{F_{BI}(p,T)}{p_e} . \quad \text{(II.41)}$$

Note that the Debye radius of eq. (II.30) can be written as

$$\rho_D = \frac{kT}{2e\sqrt{2\pi(p_e + p_{AIII})}} , \quad \text{(II.42)}$$

where p_{AIII} stands for the partial pressure of the second ions of A. In iterating, one may start by guessing $p_e^{(o)}$ for

given p and T to solve i) the equation (II.49) for $\alpha_{A1}^{(o)}$ with an assertion that $\alpha_{A2} = 0$, ii) the equation (II.50) for $\alpha_{A2}^{(o)}$ with an assertion that $\alpha_{A1} = 1$, and iii) the equation (II.51) for α_{B1}. Then $p_e^{(1)}$ and $\Delta\chi_z^{(1)}$ can be estimated using $\alpha_{A1}^{(o)}$, $\alpha_{A2}^{(o)}$ and $\alpha_{B1}^{(o)}$, and used for the next iteration. This process continues until it is seen that $p_e^{(n-1)} = p_e^{(n)}$ within the acceptable accuracy, when the true values of $\alpha_{i,z}$ become available. Again the convergence of iteration is very rapid.*

D) Ionization equilibrium in the mixture of polyatomic and monatomic gases

Apart from the immediate interest in the molecular structure there often are cases where one has to introduce certain polyatomic gases into the bath of an inert gas. One typical situation is that certain metallic species of spectroscopic interest are difficult to obtain in the gaseous phase except via metallo-organic compounds which have high vapor pressures at room temperature. Another common case arises when one wishes to vary the shock strength over a wide range so that the luminosity level behind the primary shock

---

* It should be noted that for a two component mixture

$$\frac{1}{\sigma_{n,o}} = (1 - c_A^o)(1 + \alpha_{B1}) + c_A^o(1 + \alpha_{A1} + \alpha_{A1}\alpha_{A2}) . \qquad \text{(II.43)}$$

See eq.s. (II.20) and (II.36).

may become very low. The use of some polyatomic gas with a rich molecular spectrum as a low concentration additive helps one to see the details of the flow without seriously affecting the thermodynamics of the shocked medium. In the present experimental work the additive sometimes used was tetramethylsilane. Of course, the complete dissociation of the additive is highly desirable immediately behind the primary shock because, although the influence of the dissociated additive on the thermodynamic variables of the shocked medium is taken into account in any event, it nevertheless simplifies the theoretical computation to a great extent.*

Let us consider a mixture of two different monatomic gases, A and B, and a polyatomic gas, P. Denoting C_A^o, C_B^o, and C_P^o their respective concentrations, it is true that

$$C_A^o = 1 - C_B^o - C_P^o .$$

It is sufficient to consider the first ionization of each species only. Let ξ be the number of atoms in the polyatomic molecule. Then there are $(\xi + 2)$ simultaneous equations of the following type:

$$\frac{\alpha_{i1}}{1-\alpha_{i1}} = \frac{F_{ir}(T)}{p_e} , \quad i = 1, 2, \cdots \xi, A, B . \qquad (II.44)$$

---

* For the molecules having large dissociation potentials, one can write out the relations for the dissociation equilibrium from the equation (II.27) by defining the degrees of dissociation in the same manner as for the ionization. The relations thus obtained should be solved simultaneously with those of the ionization, e.g., equations of (II.44). For more detailed discussion, see references by Wilkerson and Brown.

It is also asserted that

$$F_{iI}(p\ T) = F_{iI}(T)$$

Note that

$$p_e = \sum_i \alpha_{iI}\, p_i^\circ = \sum_i \frac{p_i^\circ F_{iI}(T)}{p_e + F_{iI}(T)} \qquad \text{(II.45)}$$

where the pressure of the nuclei

$$p^\circ = \frac{p - p_e}{1 + \xi C_p^\circ} \qquad \text{(II.46)}$$

In order to find the various degrees of ionization, one proceeds to estimate p_e for a given p and T from (II.45) by trial and error. It is found helpful that usually $p_e \ll p$ under these conditions, thus allowing one to put $p - p_e \cong p$. p_e then furnishes α's through eq. (II.44).

4. Numerical Calculations on Shocked Mercury and Mercury-Neon Mixtures

The Rankine-Hugoniot relation (see eq. (II.16)) is evaluated for pure mercury and mercury-neon mixtures by assigning the primary shock parameter, r_o, as defined by (II.19).*

---

* The shock parameter r_o is related to the shock Mach number M_s by

$$r_o \equiv \frac{\sigma_o U_1^2}{RT_o} = \gamma_o M_s^2$$

where γ_o is the specific heat ratio of the gas ahead of the n = 1st shock front. At $T_o = 200^\circ C$ $r_o = 100$ corresponds to $U_1 = 1.381$ mm/μsec or $M_s = 7.51$.

The pressure ratio, p_1/p_o, is first calculated and then the density ratio, ρ_1/ρ_o, using equations (II.18) and (II.16), respectively. Quantities such as Z_{HgI}, Z_{HgII}, Z_{HgIII}, f_{EHgI}, f_{EHgII}, and f_{EHgIII} (see eq. (II.9)) needed in the course of shock calculation are evaluated using spectroscopic data on mercury tabulated by Charlotte Moore.[50]

Fig. 2 shows the Rankine-Hugoniot relation in pure mercury for p_o = 0.5, 1, and 5 cm Hg and T_o = 473.2° and 673.2 °K. Only two stages of ionization are considered in the entire calculation. Each stage of ionization is clearly recognized in each curve through its characteristic peak, which, in fact, corresponds to the nearly complete ionization in a respective stage. If there were no higher stages of ionization than the second, all curves would fall into the dotted line (-------) after the completion of both ionizations. Notice that the increase in p_o tends to make the curves smoother, i.e. the peaks in the curve tend to merge as the pressure behind the shock increases. This is so because the greater the pressure of the shocked gas for a given temperature, the more the degrees of ionization overlap (see Fig. 7).

In Fig. 3 the Rankine-Hugoniot relation in mercury-neon mixtures is plotted for fixed p_o and T_o, but with different mercury concentrations C^o of 0.01, 0.10, 0.50, and 1. In the calculation, two stages of ionization of mercury are considered and only one stage of neon. The curve corresponding to C^o = 0.5 reveals rather clearly the role of the first and

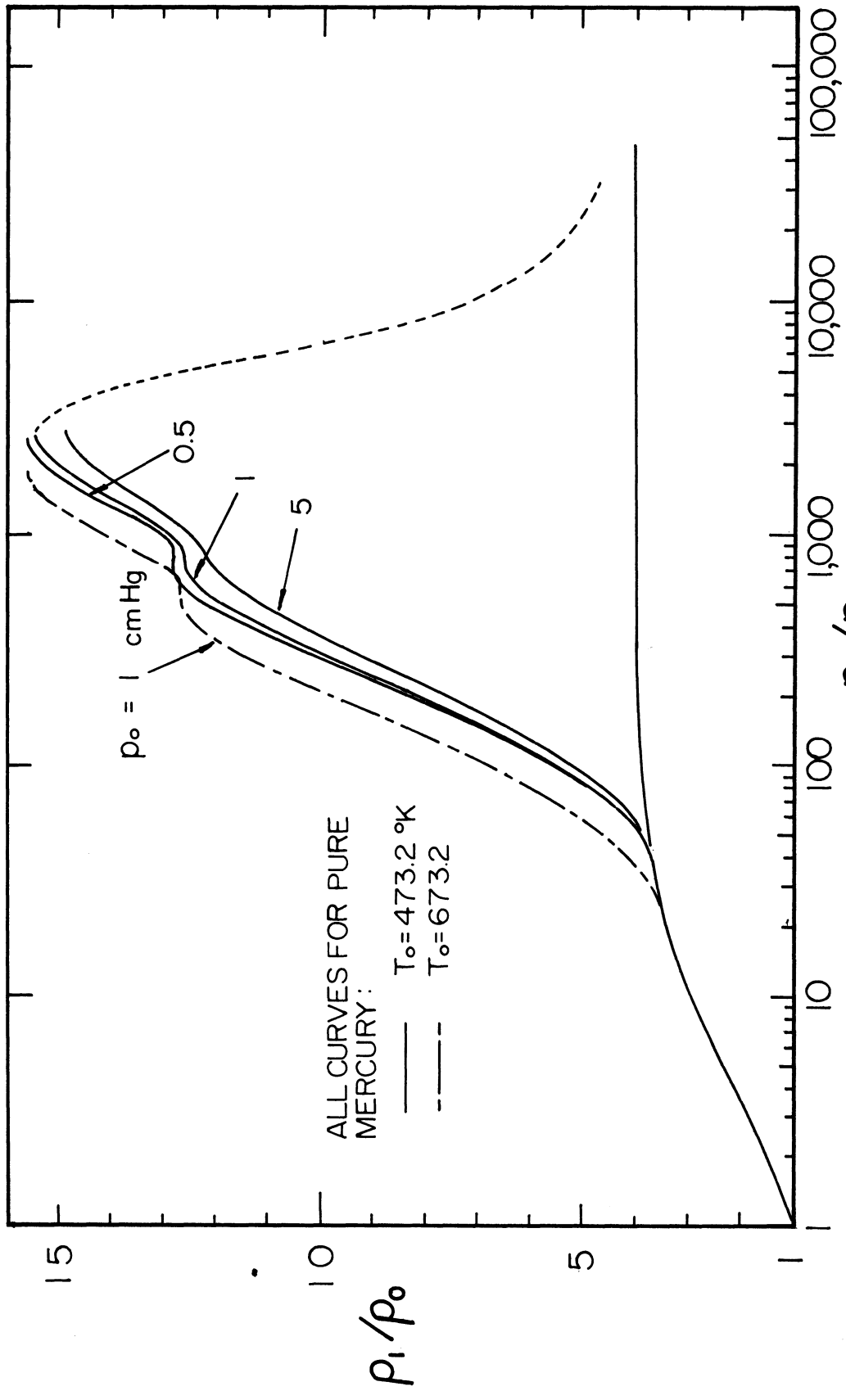

Figure 2. Rankine-Hugoniot relation for pure mercury

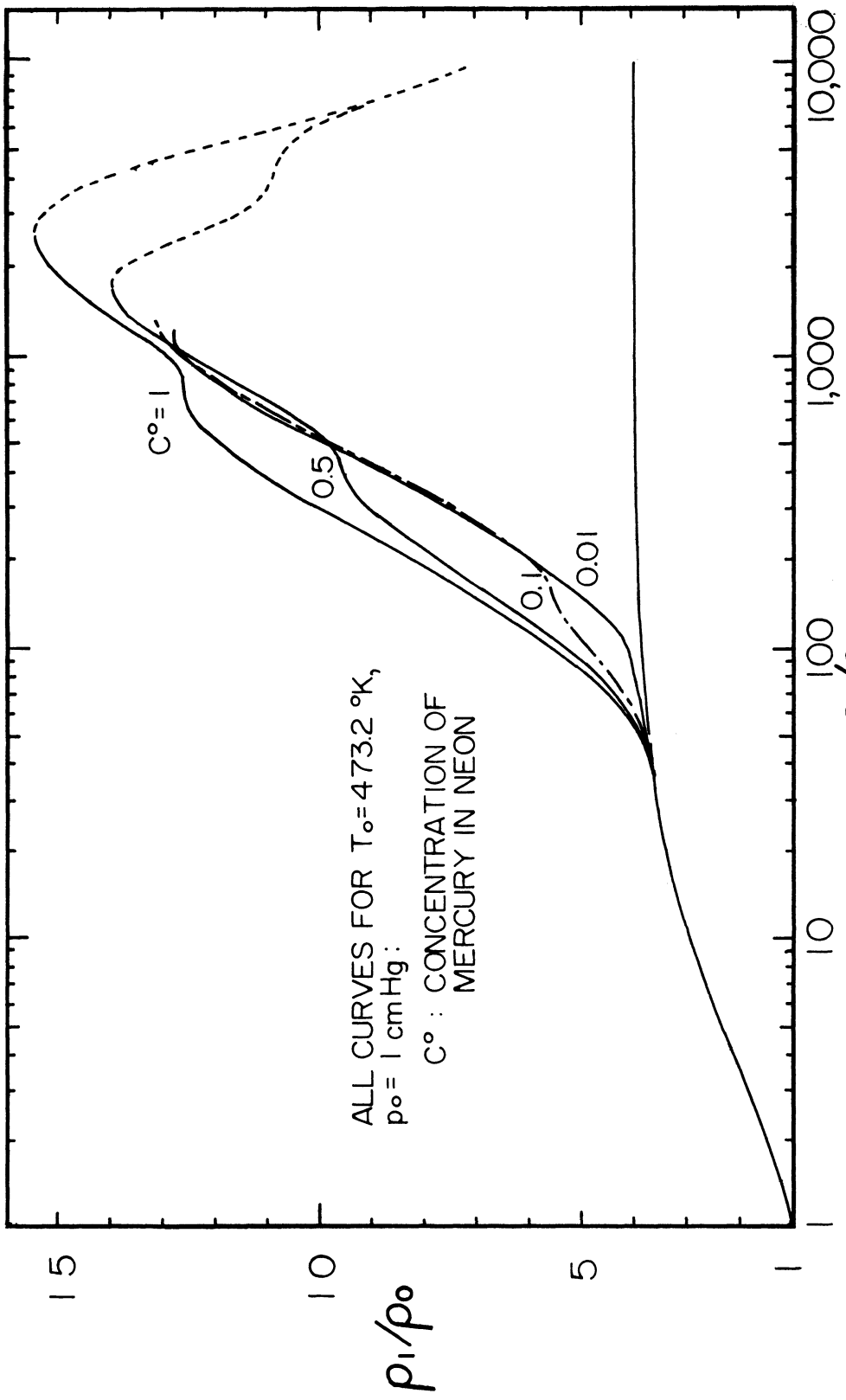

Figure 3. Rankine-Hugoniot relation for mercury-neon mixtures

second ionizations of mercury and finally also of the first ionization of neon. Again if there were no further stage of ionization than these, the curve of $C^o = 0.5$ would fall into the dotted line (-------) as the gas becomes a mixture of second ions of mercury, first ions of neon and electrons only. The curve of pure mercury ($C^o = 1$) approaching the limit of the same dotted line as for $C^o = 0.5$ is a mere coincidence stemming from the fact that the ionization potentials of neutral neon and singly ionized mercury happen to be nearly the same. However, it is of course true that any Rankine-Hugoniot curve will ultimately approach the ideal gas limit as $p_1/p_o \rightarrow \infty$.

Other quantities arising from the shock calculation for pure mercury (see Section 3B) are shown in Fig. 4. Plotted are the electron density, n_{el}, and the temperature, T_1, both behind the primary shock (n = 1) as functions of r_o for p_o = 0.5, 1, and 5 cm Hg and T_o = 473.2 °K and 673.2 °K. r_o = 500, for example, corresponds to shock speed of U_1 = 3.131 mm/μsec or M_s = 16.67 at an ambient temperature T_o = 473.2 °K; this is in the region of very strong shocks in pressure-driven shock tube practice. It is very interesting to see that for large r_o an effective way of raising the electron density is to increase not T_o but p_o, while for small r_o, T_o plays a role equal to that of p_o in controlling n_{el}. This can be explained in the following manner: for small r_o, i.e. for low T_1, the degree of ionization is small but very sensitive to a variation in T_1, resulting in the strong dependence of n_{el} on T_1 and, in

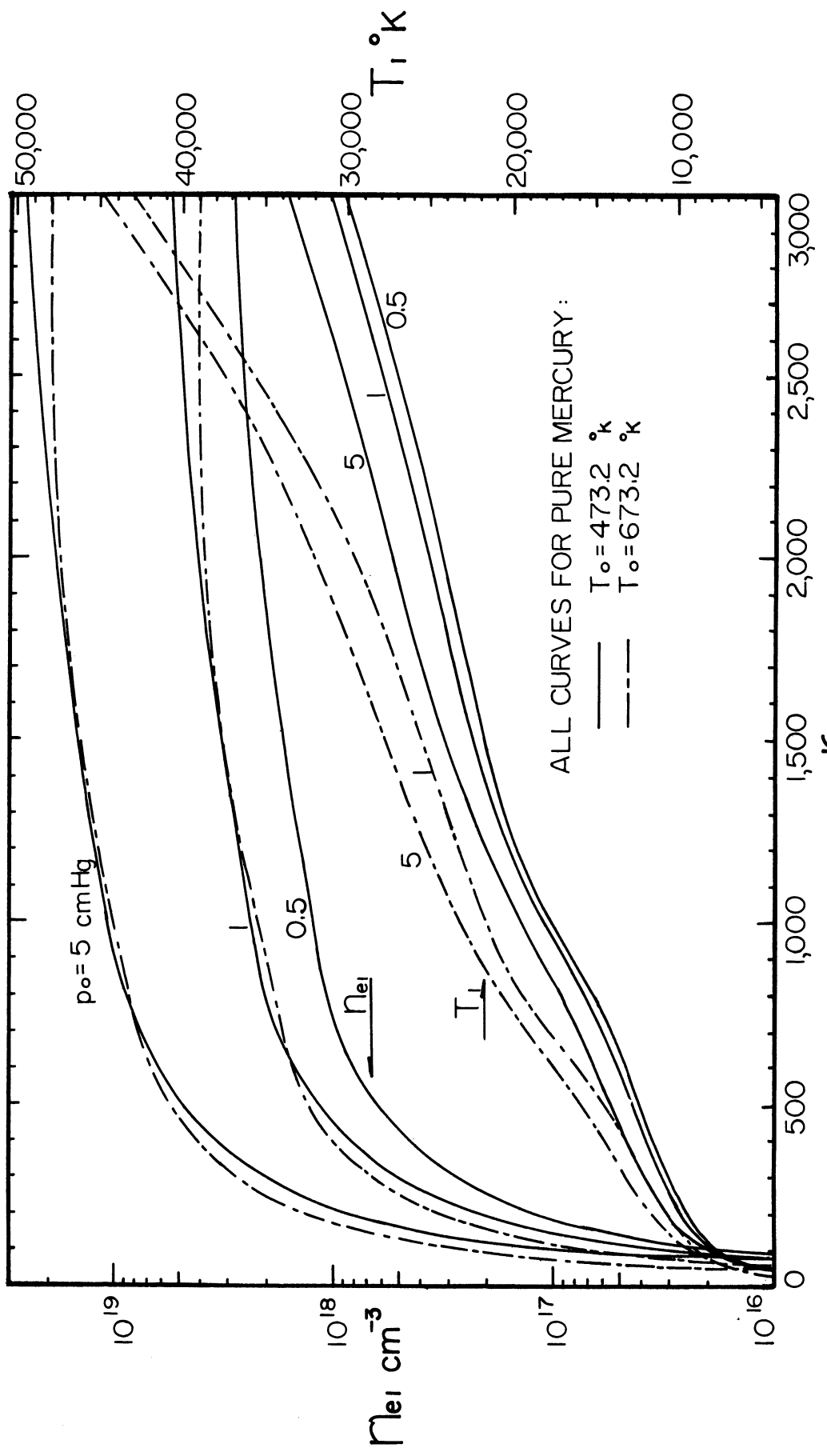

Figure 4. Electron densities and temperatures behind the n = 1st shock

turn, on T_o as well as on p_o. For large r_o, i.e. for high T_1, the degrees of ionization are large but do not undergo any drastic change because of the upper bound of the α's, thus allowing p_1 to emerge as the only alternative left in changing n_{el} by contributing to n_{t1}. p_1 or p_o for that matter is so effective in spite of the fact that for a given temperature the degrees of ionization decrease when the pressure increases, as seen in Fig. 7. Fig. 4 shows that the temperature, T_1, on the other hand, depends strongly on T_o for an entire range of r_o. It is of great significance that the pressure driven shock tube can produce thermal plasmas with electron densities rising as high as 10^{19} cm^{-3}.

In order to see the thermal behavior of mercury plasma irrespective of any specific shock, quantities such as the partition functions Z_{HgI}, Z_{HgII}, Z_{HgIII}, and the effective degrees of freedom f_{EHgI}, f_{EHgII}, f_{EHgIII} are calculated as functions of T for a given set of pressures and plotted in Figs. 5 and 6. As discussed in section 3 of this chapter, these quantities for an atom and its ionic derivatives are dependent on p via the cut-off of discrete energy levels due to interactions with neighboring particles. As the pressure increases, the electronic partition function generally decreases, as shown in Fig. 5, due to the fact that the number of physically possible ways of distributing the atoms over the electronic states decreases because the available discrete levels are reduced by the increasing number of

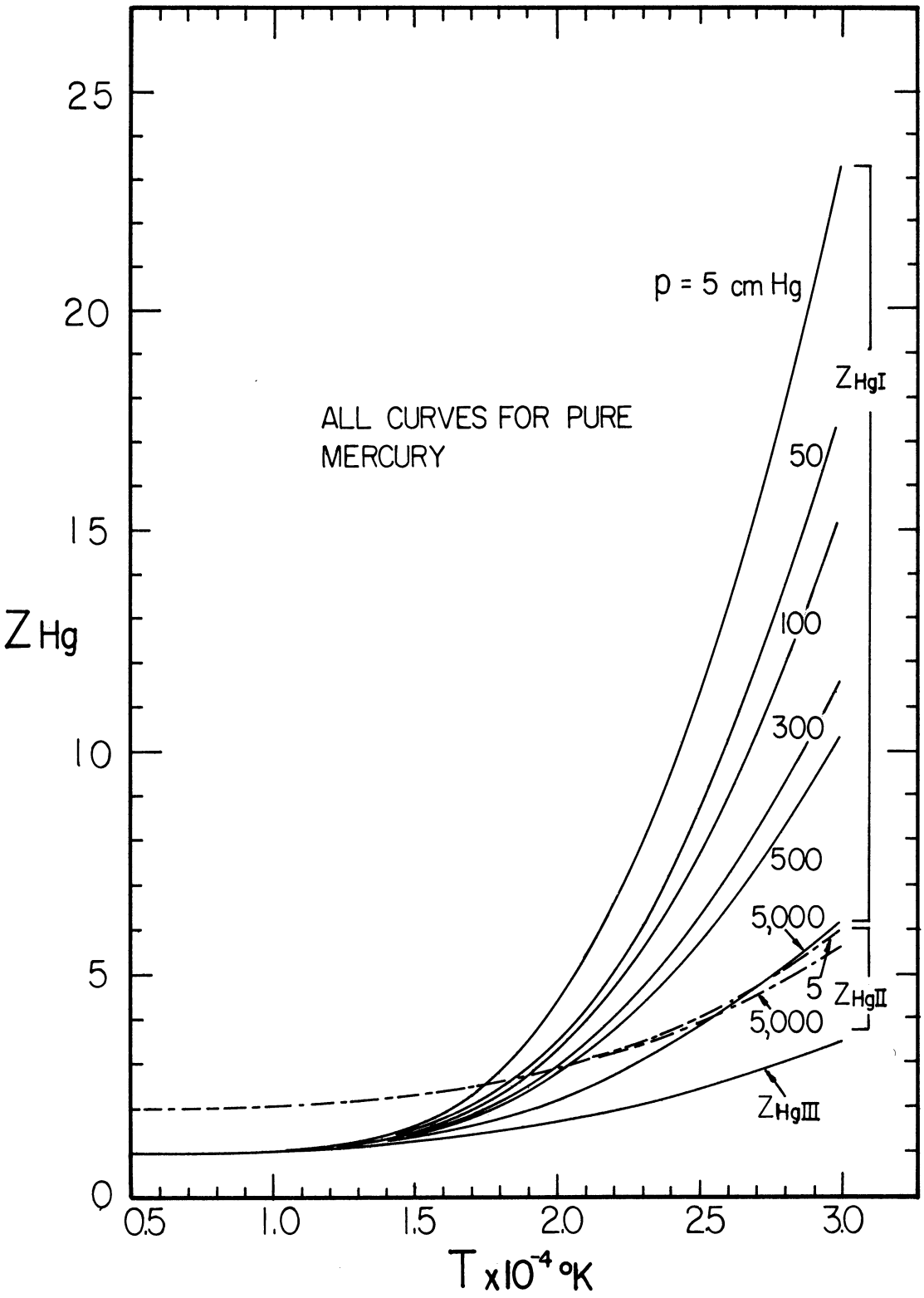

Figure 5. Electronic partition functions of neutral and ionized mercury

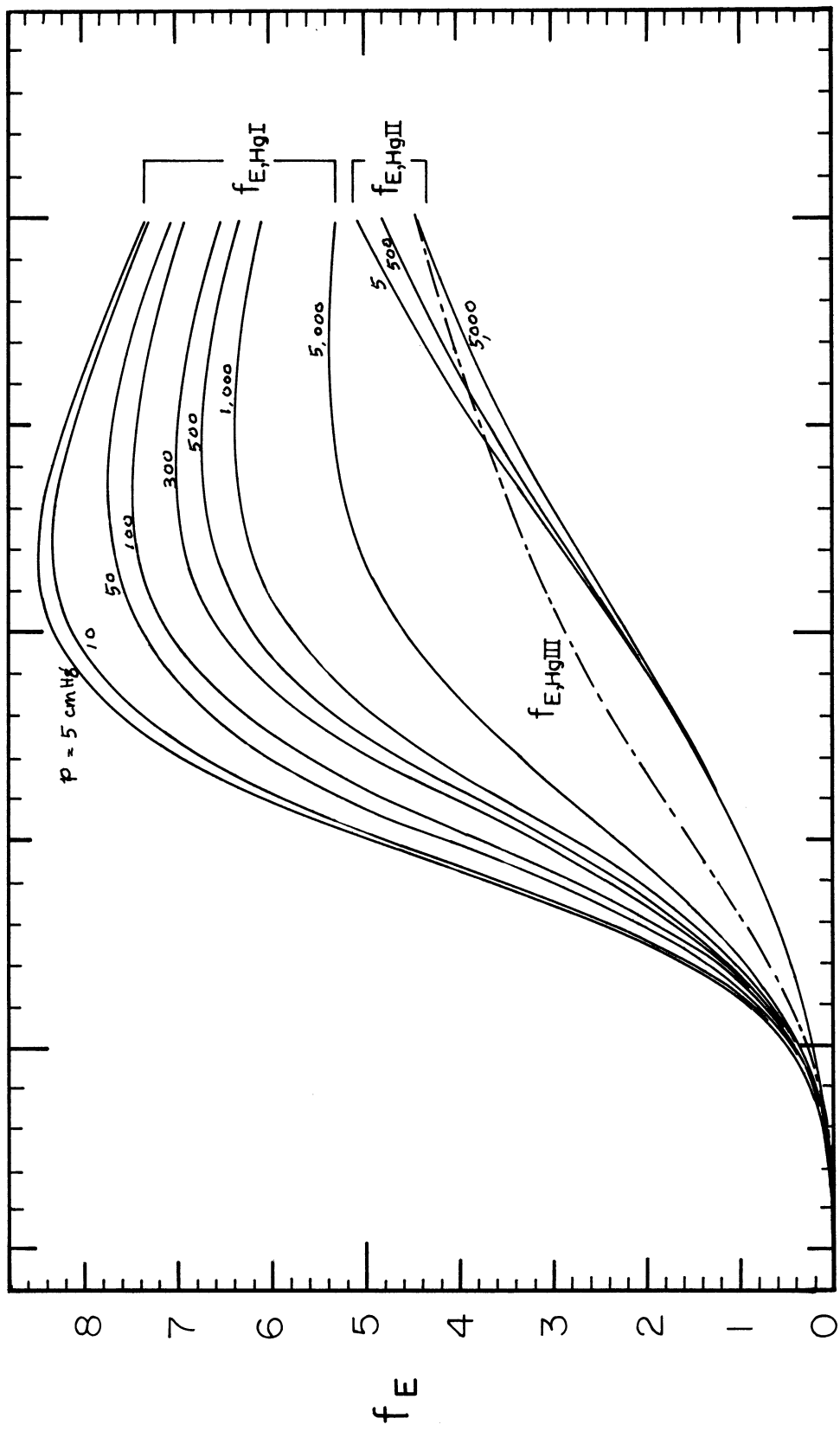

Figure 6. Electronic degrees of freedom of neutral and ionized mercury

perturbing particles (charged or not charged) in the neighborhood of the atom or ion in question. Similarly do the electronic degrees of freedom (f_{EHgI}, f_{EHgII}, and f_{EHgIII}) decrease as shown numerically for neutral and ionized mercury in Fig. 6. For $f_E = 3$ one can say that the electronic and translational modes are being excited at the same rate (recall the definition of f_E in (II.9)). The fact that $f_{Ei,z}$ becomes very large at high temperatures is actually immaterial because by then most of the species iz will have been ionized.

Plotted in Fig. 7 are the degrees of first and second ionizations of mercury. The pressure dependence of the α's comes i) from the pressure explicitly appearing in the right hand sides of equations (II.34) and (II.35), and ii) from the lowering of ionization potential which in turn depends implicitly upon the pressure. It is worthwhile to notice that for low pressure the curves of first and second ionizations are well separated, but for high pressure they overlap each other. Though dealt with separately, quantities plotted in Figs. 5, 6, and 7 are strongly interdependent and no single one of them can be evaluated independently. The whole process of iterative method described in section 3 of this chapter has been employed in the calculation.

Lastly the equation of state for high temperature mercury gas

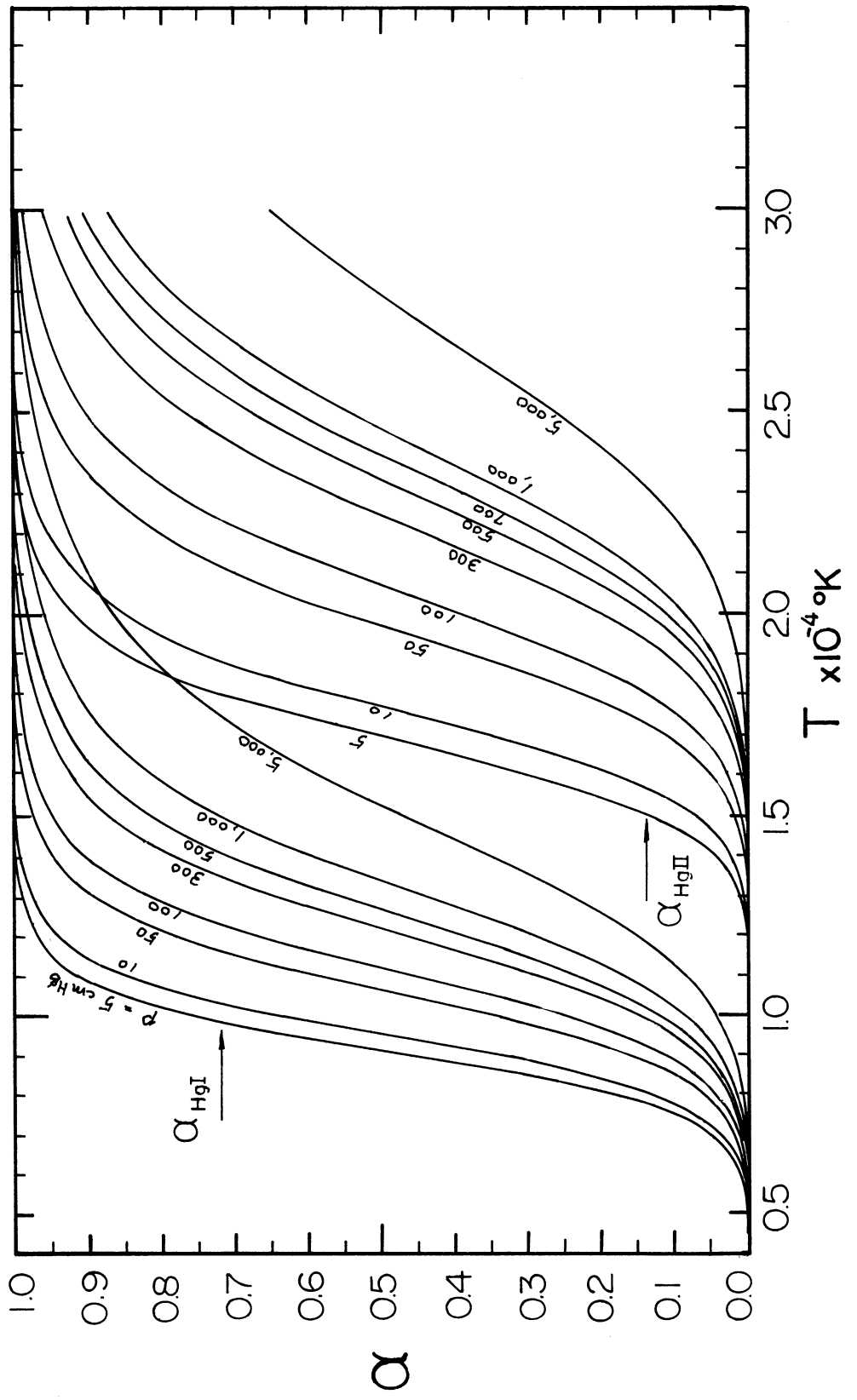

Figure 7. Degrees of ionization of mercury

$$\frac{p}{\rho} = \left(1 + \alpha_{Hg1} + \alpha_{Hg1}\alpha_{Hg2}\right)\frac{kT}{m_{Hg}} \qquad \text{(II.47)}^{*}$$

is plotted in Fig. 8. Again the pressure dependence is present through α's. Furthermore, the linearity between p/ρ and T drifts from the ideal gas limit to the first ionization limit and then to the second ionization limit as the temperature increases. This is to say that the fraction of energy stored in the translational mode increases drastically as the ionization becomes active because the free electron thus released add substantially to total particle number density (n_t), resulting in a sharp rise of the pressure.

---

* It should be observed thatthis equation of state is equivalent to eq. (II.5).

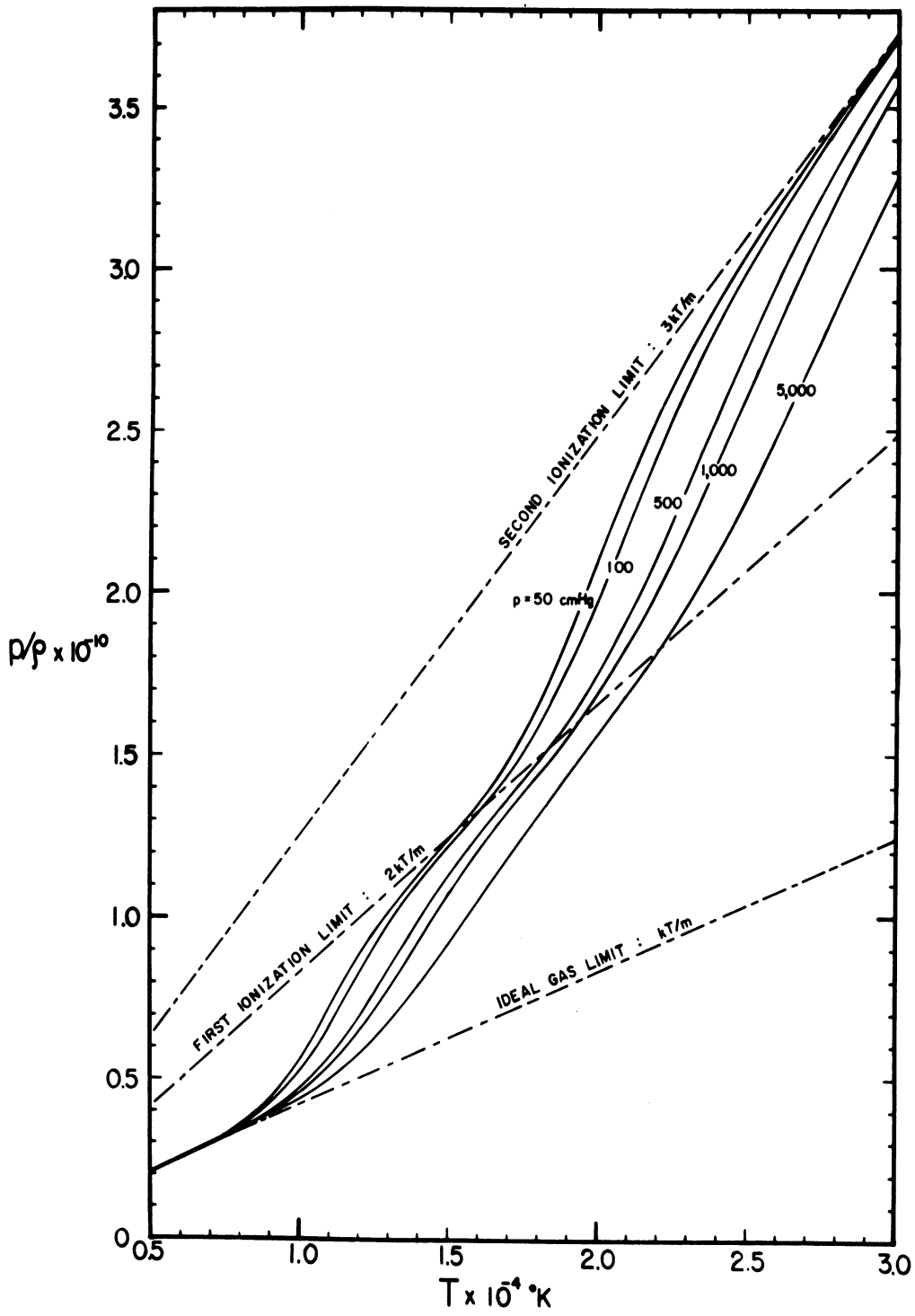

Figure 8. Equation of state in mercury gas

CHAPTER III

FLUID-DYNAMICAL EXPERIMENTS

1. Introduction

The objective of this chapter is to study the overall performance of the heated shock tube as a new fluid-dynamical device, and to examine the detail of shock-induced high temperature flow in the hope of evaluating its usefulness as a spectroscopic source and pinpointing its drawbacks, if any, together with remedies.

The heated shock tube and accessory equipment are briefly described in Section 2, followed by a broad sketch of shock tube flows in Section 3. Also reported is a novel observation of the reflected shock bifurcation in the monatomic gas of mercury. In Section 4 detailed quantitative analyses of the boundary layers in the flows ($n = 2$) are presented and empirical relations descriptive of respective flows are obtained. A theoretical model of the bifurcation is formulated and applied to other monatomic gases via numerical calculations in Section 5.

The entire analysis depends heavily on measured shock speeds and thermodynamic variables calculated from them via the shock theory discussed extensively in Chapter II. Most of the quoted data and discussion refer to pure mercury gas. Cases of neon-mercury mixtures are mentioned accordingly. For the constructional detail of the heated shock tube, the reader is referred to the reports by Kim and Laporte[31] and

by Kim[30].

2. Description of Equipment

Fig. 9 shows schematically a sideview of the entire heated shock tube. It consists of three major parts: the main shock tube, the cylindrical furnace surrounding it, and the large outer tube within which they both are contained.

The main shock tube is constructed entirely of stainless steel, type 304. The expansion tube consists of five sections and two interchangeable test sections that are made of seamless rectangular tubing with inner dimensions 1.510" x 2.560", wall thickness 0.375", and inner corner radius 0.300". The total length of the expansion tube is 144.75". The inner surface of the entire expansion tube is highly polished with a specially designed tool. The interior of the test section is treated with molten sodium dichromate to reduce the surface reflectance. The sections are assembled so as to be vacuum and high pressure tight by squeezing nickel-plated copper gaskets between each pair of matching flanges. The quartz windows are sealed onto the test sections using O-rings of stainless steel and monel. Direct contact between optical quartz and metal O-rings is avoided by inserting a thin

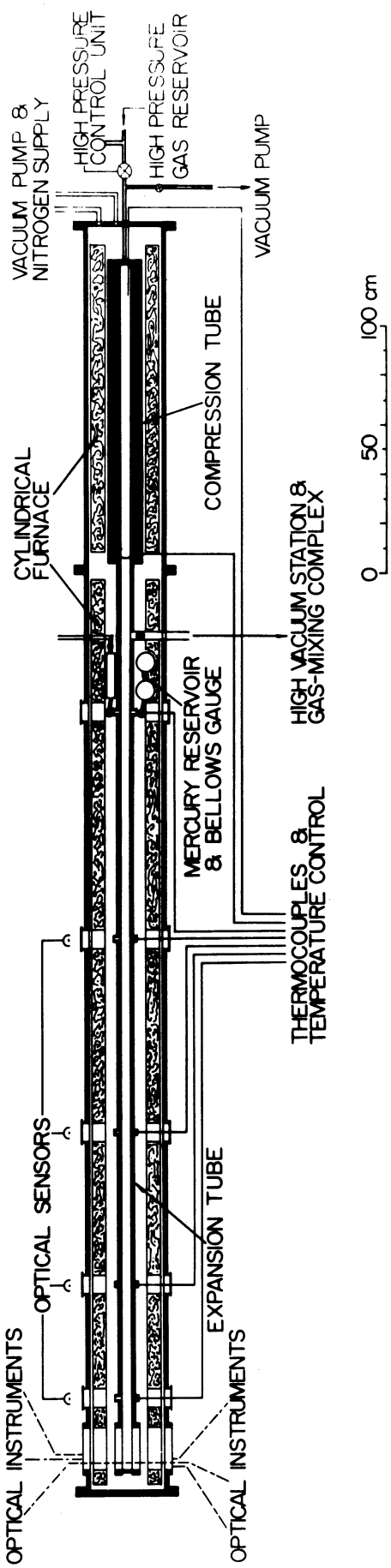

Figure 9. Schematic drawing of the heated shock tube

The compression tube is made of 48" long tubing of the same kind as the expansion tube, enclosed within another cylindrical steel tubing of 6" diameter. The space between the two tubings is filled up with refractory cement. Copper or aluminum sheets, 0.050" to 0.080" thick, are used as diaphragm material. Due to the fact that the diaphragms are held within a pair of matching circular grooves cut in the flanges, no additional gaskets are needed. The diaphragms are scored diagonally in the usual way. The entire tube proved to be well sealed from the vacuum of 5×10^{-5} torr to the high pressure of 1000 psi. The compression tube can be filled with H_2, He, or N_2 to 2,500 psi (170 atm) by means of a remote-controlled high pressure system.

The cylindrical furnace of 8" inner diameter is divided into six indicidually controlled electrical heating units, each with Chromel "C" #16 wire windings. The maximum total power is rated at 20 KW, making it possible to raise the shock tube temperature from room temperature to 400 ^{o}C in five hours. The furnace is wrapped with fiberglass insulation and placed within an outer tube of 14" inner diameter. The outer tube likewise consists of sections and is wrapped again with fiberglass and asbestos insulation to an outer diameter of 18". For safety reasons the pressure in the outer tube may be kept at a subatmospheric level.

Fig. 10 shows the completed shock tube in operation. Shown in Fig. 11 are the vacuum system connected ultimately

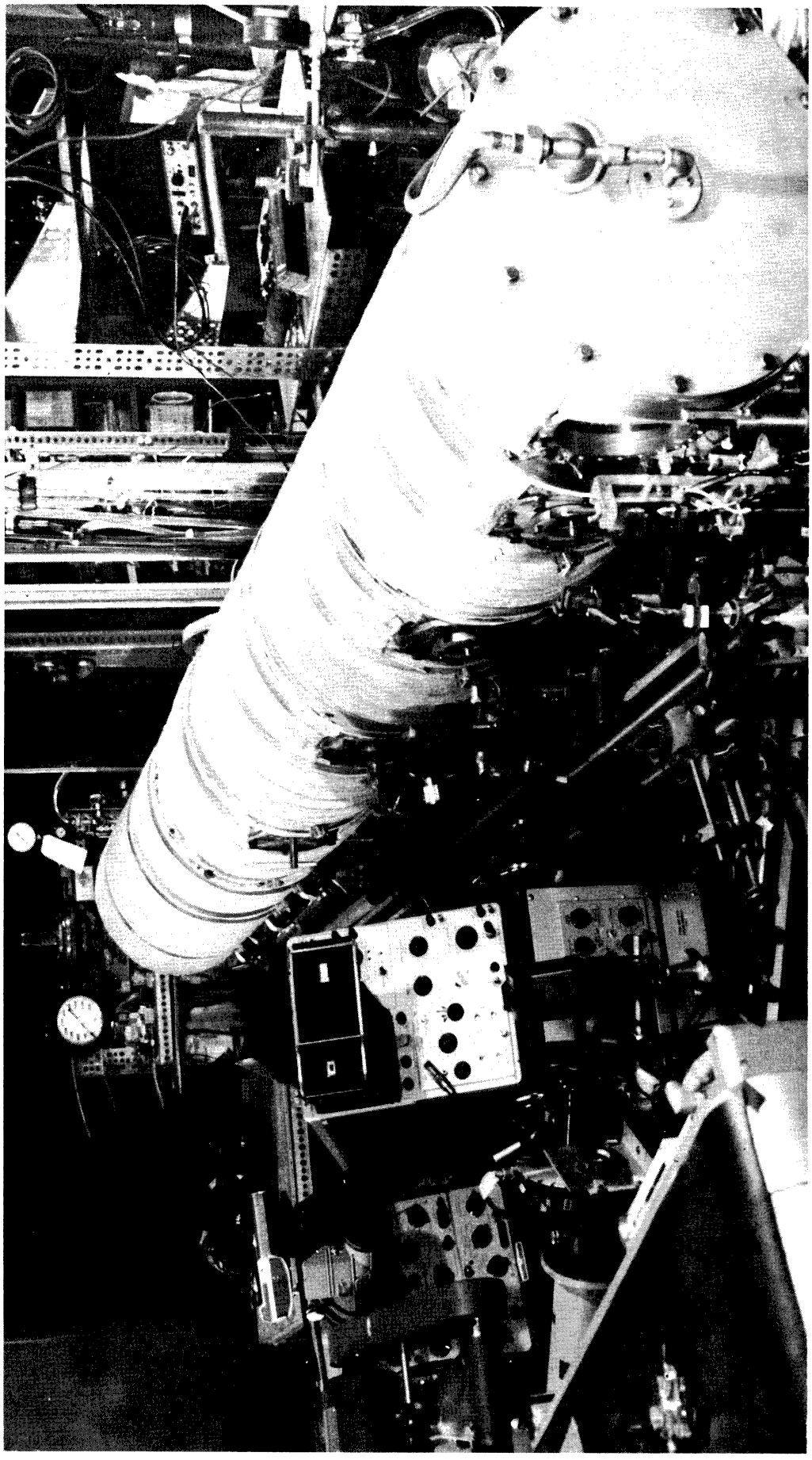

Figure 10. Completed heated shock tube in operation

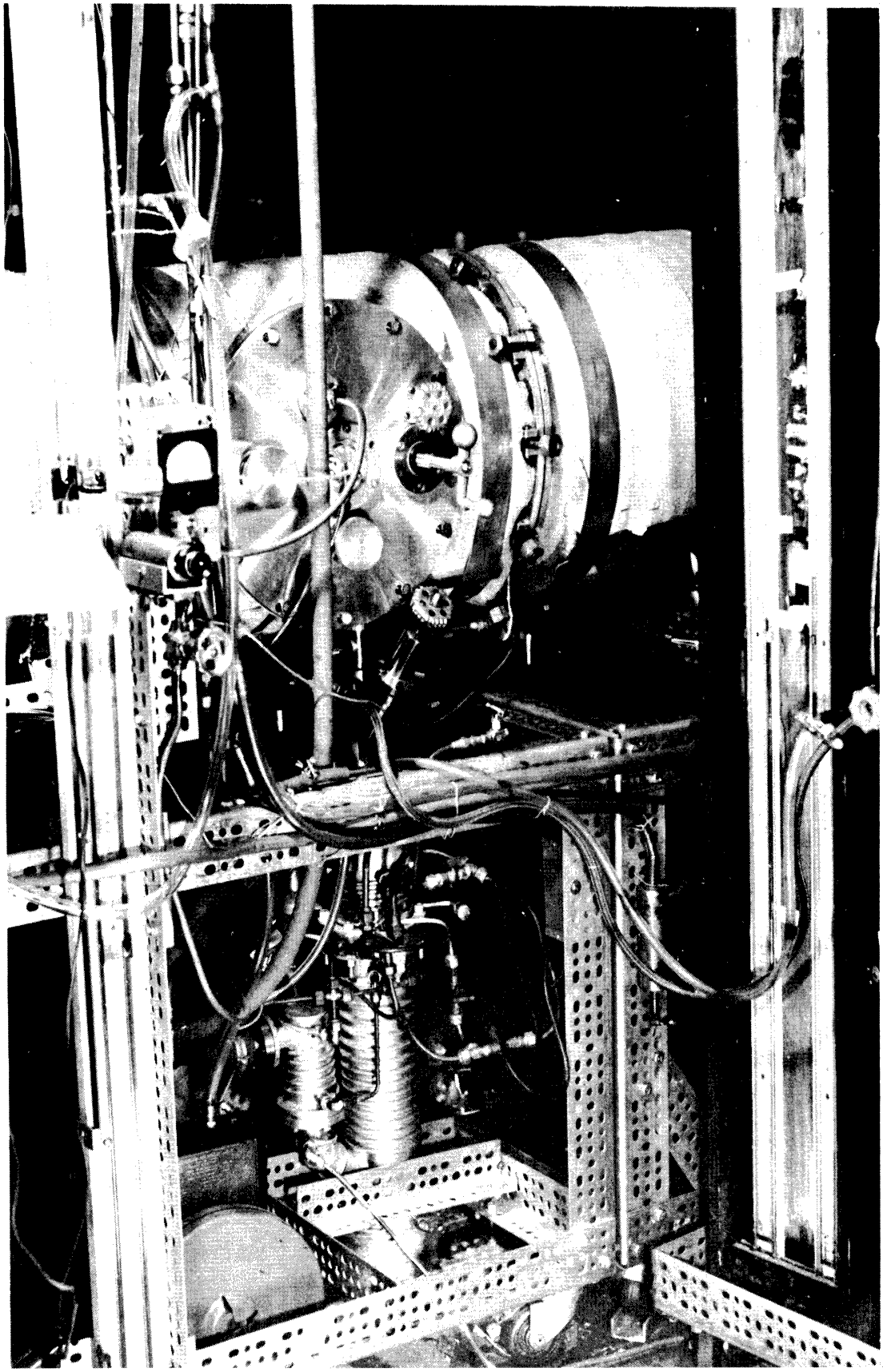

Figure 11. Vacuum system and gas-mixing complex

to the main shock tube and the gas mixing complex for the handling of all non-mercuric gases.

The mercury reservoir is installed within the furnace and connected to the expansion tube via a set of all-metal valves. The pressure of mercury gas in the expansion tube is measured for each shot with a stainless steel sylphon bellows gauge which is also installed within the furnace. This gauge is designed on the following principle: the space within the bellows is exposed only to the mercury gas present in the expansion tube, resulting in the expansion of the bellows along its axis. This can be counteracted by the build-up of air within another vacuum-tight chamber which houses the bellows. The change in the pressure of air needed to bring the bellows back to the initial position when no mercury was present is a measure of the mercury gas pressure. It is independent of the temperature gradient in the air as long as the air pressure is kept high.

In locating the initial position of the bellows, an insulated electrical feedthrough mounted on the outer chamber is put to make a gentle contact with the top of the bellows when both sides of the bellows are pumped to vacuum. A very weak current is allowed to flow through the contact. The pressure outside the bellows is then raised slowly until the current drops to, for instance, one half of the initial current when the electrical contact was firm. This pressure reading obtained constitutes the zero point in pressure measurements that follow.

When mixing mercury and other gases, another small metal container is employed to temporarily keep pre-mixed non-mercuric gases (prepared outside) at an appropriate pressure. After the mercury gas has filled the tube, the mixture in the container is released into the tube and the final total pressure is measured with the bellows gauge. The concentration of each component is thus accurately determined.

Diagnostic equipment consists of two rotating drum cameras, three grating spectrographs, one prism spectrograph, photomultipliers, and various chronograph counters. One rotating drum camera is used for the wave speed picture and aims normally at a long, narrow slit, either horizontal or vertical, mounted on the test window. An additional optical arrangement is made in such a manner that an oblique view of the shock is recorded in the same rotating drum camera as that which takes the normal wave speed pictures (see Fig. 13). Shock speeds are measured from wave speed pictures and checked often with photomultiplier measurements. The maximum error in a measured shock speed is 2%, owing to the inaccuracies in drum speed measurement (1/4%) and in reducing necessary parameters from the wave speed pictures. Spectrographs render possible the recording of spectral lines ranging from 2400 $\overset{\circ}{A}$ to 8000 $\overset{\circ}{A}$, all time-resolved to the order of a microsecond, either photographically or photoelectrically.

3. General Observations

Many shocks in mercury gas have been generated and observed, their shock Mach numbers ranging from 4 to 16 and the initial temperature varying from 200° to 320 °C. When the pressure ratio p_1/p_o across the primary (n = 1) shock front is related to the initial pressure ratio, p_c/p_o, before firing, one obtains the plot of Fig. 12 for two different driver gases—namely, hydrogen and helium. Also plotted and compared in the figure are the theoretically predicted relations. The familiar disagreement between theoretical and experimental values is attributed to the fact that the opening of the diaphragm is not abrupt enough to establish a well-defined pressure discontinuity and the shock attenuates while moving downstream indirectly due to boundary layer growth. This latter fact is confirmed here by using two different lengths of the expansion tube as shown in the figure.

Figure 13a shows typical wave speed pictures (normal view) of the primary and reflected shocks in pure mercury gas, where measured initial conditions together with calculated variables pertaining to Fig. 13a are as listed in Table III.

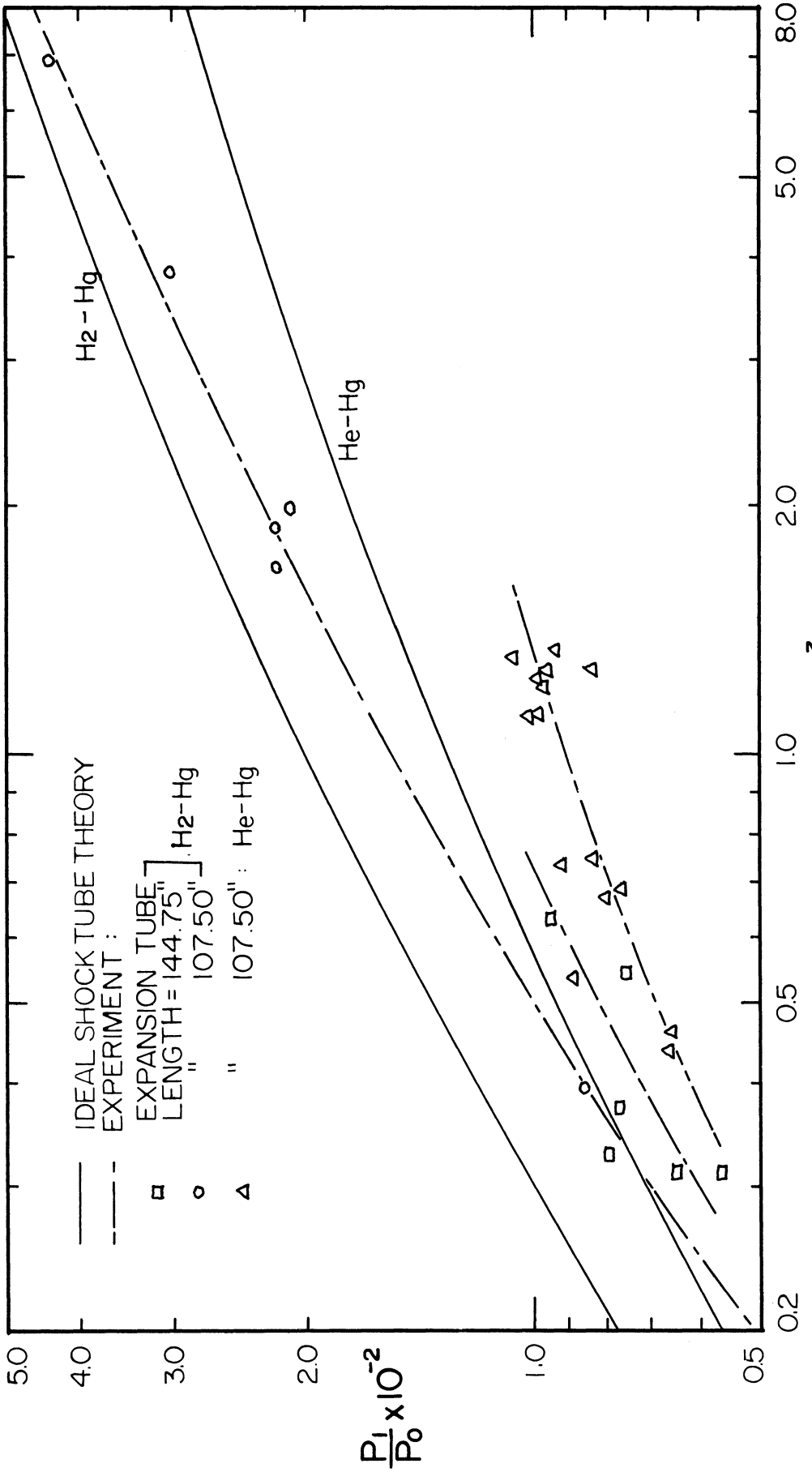

Figure 12. Shock strengths as a function of initial pressure ratio

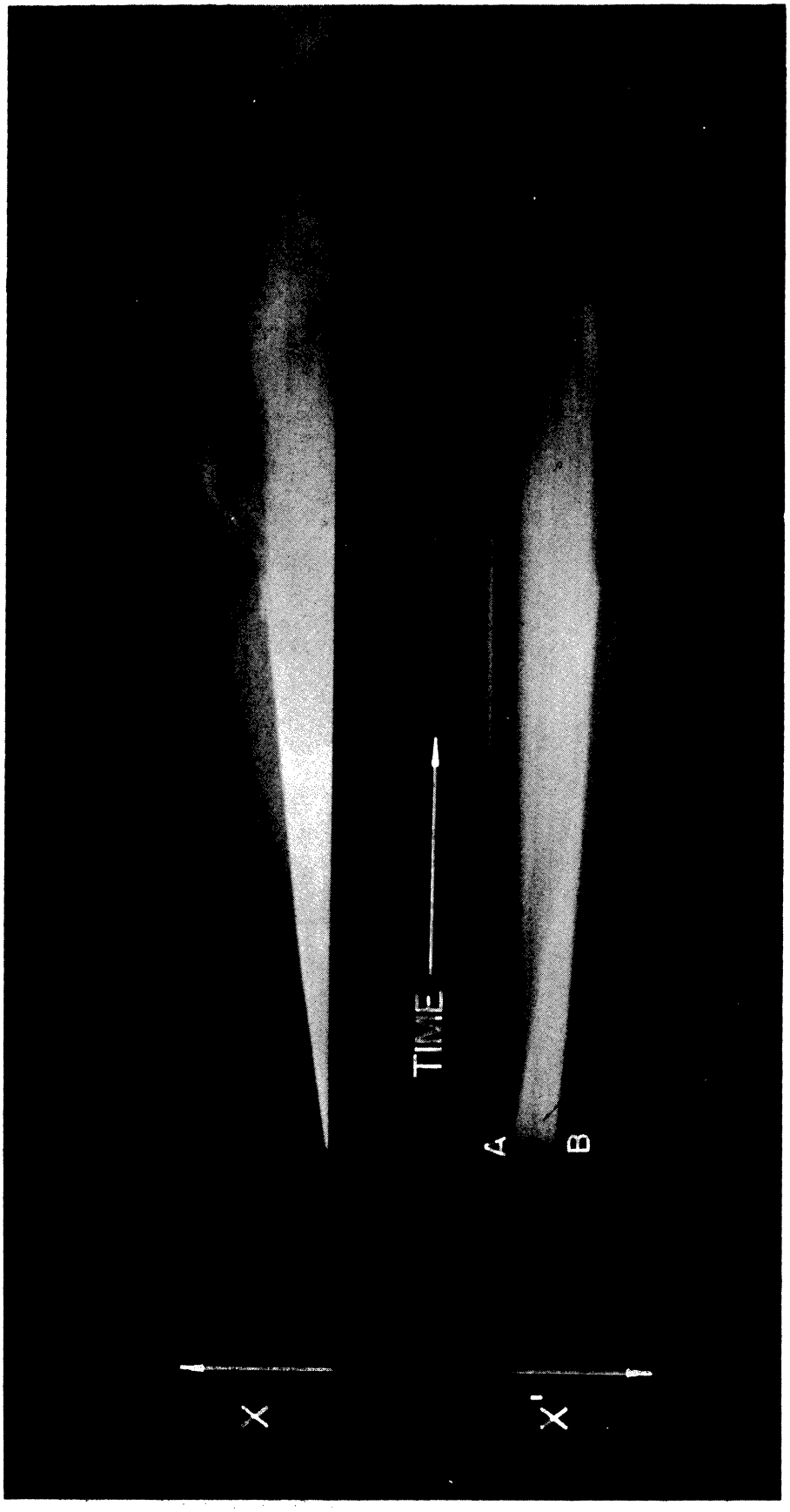

Figure 13. Wave speed pictures
a) Normal view and b) Oblique view

Table III.

Shock Variables Pertaining to Wave Speed Pictures of Fig. 13a (MHgVIII-11)

$T_o = 502.9\ ^oK$	$T_1 = 8{,}098\ ^oK$	$T_2 = 10{,}195\ ^oK$
$p_o = 1.953$ cmHg	$p_1 = 162.1$ cmHg	$p_2 = 790.5$ cmHg
$U_1 = 1.457$ mm/μs	$n_{e,1} = 6.62 \times 10^{16}\ cm^{-3}$	$n_{e,2} = 8.71 \times 10^{17}\ cm^{-3}$
$U_2 = 0.225$ mm/μs[a]	$u_1 = 1.161$ mm/μs[b]	$u_2 = 0.174$ mm/μs[c]

It will be noticed that the point on the endwall where the primary shock terminates and the point where the strong luminosity due to the first reflected shock (n = 2) begins do not coincide. However, when an additive such as tetramethylsilane ($Si(CH_3)_4$) is used (less than 0.06%), the wave speed picture shows the sharp luminosity at the position of the primary shock front.* In Fig. 13a, since no tetramethylsilane was used and since the tube was baked

a. Measured at the instant of reflection at the endwall.

b. $u_1 = U_1(1 - \rho_o/\rho_1)$

c. $$u_2 = \frac{u_1 - U_2(\rho_2/\rho_1 - 1)}{\rho_2/\rho_1}$$

* The sharp luminous line in the usual luminous shock tube was found to be mainly due to the transient molecular spectrum of C_2 coming from hydrocarbon additives (and wall impurities).[12,15]

extensively, no luminous line is seen. A generally bright region follows the shock front some time later, and the delay is considered to be the ionizational relaxation[12] of the shocked mercury gas. The relaxation time in shocked mercury gas has been measured for a variety of shock strengths, and the data will be analyzed in Chapter IV.

A close examination of Fig. 13a seems to show two reflected shocks, which we should like to explain as a bifurcation effect[35] (see Fig. 16, which however will be discussed in more detail later). Fig. 13b (space direction reversed!) is a wave speed picture taken not at right angles to the flow, but at an angle of 15^{o} from the normal. In Fig. 13a the spreading legs of the bifurcated shock on the side wall can be seen as apparently two reflected shocks, while in Fig. 13b the diminishing size of the main or normal reflected shock shows up clearly as a diminishing bright triangle. This shock disappears completely even before the encounter with the interface. This explanation is consistent with the fact that many mercury lines are strongly reversed in this region, indicating that the forked portion of the reflected shock has a more complicated structure than the simple discontinuity and the region behind the bifurcated shock is possibly even turbulent. Furthermore, it implies that the flow behind the primary shock has a growing boundary layer—growing much faster than expected in the monatomic gas. This in turn agrees well with the observation that, in the time trace of the spectral intensity in the strong

primary shock region, the intensity plateau reached after the relaxation period is maintained briefly and then deteriorates rapidly.

Many different tests have been made in order to pinpoint the possible cause of bifurcation. It was learned that the length of the expansion tube plays no significant role and neither do the initial pressures. The roughness of the inner surface of the test section and the geometry of the test window mounting seem to be somewhat responsible, but only to a limited extent. However, it has been seen possible to remove the bifurcation by either going for the weaker shocks in pure mercury gas or diluting the mercury gas with an inert gas such as neon. What it amounts to here is that the bifurcation in the monatomic gas of mercury, which is novel in itself, is dependent indirectly on the equilibrium temperature of the flow behind the primary shock, mainly through the ionization of the shocked gas. More about this point will be in Section 5.

For $M_s > 6.5$, the reflected shock speed, U_2, never exceeded 20% of the primary shock speed, U_1, owing to the strong ionization in this region and the energy loss to the endwall as expected. The empirical fact that for a given ratio, p_c/p_o, a longer reflected region is attained the greater the pressure, p_o, is not realized in the case of mercury because in most cases the significant range of the reflected shock is limited by the bifurcation independently of p_o, rather than by the interface. And for

the same reason no distinctive re-reflected shock (n = 3) at the interface is observed in the instances of strongly bifurcated shocks.

4. Quantitative Analysis of Shock Bifurcation

The analysis in this section centers around the previously mentioned shock bifurcation. As shown in Fig. 13b, the plane portion of the reflected shock diminishes when the shock moves away from the endwall, and one can in fact establish the size of the plane portion and relate it to a specific location via both Figs. 13a and b.

In concluding that the first reflected shock was bifurcated, a z-t diagram of the reflected shock proved to be useful, as shown in Fig. 14a. z is the vertical axis of the shock tube configuration. Fig. 14a was taken using a vertical slit mounted close to the endwall on the test section in contrast to Fig. 13 which utilized a horizontal slit. The side wall at the bottom is not seen by the rotating drum camera because of the round corner (corner radius of 0.300") of the rectangular tubing used. However, the figure shows quite clearly a "foot" preceding the reflected shock front near the side wall. It turns out that the "foot" grows as the shock moves away from the endwall. A y-t diagram is constructed for the reflected shock from Fig. 14a and shown in Fig. 14b. y is the axis along the line of sight which is perpendicular to the side wall facing the camera. Notice

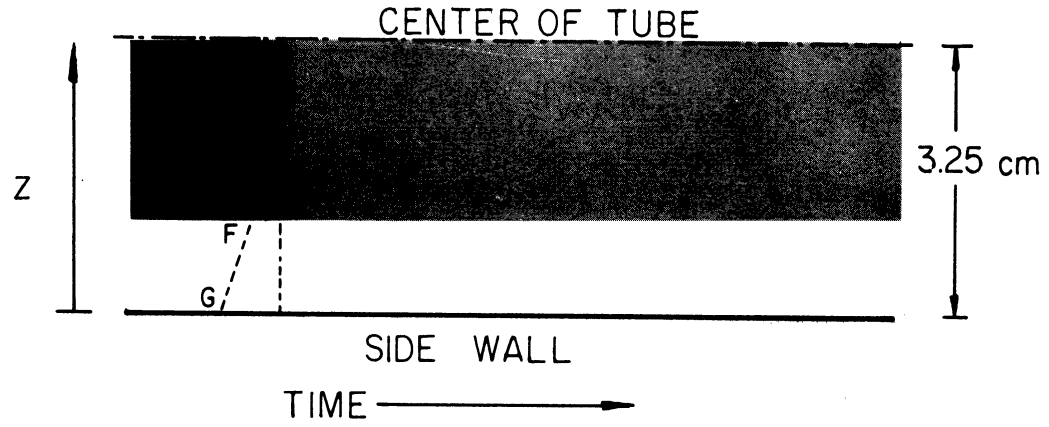

a) z-t diagram

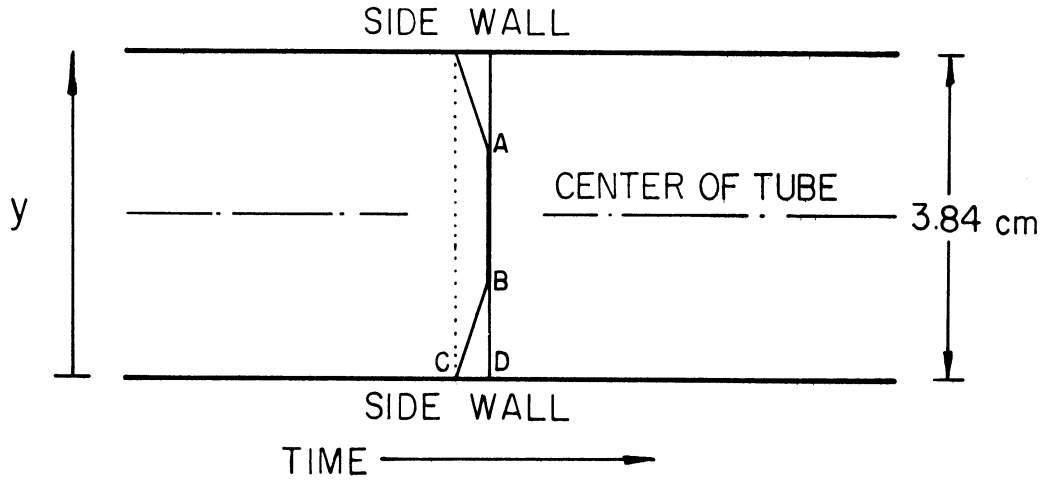

b) y-t diagram reconstructed from a)

Figure 14. Vertical slit pictures of a shock in mercury

that Fig. 14a and b differ by respective shock tube widths in the z and y directions. Fig.'s 13a, 13b, and 14b give a complete geometrical description of the reflected shock as a function of either the distance from the endwall or the time elapsed after the arrival of the primary shock at the endwall. $\overline{AB}$ in Fig. 13b and $\overline{AB}$ in Fig. 14b are an identical measure of the plane portion of reflected shock along the y-axis at a given time, except that the first is an oblique view while the latter is a full view. Let us use y_2 to denote the depth $\overline{BD}$ of the "non ideal" region of the n = 2nd shock, measured from the side wall, i.e.,

$$y_2 \equiv \overline{BD} = \tfrac{1}{2}(38.4 - \overline{AB}) \quad , \qquad \text{(III.1)}$$

where measurements are to be made in mm. Measured values of y_2 are plotted against x_2 in Fig. 15 for shocks listed in Table IV.

An inspection of Fig. 15 immediately reveals that y_2 is a quadratic function of x_2 to a good approximation. Of course, for $y_2 < 1.0$ mm, the uncertainty becomes too large for the quadratic relation to be conclusive. The proportionality constant is best expressed by variables u_1 and γ_1 of the n = 1st region. γ_1 is the specific heat ratio and is calculated using eq. (III.4) derived in the next section and Appendix B. Thus one obtains an empirical formula

$$y_2(x_2) = K \left(\frac{u_1}{\gamma_1}\right)^{\ell} x_2^{m} \qquad \text{(III.2)}$$

Table IV

Variables of Shocks Used for Bifurcation Analysis

No.	p_o cm Hg	T_o ^oK	U_1 mm/μsec	$U_2^{(o)}$ mm/μsec	T_1 ^oK	P_1 cm Hg	u_1 mm/μsec	γ_1	p_2 cm Hg
MHgVIII-11	1.953	502.9	1.457	0.225	8098	162.1	1.161	1.1992	791
-12	1.955	509.7	1.3571	0.236	7603	140.4	1.057	1.2345	616
-13	1.883	505.1	1.559	0.264	7390	124.3	1.089	1.2728	573
-14	1.822	502.3	1.560	0.236	8505	176.6	1.270	1.1744	957
-15	1.984	501.3	1.589	0.233	8640	200.4	1.297	1.1724	1099

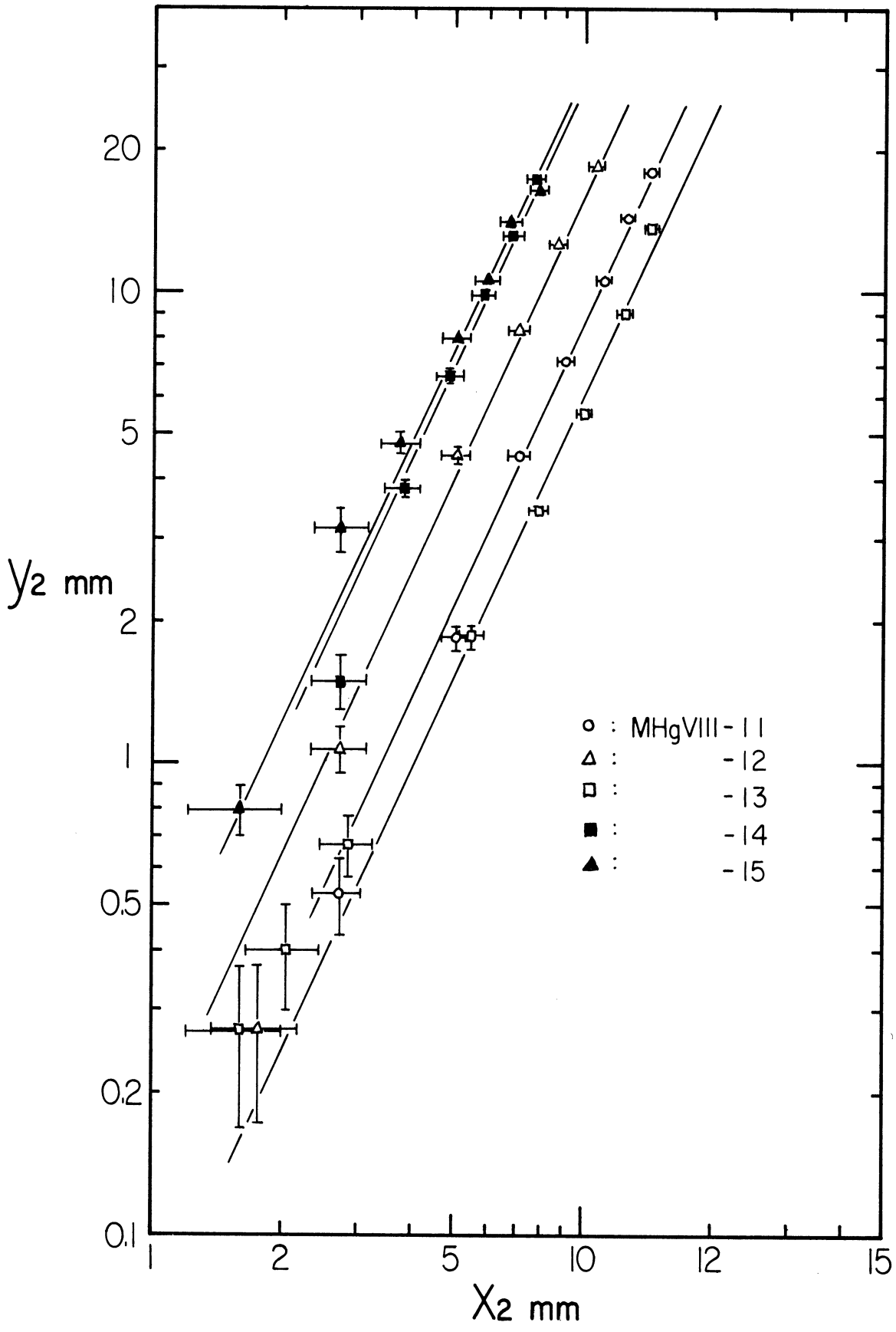

Figure 15. Depths of the "non-ideal" region of bifurcated reflected shocks as a function of distances from the endwall

where

$$K = 0.192 \pm 0.015$$

$$l = 5.23 \pm 0.40$$

$$m = 2 \pm 0.13$$

and the numerical constant, K, may depend on the type of gas and the geometry of the shock tube.

In Fig. 16, the $n = 2^{nd}$ shock profile (Series MHg VIII-12) is reconstructed for several values of x_2 from measurements of Fig. 13a and b. The angle $\theta(x_2)$ between the main shock plane and the "foot" increases with x_2, but their relation is not very clear partly due to large uncertainties in the region of small x_2. It should be noticed that $y_2(x_2)$ is merely a trajectory of a point (B or A in Fig. 14b) on the edge of the reflected shock plane, which has no direct bearing on such questions as what the boundary layer profile in the $n = 2^{nd}$ flow looks like at a given time. The flow behind the reflected shock will undergo a readjustment in the region along $y_2(x_2)$ —— that is, at a given time $y_2(x_2)$ will be spread over an area bounded by dotted lines y_2' and y_2'' as shown in Fig. 16. (Note that plots of y_2' and y_2'' are merely qualitative illustrations.)

The notion that y_2 depends on u_1 and γ_1 may seem strange at first, but it becomes more plausible if one considers how the $n = 2^{nd}$ shock is generated in the first place. The endwall of the shock tube at rest plays the role of a piston against the $n = 1^{st}$ flow moving at a speed, u_1.

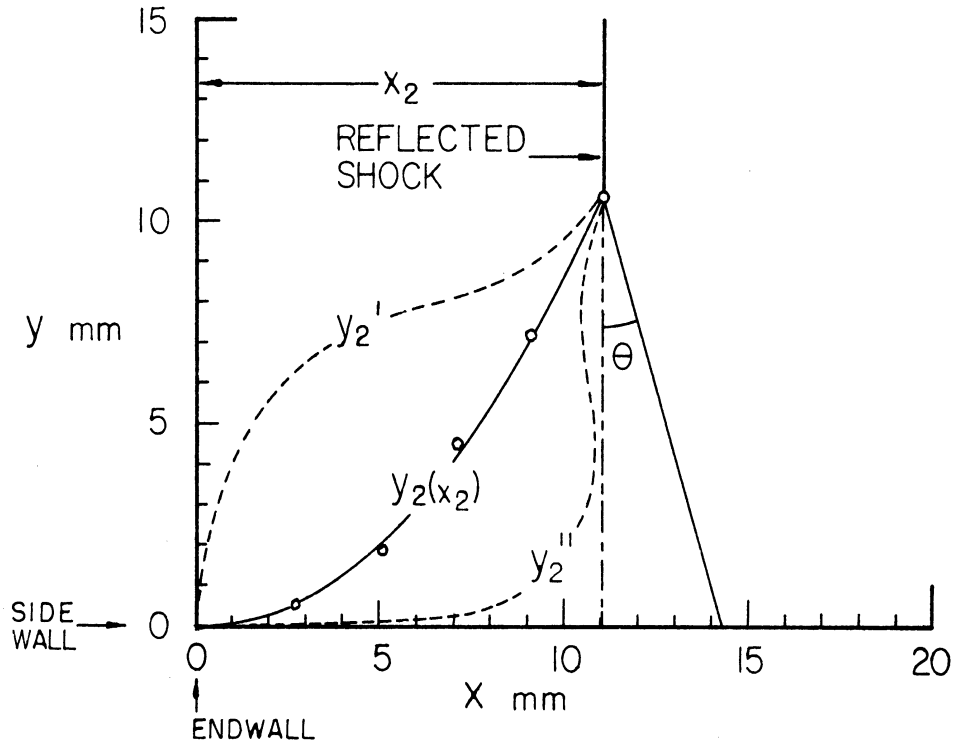

Figure 16. Profile of bifurcated reflected shock (Series MHg VIII-12)

A thin layer (on the y-z plane) of the flow immediately behind the n = 1^{st} shock front will undergo a momentum exchange with the endwall and be bounced back to be encountered by the other such layers that follow. The net effect is that the flow is brought nearly to rest after the reflection and a "pile up" of molecules takes place, resulting in a sharp rise in pressure, temperature, and density far above the n = 1^{st} state. The extent of the discontinuity in these variables is determined solely by u_1 for a given gas, neglecting the internal dissipative

processes. As more molecules are trapped into this "pile up" at a specific state, its volume increases, i.e., the surface of discontinuity moves away from the endwall, thus becoming a reflected shock.

The moving surface continues to be a surface of discontinuity because the region behind the surface (n = 2) is again supersonically separated from the region ahead, i.e.,

$$U_2 + u_1 > \sqrt{\gamma_1 R T_1 / \sigma_1}$$

The surface will be plane if and only if the primary shock flow is uniform, i.e., $\frac{\partial u_1}{\partial y} = \frac{\partial u_1}{\partial z} = 0$ along an entire span of x-axis pertaining to the primary shock zone. If the boundary layer is to grow in the flow behind the n = 1st shock to a substantial extent—that is, if the flow (n = 1) consists of a central region where $\frac{\partial u_1}{\partial y} = \frac{\partial u_1}{\partial z} = 0$ and an outer region where u_1 is smaller than it is in the center and $\frac{\partial u_1}{\partial y} = f_1(x,y,z)$, $\frac{\partial u_1}{\partial z} = f_2(x,y,z)$, the reflected shock is bound to undergo a structural change as it moves upstream, because, as pointed out earlier, the reflected shock compression in each locality is fixed by $u_1(x,y,z)$ and, as a result, the rate at which the volume of piled-up gas grows changes from point to point on the y-z plane. The portion of the reflected shock corresponding to the outer region of the n = 1st flow with lower values of u_1 compresses less than the central portion, and consequently precedes the plane portion of the shock, forming a "foot", $\overline{BC}$, in Fig. 14b.

A detailed consideration of the bifurcation phenomenon makes it possible to draw rather definite conclusions concerning the build-up of the boundary layer in the flow behind the primary shock. It is intended to present these conclusions in a separate paper.

In view of the above discussion, it can be said that strongly bifurcated shocks are not suitable for generating a uniform spectroscopic source. The hot gas of the non-ideal region in the $n = 2^{nd}$ flow absorbs the radiation from the uniform gas of the central region, resulting in strong reversals at the line centers. The continuum radiation from the central region of a strong reflected shock especially is severely affected by reversal. Its absorption profile is very broad, supporting the notion that the gas in the non-ideal region is indeed highly excited, though it is not uniform and definitely cooler than in the central region. Much of this can be said of the $n = 1^{st}$ flow, even though the line reversal is not as severe as in the $n = 2^{nd}$ flow. Instead, a fast decline in line intensity after the plateau takes place as the "non-ideal" region begins to dominate the flow. The intensity decrease instead of strong reversal is a mere consequence of the difference in temperatures and pressures of the $n = 1^{st}$ and $n = 2^{nd}$ flows, i.e., spectral lines are broadened less in the $n = 1^{st}$ flow so that the absorption in the non-uniform region appears in a less conspicuous form—a rapid decrease in line intensity.

5. γ-Model of Reflected Shock Bifurcation in Monatomic Gases

Now that the details of flows behind the bifurcated shocks have been analyzed, it is of special interest to see if one can remove the shock bifurcation and if there is any distinctive rule which sets a pattern in the appearance of the reflected shock bifurcation in monatomic gases.

As pointed out in Section 3 of this chapter, it was possible to obtain reflected shocks free of bifurcation by i) reducing the strengths of primary shocks in pure mercury gas so that equilibrium values of T_1 are of the order of 5,000 ^{o}K or less; and ii) reducing the mercury concentration in the neon-mercury mixture. "At what concentration of mercury does the bifurcation cease to appear?" is an involved question because there are yet many other variables which ultimately influence the final state behind the primary shock. However, it should be pointed out that in neon-mercury mixtures with mercury concentrations as large as 5%, strong shocks were generated with no trace of bifurcation for T_1 up to 6,000 ^{o}K.

The reflected shock bifurcation in di-and poly-atomic gases had been observed earlier by Hollyer[35], Mark[36], Strehlow and Cohen[37], Byron and Rott[38], and others. Gases dealt with ranged from N_2, O_2, NO, and CO_2 to mixtures of air-argon and N_2-argon. Most of these investigations were concerned with rather weak shocks, which at best were able to excite the vibrational modes in the shocked gas and to cause

some dissociations. Mark formulated a scheme which described the appearance of reflected shock bifurcation in terms of two critical Mach numbers—that is, the bifurcation would take place whenever the stagnation pressure of the laminar boundary layer in the primary shock flow seen in the reflected shock coordinate system becomes smaller than the equilibrium pressure behind the reflected shock. The critical Mach numbers are determined by the specific heat ratio, γ, which was considered constant at first, of the polyatomic gas in question. The existence of the lower bound in shock Mach number was substantiated by experiments (Mark), while the upper bound beyond which the bifurcation was to disappear was not confirmed by any clear-cut evidence, the supposed explanation being that the upper bound would move up higher with decreasing γ due to the excitation of vibrational modes in the gas. Byron and Rott elaborated Mark's criterion and arrived at the conclusion that γ_2 was more critical than γ_1 in the appearance of the bifurcation, and for γ_2 less than 1.52 the bifurcation would be expected for all values of Mach number above 1.5 in all gases, with the specific exception of monatomic gases.

In the light of the development in the present investigation, certain assumptions underlying those earlier developments, such as the one asserting a completely laminar boundary layer in the n = 1st flow throughout, are not completely acceptable. However, it <u>is</u> important that the specific heat ratio, γ, has something to do with the presence of the reflected shock bifurcation, because γ seems to be the

only variable which can bring together the two categories of shock bifurcation—one taking place for weak shocks of low temperature in polyatomic gases and the other occuring in monatomic gas of mercury at high temperatures. The γ -values of a monatomic gas can now become smaller than 5/3 because at high temperatures the energy can be stored in the gas internally by exciting the electronic mode and inducing the ionization. The search for one common variable which influences the shock bifurcation of both categories simultaneously of course stems from the assumption that they both are basically of an identical nature. The validity of this assumption is subject to further investigation. However, now that a greater portion of the total energy per particle is being stored in internal modes rather than in the translational mode at high temperatures, it is quite plausible to say that under these conditions variables such as the flow speed u_1 and T_1 are readily affected, for instance, by a disturbance caused by the wall at T_o, where the intensity of the disturbance is dependent on the total average energy of a particle in the free stream. γ is a measure of what fraction of the total energy exists as an internal energy in contrast to the translational energy.

The specific heat ratio, γ , can be written as

$$\gamma \equiv \frac{C_p}{C_v} = \left(\frac{\partial h}{\partial T}\right) \Big/ \left(\frac{\partial e}{\partial T}\right) \qquad \text{(III.3)}^{39}$$

where the specific enthalpy, h, and the specific internal energy, e, are defined by eq.'s (II.15) and (II.18) respectively. For doubly ionized gases, one obtains

$$\gamma\Big\{3(1+\alpha_1+\alpha_1\alpha_2)+\alpha_1(1-\alpha_1^2)\Big(\frac{5}{2}+\frac{\chi_I}{kT}+\frac{f_{EII}}{2}-\frac{f_{EI}}{2}\Big)\Big[\frac{3}{2}(1+\alpha_2)$$
$$-(2\alpha_1-\alpha_2+2\alpha_1\alpha_2)f_{EI}+(1+2\alpha_1)(1-\alpha_2)f_{EII}$$
$$+(\alpha_2+2\alpha_1\alpha_2+2\alpha_1\alpha_2^2)f_{EIII}+\frac{\chi_I}{kT}+\frac{\chi_{II}}{kT}\alpha_2\Big]$$
$$+\alpha_1\alpha_2\frac{(2+\alpha_2)(1-\alpha_1^2)}{(1+2\alpha_2)}\Big(\frac{5}{2}+\frac{\chi_{II}}{kT}+\frac{f_{EIII}}{2}-\frac{f_{EII}}{2}\Big)\Big[\frac{3}{2}+(1-\alpha_1)f_{EI}$$
$$-(1+2\alpha_1\alpha_2)f_{EII}+(1+\alpha_1+2\alpha_1\alpha_2)f_{EIII}+\frac{\chi_{II}}{kT}\Big\}$$
$$=5(1+\alpha_1+\alpha_1\alpha_2)+\alpha_1(1-\alpha_1^2)\Big(\frac{5}{2}+\frac{\chi_I}{kT}+\frac{f_{EII}}{2}-\frac{f_{EI}}{2}\Big)\Big[\frac{5}{2}(1+\alpha_2)$$
$$-(2\alpha_1-\alpha_2+2\alpha_1\alpha_2)f_{EI}+(1+2\alpha_1)(1-\alpha_2)f_{EII}$$
$$+(\alpha_2+2\alpha_1\alpha_2+2\alpha_1\alpha_2^2)f_{EIII}+\frac{\chi_I}{kT}+\frac{\chi_{II}}{kT}\alpha_2\Big]$$
$$+\alpha_1\alpha_2\frac{(2+\alpha_2)(1-\alpha_2^2)}{(1+2\alpha_2)}\Big(\frac{5}{2}+\frac{\chi_{II}}{kT}+\frac{f_{EIII}}{2}-\frac{f_{EII}}{2}\Big)\Big[\frac{5}{2}+(1-\alpha_1)f_{EI}$$
$$-(1+2\alpha_1\alpha_2)f_{EII}+(1+\alpha_1+2\alpha_1\alpha_2)f_{EIII}+\frac{\chi_{II}}{kT}\Big] \qquad (III.4)$$

where it is assumed that

$$\left| f_{Ez}^2 - \left\langle \left(\frac{2E_E}{kT} \right)^2 \right\rangle \right| \ll f_{Ez} \quad , \quad z = \mathrm{I}, \mathrm{II}, \mathrm{III}, \cdots$$

See Appendix B for the complete derivation. γ of ionized mercury is calculated using eq. (III.4) for p = 50, 500, and 5,000 cm Hg, and is plotted in Fig. 17. The pressure dependence of γ originates mainly from that of the α's via equations of ionization equilibrium (see Chapter II). Dips in the plot of γ correspond to respective ionizations and the separation in the temperature scale between two neighboring minima of γ is determined roughly by the ratio of ionization potentials concerned. Note that once the ionization becomes active the change in γ is more strongly influenced by the ionization rather than the electronic excitation. Recalling that in the pressure range of shock tube flows the successive degrees of ionization of mercury overlap considerably (see Fig. 7), the return of γ-values to 5/3 in between consecutive ionizations seems unlikely, and it indeed proves to be the case as shown in the figure. γ continues to fluctuate more or less around 1.2 as T increases beyond 7,000 ^{o}K.

According to the γ-model of reflected shock bifurcation, it appears extremely unlikely that the bifurcation will disappear at all at higher temperatures, i.e., for stronger shocks in mercury. In fact, the reflected shock bifurcation had been observed for all shocks in pure mercury gas whose equilibrium temperature, T_1, exceeded 6,000 ^{o}K, and it began to disappear as T_1 decreased below approximately 5,000 ^{o}K.

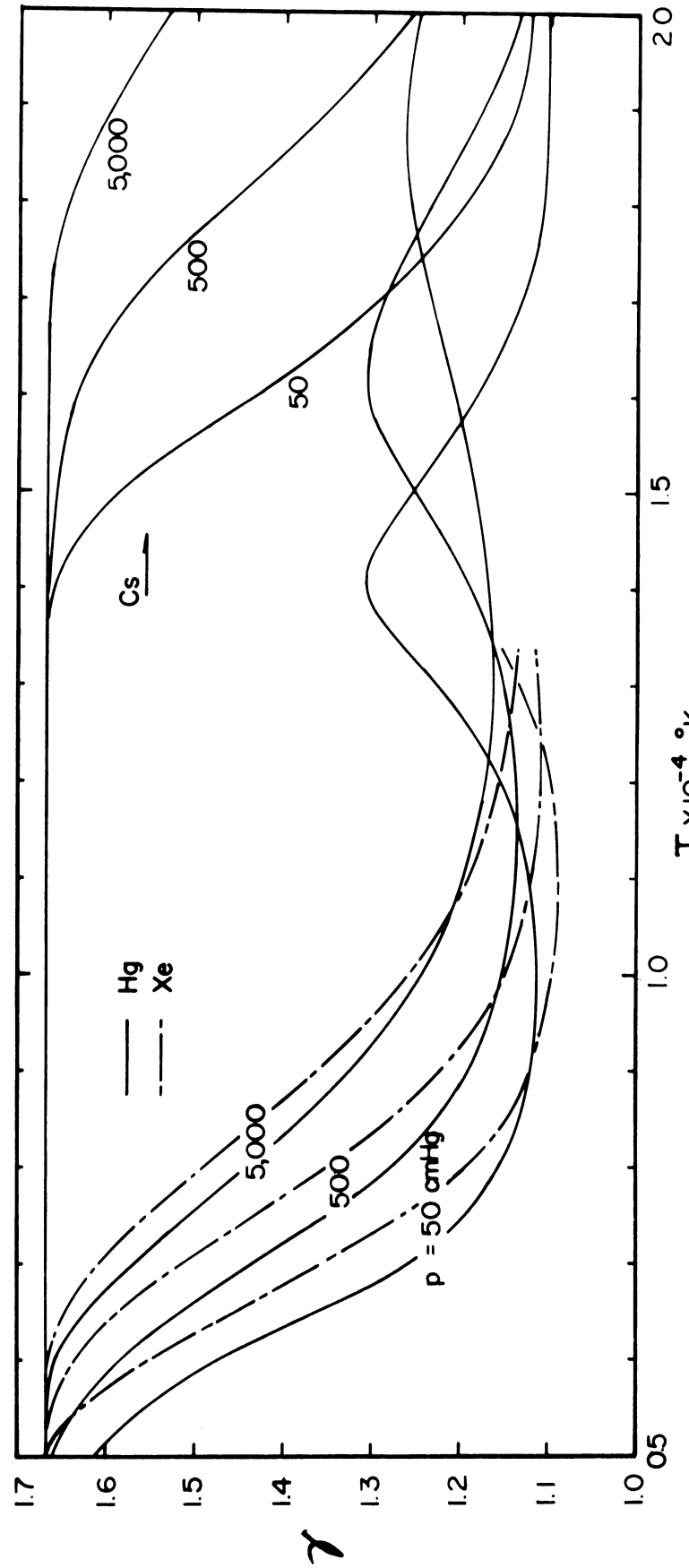

Figure 17. Calculated specific heat ratios for mercury, xenon, and cesium as a function of temperature

Similar calculations were made for xenon as shown also in Fig. 17. It shows that if the γ-model works properly for mercury one shold expect the bifurcation to happen for strong shocks in xenon. Such shots in research grade xenon were made in the luminous shock tube of this laboratory (used earlier by Turner, Doherty, Wilkerson, Charatis, and Brown), and the bifurcation in xenon was observed. In order to confirm earlier observations of the bifurcation in polyatomic gases, strong shocks (all luminous in this case) in air and air-neon mixtures were generated in the luminous and heated shock tubes and all showed the reflected shock bifurcation.

One may conclude at this point that the specific heat ratio of an ionized gas will remain for large temperature intervals far smaller than 5/3 if successive ionization potentials of the atom are not very much different from each other as is the case for mercury and xenon; therefore bifurcation will persist. The experimentally established method of removing the bifurcation (by means of depressing the ionization) is not very significant in view of the fact that one of the main objectives of the present investigation is to find a source of very high temperature in a local thermodynamic equilibrium. Instead, a search for another heavy evaporable element expressly with widely separated first and second ionization potentials led us to cesium as a shock medium. Its first and second ionization potentials are 3.893 and 23.45 eV, respectively, and as one sees they differ from each other much more than the corresponding values

for mercury, which are 10.434 and 18.75 eV. γ for cesium has been calculated accordingly and is plotted in Fig. 17. γ undergoes a sharp drop at about 4,000 ^{o}K(not shown in the plot) and resumes the value of 5/3 from 5,000 ^{o}K to 15,000 ^{o}K. It appears possible to generate a strong shock in cesium gas free of any fast-growing boundary layer, which produces a high density, high temperature (5,000 ^{o}K to 15,000 ^{o}K) plasma in a local thermodynamic equilibrium consisting only of the first ions of cesium and electrons behind the primary shock. This would make it possible to have an even denser and hotter plasma behind the reflected shock, free of the bifurcation.

It is proposed to undertake an investigation of shocks in pure cesium, involving a heated shock tube capable of functioning at an ambient temperature of 600 ^{o}C or higher. Bits of technical know-how and constructional materials employed in the present heated shock tube should prove useful and nearly sufficient for such a new project. It would constitute a decisive test of the validity of our understanding of the reflected shock bifurcation in ionized monatomic gases.

CHAPTER IV

IONIZATIONAL RELAXATION IN SHOCKED MERCURY GAS

1. Introduction

In Chapter II it was pointed out that the shocked gas undergoes a period during which the system is initially far removed from complete local thermodynamic equilibrium but approaches it gradually. In other words, after the shock has passed, it is possible to speak of several different "effective temperatures" pertaining to various species (atoms, ions, and electrons) and internal modes (atoms and ions in various electronic states). Generally speaking, the length of the relaxing period depends on the characteristic energies and the effectiveness of the collisions that carry out the energy equilibration among all particles.

The ionizational relaxation in shocked mercury gas in particular takes place for the following reason: at an equilibrium temperature of 11,000 ^{o}K behind a typical strong shock in pure mercury the average translational energy is approximately 1 eV, which is far too small to knock an orbital electron of a mercury atom in the ground state over the potential barrier of 10.434 eV. The number of particles having energies as high as 10.434 eV amounts to only one per $e^{9.4}$ particles with the average energy, while the equilibrium degree of ionization is expected to be over 45% for p = 100 cm Hg. Therefore, a large number of neutral mercury atoms need to undergo many elastic collisions to

accumulate enough energy before scoring the ionizing collisions—a process which takes time because the collision frequency is finite and determined by the equilibrium condition.

It has become generally known through studies by a few earlier investigators[33,40] that the ionization equilibrium in a shocked gas comes about by two different processes: i) the atom-atom collisions and ii) the electron-atom collisions. The electron-atom process is known to be more effective in ionizing a gas than the atom-atom process, but this process can take place only when the gas contains a sizable number of electrons initially. Naturally, the first process is considered to play the role of supplying electrons at a rather slow rate,* and it turns out that it decisively dominates the rate of ionization as long as the electron density stays less than 10^{-5} times** the number density of atoms; the second becomes fully rate-controlling as the electron density*** goes beyond 10^{-3} times the atom density. In the intermediate region the two porcesses are mixed and more or less equally active.

---

* There are indications that the atom-atom process is not the only mechanism which supplies electrons necessary for the electron-atom process to become active. See Section 3.

** This figure is so conservative an estimate that the chance of the other process occuring concurrently is practically non-existent.

*** A time-dependent density during the relaxing period—not the equilibrium density.

Since the average particle energy is much lower than the ionization potential and since there are also many intermediate electronic levels in an atom, it is very possible that each of the two previously mentioned processes consists of two or more steps leading to the ionization. Earlier measurements[41] of the ionizational relaxation times in shocked gases such as argon, krypton, and xenon pertaining strictly to the atom-atom collisions show that a two-step process is actually taking place, the first step being the excitation of the atom from the ground state to an intermediate excited state and the second leading the atom in the excited state to ionization. The intermediate potential for each case coincides well with the group of first excited states above the ground state. Another experiment[42] on cesium-argon mixtures (argon constituting more than 97% of the mixture remains practically neutral) shows that the same holds true for the electron-atom process. The present experiment on mercury strongly supports the indications stated thus far as will be discussed in detail in the following sections.

2. Measurements of the Ionizational Relaxation Time in Mercury

Measuring the ionizational relaxation time utilizing the shock tube is relatively easy and free of complications because i) the strong shock "turns on" a high temperature in the gas of interest, establishing a translational

equilibrium among all atoms approximately within 0.01 μsec;[33] ii) the ionization is the slowest of all internal excitations; and iii) yet the ionization and electronic excitations are so closely related that the progress of ionization can be monitored by means of the time-dependent light intensity of emission from the shocked gas.*

It is often observed that impurities may obscure the whole phenomena through the violation of the point iii) above. In this respect the heated shock tube is especially appropriate for this type of investigation because the impurity level can be kept low through an extensive baking and pumping.

Fig. 18a is a schematic reproduction of typical wave speed pictures for shocks in pure mercury. The region between the shock and luminosity fronts corresponds to the relaxing period of ionization because in pure mercury there are only three modes of excitation—translational, electronic, and ionizational. In view of the fact that the flow speed is lower than the shock speed, i.e., from eq. (II.10)

$$\frac{v_1}{v_0} = \frac{U_1 - u_1}{U_1} = \frac{\rho_0}{\rho_1} \qquad \text{(IV.1)}$$

the spacing, Δt, between the two fronts along the time axis is not the relaxation time, τ, itself but gives rise to τ in the following manner: noting that in Fig. 18a the group

---

* In the case of low electron density ($< 10^{13} cm^{-3}$) the microwave reflection-transmission technique can be used.[41]

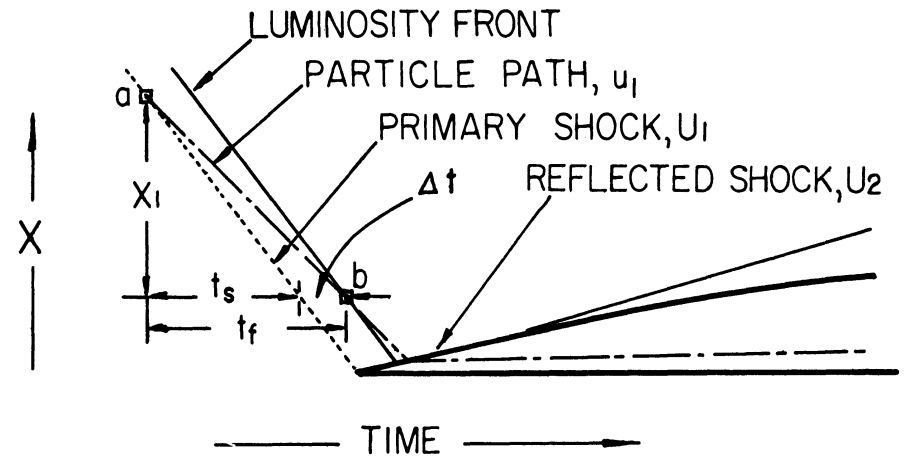

a) Wave speed pictures and ionizational relaxation time

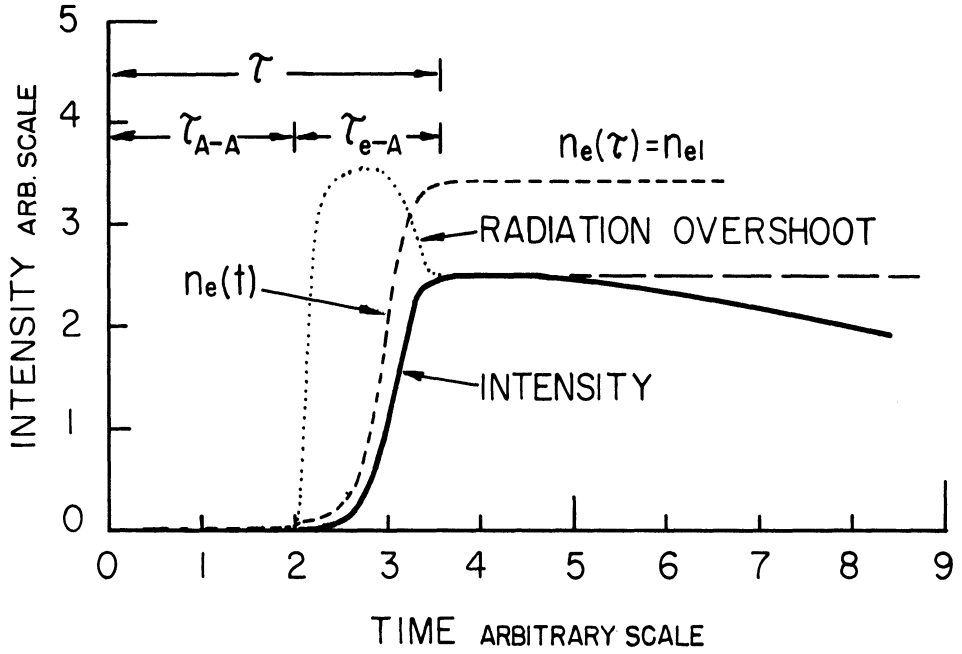

b) Relaxation time and intensity profile (in time)

Figure 18. Illustration of ionizational relaxation time in relation to flow variables and intensity

of particles at b was shocked earlier at a, one may write

$$(t_f - t_s) : \Delta t = t_f : \tau$$

to obtain

$$\tau = \frac{U_1}{U_1 - u_1} \Delta t = \frac{\rho_1}{\rho_0} \Delta t \qquad \text{(IV.2)}$$

where

$$U_1 = \frac{x_1}{t_s} \quad , \quad u_1 = \frac{x_1}{t_f}$$

In Fig. 13a, an actual wave speed picture exhibiting the relaxation time is shown. The primary shock front is not visible in the case of pure mercury gas in the heated shock tube, providing stong evidence that the impurity level is low.* However, the reflected shock front can be identified at the endwall, thus making it possible for one to locate the primary shock front and in turn to measure Δt. The ionizational relaxation time associated with the reflected shock is very short because T_2, the temperature behind it, is higher than T_1, the temperature behind the primary shock. Also the reflected shock front goes through a medium which has a substantially large number of electrons provided by the primary shock.

Recalling the processes of ionization described earlier,

---

* The primary shock front in the luminous shock tube is visible due to the molecular spectra of impurities. These have very short relaxation times.

one can write approximately

$$\tau = \tau_{A-A} + \tau_{e-A} \qquad \text{(IV.3)}$$

where τ_{A-A} stands for the period of the atom-atom process, and τ_{e-A} for that of the electron-atom process. Fig. 18b shows (only schematically!) a tracing of the spectral intensity across the shocked zone along the time axis. The shock front is presumed to be at the origin of the t-axis. The solid line shows a typical time-resolved intensity profile* for the pure shocked mercury gas. The intensity plateau is briefly maintained, indicating that the establishment of an equilibrium distribution is complete, and decreases steadily due to the boundary layer growth as extensively described in Chapter III. Notice that the so-called radiation overshoot which is commonly observed in luminous shock tube experiments is absent in the present case. It occurs when the upper levels of atoms become temporarily overpopulated beyond the equilibrium population due to the presence of impurities sizable in number density in comparison with the density of emitting atoms (its detailed mechanism will be discussed in the following section). The absence of radiation overshoot constitutes further evidence of the very low impurity level in the heated shock tube.

---

* Note that the white light from shocked mercury has practically the same profile as that of any neutral mercury line (at least in the visible region), meaning that the shock excitation of electronic modes is indiscriminatory. This check was made by taking wave speed pictures through a number of interference filters.

Also shown in the figure is the electron density, its increase being closely represented by the spectral intensity rise. When $n_e(t)/n^o_{Hg}$ begins to exceed 10^{-3} as a result of, e.g., the atom-atom process, the electron-atom process is likely to take over and continue to produce mercury ions until

$$\frac{n_e(t)}{n^o_{Hg}} \longrightarrow \frac{n_{e1}}{n^o_{Hg}} = \alpha_{Hg1}$$

All together thirteen shots in pure mercury were used to determine the pattern of ionizational relaxation as a function of thermodynamic variables, which are listed in Table V. The plot of τ versus $1/T_1$ in Fig. 19 yields a straight line and shows hardly any dependence of τ on such variables as p_1, n^o_{Hg}, and n_{e1}, despite the fact that each of these variables varies extensively. The slope of the straight line gives rise to the so-called activation energy of the ionizational relaxation, i.e.,

$$\tau = \text{const.}\ n^{o\,-\delta}_{Hg}\ e^{\frac{E_a}{kT}} \qquad \text{(IV.3)}$$

where the activation energy is found to be

$$E_a = 4.88 \pm 0.28 \text{ eV}$$

and

$$\delta = 0.00 \pm 0.04$$

δ in particular is found by plotting $\tau\, e^{-Ea/kT}$ versus n^o_{Hg}.

Table V

Measured and Related Variables

Series	p_o cmHg	T_1 °K	p_1 cmHg	ρ_1/ρ_o	n^o_{Hg1} cm^{-3}	n_{el} cm^{-3}	τ μsec
MHgVIII- 7	1.103	7818	88.24	4.902	1.069×10^{18}	3.70×10^{16}	11.221
8	1.112	8214	103.1	5.322	1.146 "	5.85 "	9.069
9	1.091	8236	101.5	5.362	1.123 "	5.93 "	8.02
10	1.162	8313	110.9	5.425	1.217 "	6.27 "	9.722
11	1.953	8098	162.1	4.913	1.856 "	6.62 "	11.143
12	1.955	7603	140.4	4.515	1.742 "	3.57 "	18.679
13	1.883	7390	124.3	4.383	1.548 "	2.81 "	18.908
14	1.822	8505	176.6	5.380	1.890 "	1.02×10^{17}	7.979
15	1.984	8640	200.4	5.484	2.104 "	1.22 "	5.758
16	1.166	10493	254.3	8.535	1.902 "	4.23 "	2.140
17	0.5704	10962	172.1	10.205	1.093 "	3.97 "	1.733
21	1.240	10347	259.7	8.372	1.994 "	4.21 "	2.240
22	1.688	8244	148.9	5.142	1.661 "	7.36×10^{16}	9.411

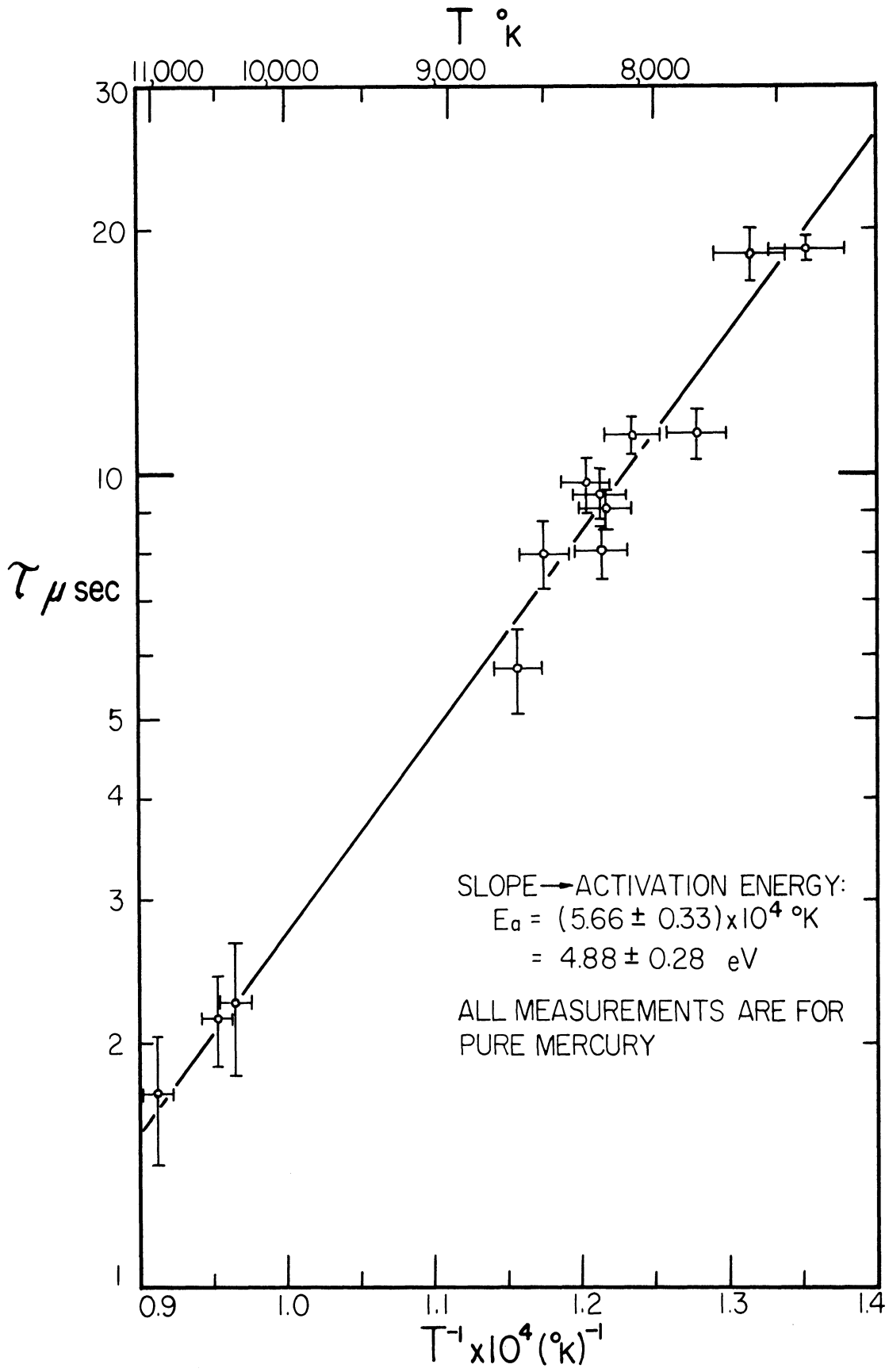

Figure 19. Ionizational relaxation times as a function of equilibrium temperatures

δ being zero is not exactly an obvious outcome because one tends to think that the greater the number of particles, the more frequent the ionizing collisions would get, thus speeding up the ionizational relaxation. In order to explore the matter further, mercury-neon mixtures were used as the shock medium, the mercury concentration varying from 4 to 50%. Over the temperature range (T_1) of 6,900° to 8,400 °K the value of activation energy remained unchanged and practically the same as for the case of pure mercury. But δ -value showed a distinctive dependence on the equilibrium electron density, which are summarized as follows:

$$\delta = 0.86 \pm 0.11 \text{ for } n_e = (4 \sim 5.2) \times 10^{15} \text{ cm}^{-3}$$

where n_{Hg}^o varied from 4.4×10^{16} to 1.3×10^{17} cm^{-3}, and

$$\delta = 0.39 \pm 0.09 \text{ for } n_e = (1.4 \sim 3) \times 10^{16} \text{ cm}^{-3}$$

with n_{Hg}^o ranging from 9.3×10^{16} to 6.3×10^{17}. Throughout the runs of mixtures a small amount of tetramethylsilane (0.046 to 0.069%) was added in the shocked zone in accordance with the requirements for flow variable measurements.

3. Interpretation of Results and Comparison with Other Related Experiments

In their investigation of the ionization rate of argon, krypton, and xenon, Harwell and Jahn[41] treated the atom-atom collisions as the sole mechanism of ionization by choosing

the shock variables in such a way that the equilibrium electron density was of the order of 10^{13} cm^{-3} or lower. Incidentally, 10^{13} cm^{-3} also represents the upper limit to the microwave technique of measuring electron density, which Harwell and Jahn employed. Their findings are noteworthy, though hardly unique: i) for all three elements the measured activation energy embraces unmistakably a number of first excited states of each element, indicating that the atom-atom collision for ionization is very likely to be a two step process, at least in the case of the noble gases; and ii) the dependence of the ionization rate on the number density of atoms is "nearly" quadratic, or the ionizational relaxation time is inversely proportional to the number density of atoms.

Somewhat earlier Haught[42] reported his observation of ionizational relaxation of cesium using shocks in cesium-argon mixtures (cesium concentration of 0.50 to 2.60%). For an electron density range of 2.0×10^{15} to 8.5×10^{15} cm^{-3}, the relaxation time attributed to the atom-atom process, τ_{A-A}, yielded $\delta = 0.61 \pm 0.05$, while τ_{e-A} of the electron-atom process showed no remarkable pressure dependence, i.e., $\delta = 0.00 \pm 0.11$. τ_{A-A} and τ_{e-A} both shared one activation energy which was again in the neighborhood of first excited states of neutral cesium. τ_{A-A} was greater than τ_{e-A} by a factor of 1.6 to 4.4. In measuring τ_{e-A}, Haught identifies the radiation overshoot as the period of the electron-atom process as shown in Fig.18b, by arguing that the internal excitation responsible for the emission of spectral lines

is a faster process than the ionization so that once the electron-atom process begins to dominate, the upper level population of cesium temporarily exceeds the equilibrium population.

The indication from the present study is that the identification of τ_{e-A} with the time span of the radiation overshoot is acceptable, but its reason given above is of doubtful nature. No radiation overshoot is observed in pure mercury, or in mixtures of neon and mercury, with the mercury concentration as low as 2%. To produce the radiation overshoot, let us take this 2% mercury and neon mixture and gradually add more and more of tetramethylsilane. At first still no radiation overshoot will be seen. It is not until the tetramethylsilane content reaches 10% of the mercury concentration (or 0.02% of neon) that this phenomenon is observable. One may speculate at this point that the role of impurities is dual, one being the excitation of emitting atoms to the point of overpopulation in upper levels through direct impurity-atom collisions during the electron-atom process, the other being the excitation through collision of emitting atoms with additional electrons* supplied by the impurities whose ionization rate is greater. However, the latter explanation is the likelier choice because at first the presence of neon, for instance, does not cause the

---

* The electrons thus freed from the impurity atoms during the electron-atom process of the emitting atoms will not quite have the chance to become highly energetic when they begin to interact with the emitting atoms.

radiation overshoot at any level of concentration, and secondly, the impurity elements such as silicon and carbon are indeed ionizable faster than mercury.* Also one should observe that typical impurities in the luminous shock tube are elements of low ionization potentials such as sodium (5.138 eV), and potassium (4.339 eV), in contrast to the emitting elements of higher ionization potentials such as chromium (6.761 eV)and lead (7.415 eV) whose spectral lines showed the radiation overshoot.[15,17]

In Fig. 20 the energy level diagram for argon, krypton, xenon, cesium, and mercury are shown in a normalized scale through division by the respective ionization potential. The measured activation energy E_a is in each case indicated by a small box of dotted lines surrounding a few of the first excited states. It is clear from Fig. 20 that in each case the activation energy closely agrees with the group of first excited states. This is not a unique aspect for the inert gas as was thought by Harwell and Jahn, but holds true for all five elements. It should be noted especially that the ground to first excited state energy gap in cesium amounts to only 35.6% of its ionization potential. None the less it is important that the largest gap between two neighboring levels is that of the ground to first excited states so that the

---

* The atomic species of silicon and carbon are made available through the dissociation of tetramethylsilane. It is well known that such a dissociation does not produce atoms in the ground state alone, but it provides many atomic species in excited states, making them even more favorable agents in exciting the emitting atoms.

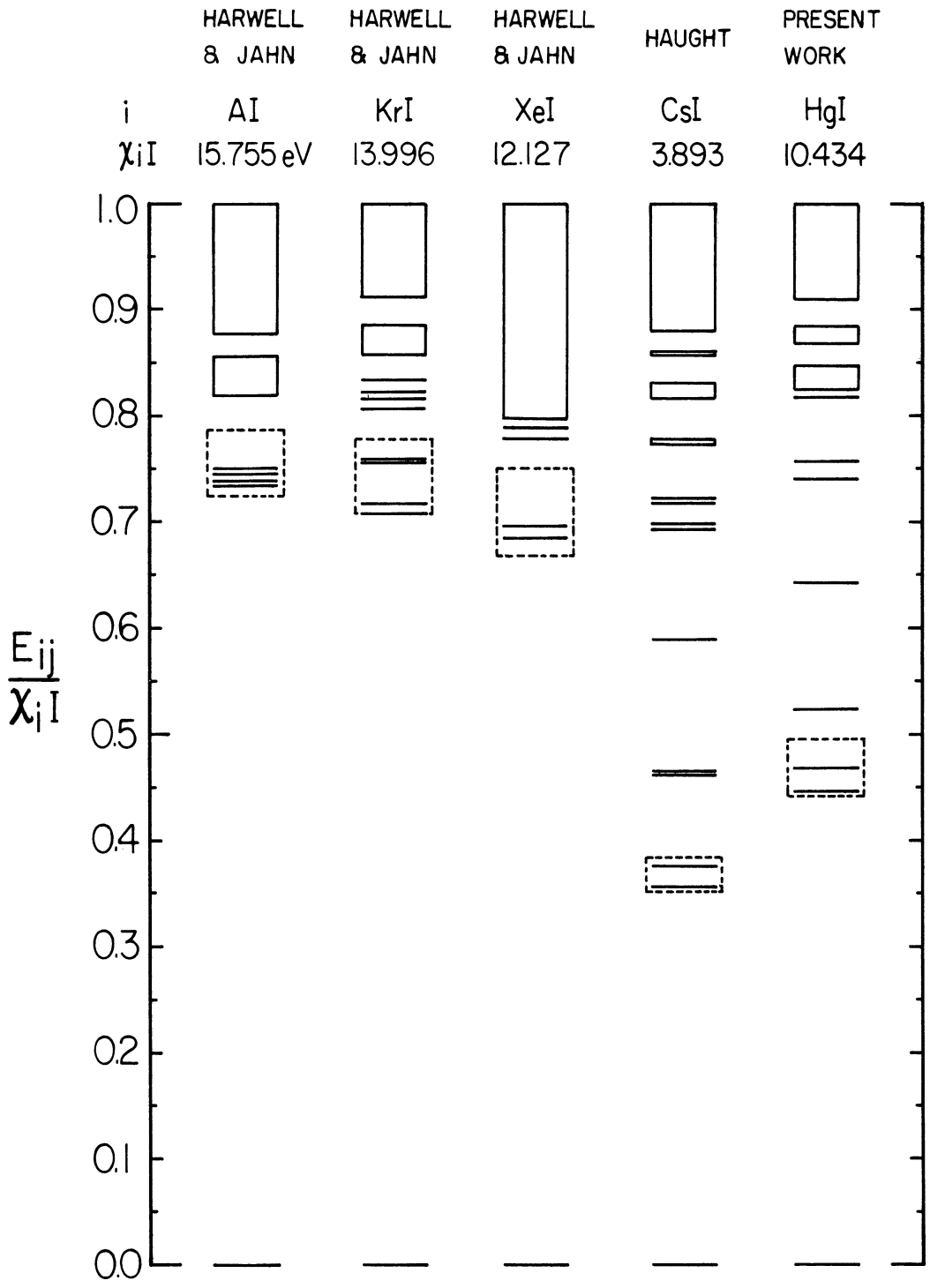

Figure 20. Energy level diagrams and activation energies of argon, krypton, xenon, cesium and mercury

population in the first excited states constitutes the majority of the population of all excited states. In other words, the rate at which the first excited states are populated will determine the ionization rate in the atom-atom process as well as in the electron-atom process.

Moreover, it is fair to conclude that the pressure dependence of the ionizational relaxation time is characteristic of the atom-atom process, whereas the electron-atom process was found previously to be independent of the pressure. In this context, the empirical relation of eq. (IV.3) can be understood as an indication that for equilibrium electron densities exceeding 3×10^{16} cm^{-3} the ionizational relaxation in shocked mercury gas is predominantly an electron-atom process. This is further substantiated by the results from the neon-mercury mixtures mentioned earlier, results which showed that as the equilibrium electron density decreases, the role of the atom-atom process gradually becomes significant, and it finally begins to dominate when n_{el} reaches the level of 5×10^{15} cm^{-3}.

A recent theoretical calculation on the electron-mercury atom collisions shows that the total excitation cross sections from $6s^1S$ to $6p^3P_o^o$, $6p^3P_1^o$, and to $6p^3P_2^o$ (see Fig. 24) are large and almost linearly proportional to electron energies in the range of energies slightly greater than the energy level difference involved in the respective excitation.[43] Earlier experimental results on the total ionization cross sections by electron impact showed a similar energy dependence.[44] These results are consistent with the present

picture of two-step processes of ionization. It is possible to show by writing out the ionization rate equation based on the Maxwellian distribution among participating particles of each kind, that the activation energy is indeed the resonance energy as has been found in the present investigation. On the other hand, the fact that τ is independent of the pressure in the electron-atom process does not find any straightforward explanation at the moment, although a detailed numerical calculation of the ionization rate using the available cross sections appears capable of providing an explanation.

One more question that remains to be answered is what mechanism actually provides the electrons that are necessary in initiating the electron-atom process in the case of shocked pure mercury. The atom-atom process appears an extremely unlikely one in this role in the light of the fact that i) there is not any evidence of the pressure dependence of τ as emphasized earlier and ii) actual densitometer tracing of time-resolved spectral (or white light) intensities fails to show any sign of τ_{A-A} period. An alternative is the process of photo-excitation and -ionization and in fact this is rather favorable in view of the fact that i) oscillator strengths of neutral mercury lines are generally large, thus making the photo-excitation and -ionization cross section large (see Chapter V), ii) the spectral radiation field originating from shocked mercury gas is very strong due to high equilibrium temperature and pressure behind the primary shock, and iii) the continuum emission, arising

from the recombination of mercury ions and electrons in the equilibrium zone, has been observed to be strong especially in the neighborhood of the resonance line of 2537 Å for all shocks dealt with in this analysis. It is very likely that the actual photo-ionization process takes place in the dark region between the shock front and the equilibrium zone because it is optically denser than the region ahead of the shock. Of course, a mild photo-excitation can take place far ahead of the shock during a period often lasting as long as 1 msec.

CHAPTER V

MEASUREMENT OF OSCILLATOR STRENGTHS OF NEUTRAL MERCURY LINES

1. Introduction

The program of measuring oscillator strengths of neutral mercury lines has been carried out for two different reasons. One is to demonstrate the relevance of the heated shock tube as a spectroscopic source for handling metallic elements in the gaseous phase either by letting them evaporate in the tube or by relying upon such agents as metallo-organic compounds that can be evaporated at the shock tube temperature. The other reason is that measured oscillator strengths of mercury available in the literature[45,46] have rather questionable accuracy in spite of a few notable attempts in the past largely because the spectroscopic sources employed for those measurements lacked the local thermodynamic equilibrium which is essential to the evaluation of level populations. Absolute oscillator strengths are of special interest in astrophysics for the measurement of elemental abundances in the stellar atomosphere.

The spectroscopic measurement with which we are concerned here is performed in the region behind the $n = 2^{nd}$ shock because the flow comes nearly to rest in this region, the equilibrium temperature is high enough to excite most of the neutral mercury lines, and the duration of the hot flow is long enough for the completion of measurements. In order to make

certain of the presence of a local thermodynamic equilibrium in this region, one must observe the following points: i) the shock strength should be chosen in such a manner that the ionizational relaxation time of the species in question is substantially shorter than the duration of the $n = 2^{nd}$ flow, and all other relaxation times that may be present are shorter than that of the main species or much longer; ii) the impurity level should be maintained low so that the contribution of electrons by the impurity toward the equilibrium electron density stays minimal—especially so when its relaxation time is shorter than that of the main species; iii) the specific heat ratio, γ_1, of the flow behind the $n = 1^{st}$ shock must be kept very close to the ideal gas value of 5/3 so as not to encourage the growth of the boundary layer in the $n = 1^{st}$ region and in turn the occurrence of the reflected shock bifurcation.

As discussed in Chapter IV, a violation of the second requirement above leads to the radiation overshoot which would interfere with the absolute intensity measurement. The third requirement can be met by diluting the mercury gas with an inert gas (neon in this case) which also helps to keep the shocked gas from becoming excessively optically thick.

2. Preparation of the Shock Medium

The typical shot is made in a mixture of neon, mercury, and tetramethylsilane ($Si(CH_3)_4$) with helium as the driving

gas. p_o varies from 0.950 to 1.950 cmHg, while T_o is maintained at 505 ^oK with only a few degrees variation. As far as the impurities deposited on the inner wall of the tube are concerned, the shock tube is made spectroscopically clean by means of continuous baking and pumping over several thousand hours at temperatures of 200° to 320 ^oC and by means of numerous previous shots. The concentration of mercury and tetramethylsilane in neon range from 2.3 to 6.7% and from 0.023 to 0.060%, respectively.

T_1 lies between 4,900° and 6,000 ^oK, while T_2 varies from 8,500° to 10,200 ^oK. The reason for using $Si(CH_3)_4$ as an additive is that at T_1 in the above range the ionizational relaxation time is so long and the level population so low that the method of using the shock luminosity for the flow diagnosis is difficult without the aid of a molecular spectrum from a suitable compound such as $Si(CH_3)_4$. Tetramethylsilane is a colorless, toxic liquid with a very low boiling point (26.6 ^oC). Ample precaution must be taken in containing its vapor because there is much evidence that the vapor reacts (dissolves!) with silicone vacuum grease, thus causing a leak in the vacuum cock seal.

Preparing the mixture of neon and gases of mercury and tetramethylsilane calls for some attention mainly because of the presence of mercury. The following procedure has proved to be suitable:

i) Prepare a mixture of neon and $Si(CH_3)_4$ gas with the silicon concentration of 0.3 to 1.5% in a 1-liter flask at room temperature. The pressure of the mixture is about

one atm. The reason for making the Si-concentration much higher here than its final concentration is to keep the influence of the adsorption of $Si(CH_3)_4$ to the flask wall on the resultant concentration minimal after the passage of several hours from the time of preparation.

ii) Dilute the mixture prepared in step i) with neon to the final silicon concentration in a stainless steel container installed within the furnace and connected to the expansion tube via a bakable vacuum valve. This should be done only a few minutes before firing the shot. The pressure of the resultant mixture should be such that after its release into the expansion tube the resultant pressure becomes only a few percent short of the anticipated final pressure, p_o. During this step the vacuum of the expansion tube should remain unaffected.

iii) Introduce mercury gas into the expansion tube (now the pumping system is disconnected) to a designated pressure (on the order of 0.05 cmHg) from the mercury reservoir also installed within the furnace. The mercury gas pressure is measured by means of the stainless steel sylphon bellows gauge.

iv) Release the diluted mixture in the container into the expansion tube and measure the final pressure, p_o, with the bellows gauge. Measured p_o generally agrees well with the pressure predicted in the course of preparation. Allow at least two minutes between steps ii) and iv) in order for the diluted mixture to come to a thermal equilibrium at T_o.

The molecule $Si(CH_3)_4$ is thermally unstable and in fact decomposes completely above 800 °C.[47] It is then reasonable to assert that the molecule undergoes a complete dissociation into its constituent atoms all in the gaseous phase behind the n = 1st shock, i.e.,

$$\underset{\text{gas}}{Si(CH_3)_4} \longrightarrow \underset{\text{gas}}{Si} + \underset{\text{gas}}{4C} + \underset{\text{gas}}{12H} - 30.6\ eV \qquad (V.1)^{48}$$

The large value of the effective dissociation potential does not undermine the assertion because the complete dissociation is brought about in many intermediate stages, each with a small dissociation potential.

The change in the effective molecular weight due to the dissociation and ionization of all species involved can be written for this particular mixture as

$$\frac{1}{\sigma_{n,o}} = \prod_{n=1}^{n} \frac{\sigma_{n-1}}{\sigma_n}$$

$$= \left(1 - C^{\circ}_{Si(CH_3)_4} - C^{\circ}_{Hg}\right) + C^{\circ}_{Hg}\left(1 + \alpha_{Hg1} + \alpha_{Hg1}\alpha_{Hg2}\right) \qquad (V.2)$$

$$+ C^{\circ}_{Si(CH_3)_4}\left[1 + \alpha_o\left(16 + \alpha_{Si1} + \alpha_{Si1}\alpha_{Si2} + 4\alpha_{C1} + 12\alpha_{H1}\right)\right]$$

where α_o stands for the degree of the dissociation of eq. (V.1) and is asserted to be unity. This ratio must be evaluated to complete the calculation of thermodynamic variables behind the n = 2nd shock from measured U_1 and U_2 and initial conditions. If one wishes to neglect the influence of tetramethylsilane and if this is justifiable,

an approximation can be made by setting $C^{o}_{Si(CH_3)_4} = 0$ in eq. (V.2) and by disregarding all contributions of Si, C, and H toward the specific internal energy (see eq. (II.7)) throughout the shock calculation. But this approximation is not advisable in the present range of silane concentration in view of the fact that the complete dissociation of $Si(CH_3)_4$ and subsequent ionizations can lower the equilibrium temperature T_2 behind the n = 2^{nd} shock by as much as 200 ^{o}K (see Brown on tetraethyllead also).

3. A Solution to the Equations of Radiative Transfer in Optically Thick Plasmas

Now consider the situation of aiming an optical system at the hot gas in a local thermodynamic equilibrium. The gas is bounded by two parallel plane surfaces w cm apart and the line of sight of the optical system is perpendicular to the confining surfaces. Define the specific intensity of emission at a frequency, ν , as the energy emitted from the hot gas per unit time, unit surface area, unit solid angle, and per unit frequency, i.e.,

$$I_\nu \equiv \frac{dE}{dt\, d\sigma\, d\omega\, d\nu} \qquad (V.3)$$

The change of the specific intensity along the line of sight can be best expressed by

$$\frac{dI_\nu}{dy} = k'_\nu \left[B(\nu, T) - I_\nu \right] \qquad (V.4)^{49}$$

where y is the coordinate axis along the line of sight perpendicular to the surface and B(ν, T) the Planck's black body function. k_ν' is the absorption coefficient of the gaseous radiator, corrected for the stimulated emission:

$$k_\nu' = h\nu P(\nu) n_j B_{jj'} \left(1 - e^{-\frac{h\nu_{j'j}}{kT}}\right) \qquad (V.5)$$

j' and j label the upper and lower levels of the transition responsible for the emissions, respectively. P(ν) is the line profile function in the neighborhood of the central frequency, ν_0, and is normalized so that

$$\int_{-\infty}^{\infty} P(\nu)\, d\nu = 1 \qquad (V.6)$$

$B_{jj'}$ is the Einstein coefficient of absorption and is related to the other Einstein coefficients of emission ($A_{j'j}$) and of stimulated emission ($B_{j'j}$) by

$$g_{j'} A_{j'j} = \frac{2h\nu_{j'j}}{c^2} g_j B_{jj'} \qquad (V.7)$$

and

$$g_j B_{jj'} = g_{j'} B_{j'j} \quad , \qquad (V.8)$$

and also to the oscillator strength by

$$f_{jj'} = \frac{h\nu mc}{\pi e^2} B_{jj'} \quad , \qquad (V.9)$$

where

$$g_j f_{jj'} = g_{j'} f_{j'j} \equiv gf \qquad (V.10)$$

m and e are the mass and charge of the electron, respectively. The g's are the quantum weights of the respective energy levels. $f_{jj'}$ and $f_{j'j}$ are the absorption and emission oscillator strengths, respectively.

Eq. (V.4) is often called the equation of radiative transfer[49] whose solution is to give rise to the evaluation of the oscillator strengths via eqs. (V.5), (V.9), and the measurements of respective intensities. Note that in a complete thermodynamic equilibrium $\frac{dI_\nu}{dy} = 0$, i.e., the radiation field becomes nothing else but that of the black body.

Eq. (V.4) can be readily solved for I_ν by integrating with respect to y over the path between the two confining planes. We obtain

$$I_\nu = B(\nu, T)\left(1 - e^{-k_\nu' w}\right) \qquad (V.11)$$

A constant of intergration is neglected in the process because there is no external source of radiation along the line of sight. k_ν'w, the product of the corrected absorption coefficient and the width of the luminous region, is a measure of the optical thickness of the radiating gas; quite understandably the radiating gas of small k_ν'w is considered "optically thin" and that of large k_ν'w "optically thick".

The solution (V.11) states that the specific intensity from a radiator in a local thermodynamic equilibrium at temperature, T, cannot possibly be greater than or equal to that of the black body radiator at the same temperature. In other words, I_ν becomes equal to $B(\nu, T)$ only when $k_\nu' w$ goes to infinity, which is either the case of a complete thermodynamic equilibrium or the case of an infinitely deep, optically thin radiator in a local thermodynamic equilibrium.

It is customary and convenient to measure the integrated line intensity at a given frequency rather than the specific intensity. The integrated intensity can be written as

$$I = \int_{-\infty}^{\infty} I_\nu \, d\nu \cong B(\nu, T) \int_{-\infty}^{\infty} \left(1 - e^{-k_\nu' w}\right) d\nu \qquad \text{(V.12)}$$

$B(\nu, T)$ is a slowly varying function of ν and is assumed to remain constant in the neighborhood of the central frequency, ν_0. For an optically thin radiator one may Taylor-expand the exponential term in the integrand and retain only the first order term to arrive at

$$I = \frac{2\pi h e^2}{m} \frac{w}{\lambda^3} n_{j'} f_{j'j} \qquad \text{(V.13)}$$

It should be noted that

$$n_{j'} = \frac{g_{j'}}{g_j} n_j \, e^{-\frac{(E_{j'} - E_j)}{kT}} = n \frac{g_{j'} e^{-\frac{E_{j'}}{kT}}}{Z} \qquad \text{(V.14)}$$

where n is the number of emitting atoms (mercury).

The relation (V.13) has only a limited use because of difficulty in attaining a optically thin, yet very bright radiator. If such a condition is achieved, one can not only measure the absolute gf-values by measuring I absolutely, but also use eqs. (V.13) and (V.14) inversely to measure the temperature of the source by measuring relative intensities of several emission lines of one element present in the source, provided that their relative gf-values are known. The temperature in the latter case is calculated from eqs. (V.13) and (V.14):

$$T = \frac{(E_{j'n} - E_{j'm})}{k \ln\left[\frac{I_m}{I_n}\left(\frac{\lambda_m}{\lambda_n}\right)^3 \frac{(gf)_n}{(gf)_m}\right]} \qquad (V.15)$$

where the subscripts n, m, ····· label the various spectral lines observed. $(gf)_n$ and $(gf)_m$ are the relative gf-values of the n^{th} and m^{th} lines, respectively.

For an optically thick plasma the evaluation of the integrated line intensity of eq. (V.12) calls for the explicit form of k_ν 'w because the integration now has to be rigorously carried out—that is to say that an analytic expression of the line profile, $P(\nu)$, suitable to the present experimental circumstance is necessary. A brief review of all mechanisms of the spectral line broadening is in order, which can be classified into the following three categories:

i) Doppler broadening due to the thermal motion of emitting atoms has the profile of a Gaussian type

$$e^{-\left(\frac{\nu-\nu_0}{\Delta\nu_D}\right)^2} \tag{V.16}$$

where its 1/2 1/e-width, $\Delta\nu_D$, is given by

$$\Delta\nu_D = \frac{\nu_0}{c}\sqrt{\frac{2RT}{\sigma}} \tag{V.17}$$

ii) Generalized Lorentzian broadening due, at first, to the perturbation of the emitting atoms by neighboring atoms via collision, resulting in the interruption of emission, and secondly to the natural damping of atomic oscillators resulting from the radiation of electromagnetic energy. Both have the profile of one identical type

$$\frac{1}{1+\left(\frac{\nu-\nu_0}{\Delta\nu_L}\right)^2} \tag{V.18}$$

where the 1/2 half-width of the generalized Lorentzian profile, $\Delta\nu_L$, is

$$\Delta\nu_L = \Delta\nu_p + \Delta\nu_N \cong \frac{1}{2\pi t_{coll.}} \tag{V.19}$$

$\Delta\nu_p$ and $\Delta\nu_N$ are the 1/2 half-widths of the profiles pertaining to the collisional broadening (alternatively called the pressure broadening due to its dependence on the gas

pressure) and to the natural damping, respectively. $t_{coll.}$ is the time of collision between particles and under the experimental circumstance is considered much longer than the finite lifetime of a non-metastable excited state, thus giving rise to the approximation in eq. (V.19).

iii) Stark broadening due to the interaction of emitting atoms with neighboring charged particles such as ions, electrons, and polar molecules (the last contribution is very small compared with the ion or electron broadening). It breaks down to two basic classes—namely, the first order Stark broadening due to the presence of a permanent electric dipole in the atom and the second order Stark broadening due to the emergence of an electric dipole induced in the atom by an external electric field. The extent of the broadening therefore depends heavily on whether the electron orbits responsible for the emission of an individual line are of a penetrating kind or a non-penetrating kind. For a penetrating orbit the permanent electric dipole is extremely small because the time average of the electric dipole along the orbit has the contribution coming only from the portion of the orbit that stays outside the electron core around the nucleus, thus resulting in only the second order Stark broadening which is a small effect in itself.

The pertinent electric field in the case of ionized gases is not static but randomly directed and has contributions from the neighboring ions as well as from the electrons, which complicates the theoretical treatment together with the difficulty of evaluating the radial wave function of heavy

atoms. There is not a single successful theoretical Stark broadening profile for the complex atoms worth mentioning here at the moment.

Notice that the broadening of the first category is completely different in nature from that of the second category so that the two profiles can be either superimposed or separated freely, while those of the second and third categories are deeply interwoven under the experimental condition. The latter point indicates that if the Stark broadening is made not to dominate over the generalized Lorentzian broadening, one can very well approximate the combined profile by that of the second category with only a minor adjustment of the 1/2 half-width so as to fit the combined profile. A close examination of the electron configuration of the mercury atom shows that the quantum defects are large for all of the following terms:[50]

$6s^2\,^1S$	$7s\,^3S$	$7s\,^1S$	$8s\,^3S$	$9s\,^3S$
$6p\,^3P^o$	$6p\,^1P^o$			
$6d\,^1D$	$6d\,^3D$	$7d\,^1D$	$7d\,^3D$	$8d\,^1D$

i.e., all the pertinent electron orbits of these terms are deeply penetrating. Therefore the lines originating from these terms are subjected only to the second order Stark broadening. This together with the low electron density in the hot gas will indeed assure that the half-width of the Stark profile remains on the order of the Lorentzian

half-width.

Under these conditions $P(\nu)$ can be expressed as the convolution of two profiles (V.16) and (V.17), i.e.,

$$P(\nu) = \text{const.} \int_{-\infty}^{\infty} \frac{e^{-\left(\frac{\epsilon}{\Delta\nu_D}\right)^2}}{1+\left(\frac{\nu-\nu_0-\epsilon}{\Delta\nu_L'}\right)^2} d\epsilon$$

where ϵ is the frequency deviation from the central frequency in the Doppler broadening. $\Delta\nu_L'$ is the 1/2 half-width of the two profiles combined, excluding the Doppler width. The constant can be found via the normalization condition (V.6): Thus we obtain

$$\begin{aligned} P(\nu) &= P(a,b) \\ &= \frac{a}{\pi^{3/2}\Delta\nu_D} \int_{-\infty}^{\infty} \frac{e^{-\eta^2} d\eta}{a^2+(b-\eta)^2} \end{aligned} \tag{V.20}$$

where

$$a \equiv \frac{\Delta\nu_L'}{\Delta\nu_D}, \quad b \equiv \frac{\nu-\nu_0}{\Delta\nu_D}, \quad \eta \equiv \frac{\epsilon}{\Delta\nu_D} \tag{V.21}$$

Eq. (V.5) can be rewritten with eq. (V.9) as

$$k_\nu' w = \sqrt{\pi}\,\Delta\nu_D\, C\, P(a,b) \tag{V.22}$$

where

$$C = \frac{\sqrt{\pi}e^2}{mc} w \frac{n_j f_{jj'}}{\Delta\nu_D}\left(1 - e^{-\frac{h\nu}{kT}}\right) \qquad (V.23)$$

The integrated intensity of the emission line is obtained by substituting (V.21) for k_ν 'w in eq. (V.12):

$$\mathcal{J} \equiv \frac{I}{2\Delta\nu_D B(\nu_0, T)} = \int_0^\infty \left[1 - e^{-\sqrt{\pi}\Delta\nu_D C P(a,b)}\right] db \qquad (V.24)$$

The integration of (V.24) can not be carried out analytically in closed form. However, numerical values of $\mathcal{J}$ as a function of C and a had been evaluated by van der Held[69] and by Penner and Kavanaugh[70]; when plotted as functions of C, with as peramater, they are called curves of growth (Fig. 21).

For small C, $\mathcal{J}$ is linear in C, while $\mathcal{J}$ varies as $C^{\frac{1}{2}}$ for large C. The physically possible region is bounded by two limiting curves of $a = \infty$ and $a = 0$. Now that the relation between $\mathcal{J}$ and C is quantitatively established for any given a, one can evaluate the gf-value of a given line by experimentally determining both $\mathcal{J}$ and a together with the thermodynamic state of the radiating gas.

4. Measurement of Absolute Integrated Line Intensities

A two prism quartz spectrograph and a grating spectrograph coupled with a rotating drum camera, are alternately

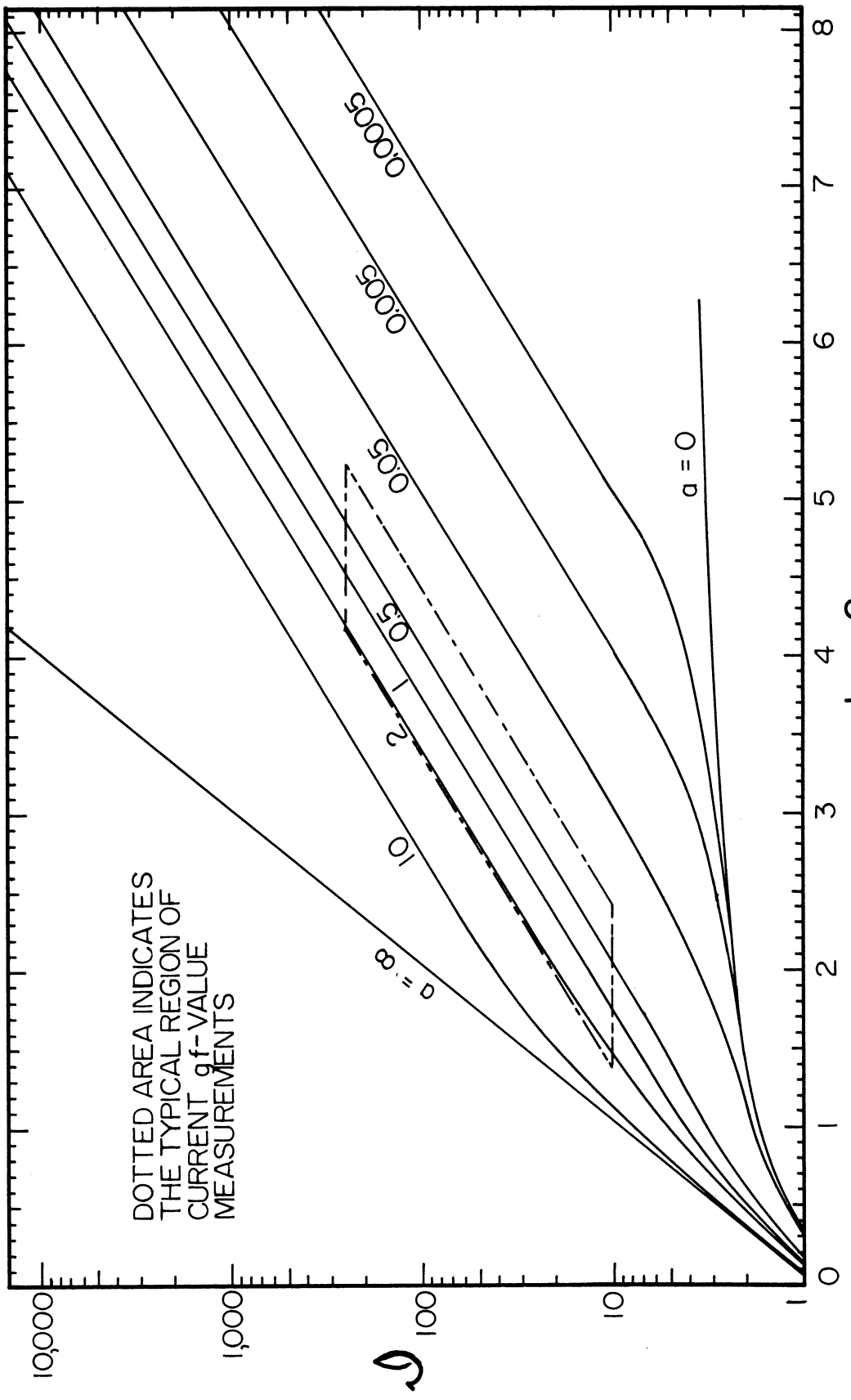

Figure 21. Curves of growth

used for the line intensity measurement. The first spectrograph is used for lines with wavelengths of 2400 Å to 4000 Å and the other for those above 4000 Å. The time-resolved line intensity is recorded on 35 mm film strip of Kodak 103-F (4500 Å ~ 6800 Å) or Kodak 103-0 (2400 Å ~ 5000 Å). A typical exposure time of the shock tube exposure is of the order of 8 to 20 μsec, while the time resolution of the recorded intensity is better than 1 μsec.

The spectrograph aims at an aperture (5 mm diameter, located 2.5 cm upstream from the endwall) provided in the mask covering the side window of the tube, by means of the following optical arrangement. Two collimating lenses (focal lengths 8" and 6") and a stop with a circular aperture between them are placed between the spectrograph and the test section. The stop is used in order to keep the solid angle of the shock tube radiation fixed. The image of the stop is focused at the center of the shock tube by the first collimating lens. The location of the second lens is adjusted in such a manner that the image of the entrance slit of the spectrograph is formed NOT on the stop but halfway between the stop and the first lens, in order to insure a uniform illumination on the entrance slit.

The integrated line intensity of a given spectral line can be measured in two different ways: One is to set the entrace slit width of the spectrograph in such a way that its effective width, $(s.w.)_{eff}$, on the image plane is slightly greater than the line width at its base, $\delta\lambda_{base}$.

The center of the resultant profile thus recorded on the film directly corresponds to the integrated line intensity. (The profile is obtained by tracing the exposed film with a microphotodensitometer.*) If $(s.w.)_{eff}$, is much larger than $\delta\lambda_{base}$, one observes a flat maximum, as wide as the quantity, $(s.w.)_{eff} - \delta\lambda_{base}$, at the center of the recorded profile. This can in turn be regarded as positive evidence that the integration of the specific intensity is duly performed. Another method, used when $(s.w.)_{eff} < \delta\lambda_{base}$ due to difficulties with over lapping neighboring lines and with severe line broadening, is to measure the area surrounded by the traced line profile and then to fit this area into a rectangular profile with its base width same as $(s.w.)_{eff}$. The height of the resultant rectangular column gives rise to the integrated intensity.

Following is a detailed description of the photographic photometry which has throughout been employed to determine the intensity absolutely.**

The densitometer tracing of an exposed film is a display of the relative transmission coefficient, θ_f, of its

---

* The recording microphotodensitometer was provided through courtesy of Professor C. E. Nordman of the Chemistry Department of the University.

** Photoelectric photometry can also be used, following the exactly same method as described for the film, simply by replacing the film with suitable photoelectric censors.

emulsion, regarding the unexposed area of the film as fully transparent. The film blackening is usually expressed in the unit of the neutral density which is defined as

$$\text{Neutral Density (N. D.)} \equiv \log \frac{1}{\theta_f}$$

The neutral density of the exposed film is generally a function of the exposure which can be expressed as

$$\text{Exposure (E)} = \text{Intensity (I)} \times \text{Exposure Time } (t_E). \tag{V.25}$$

It is then necessary to establish the exact dependence of N.D. on E in order to measure the intensity of radiation. For the evaluation of the absolute intensity the exposure scale must be fixed absolutely by means of an absolute radiation standard because θ_f alone provides only a relative exposure.

The absolute intensity measurement becomes rather complicated because i) the dependence of N.D. on E is not completely linear, ii) the film sensitivity is wavelength-dependent, and iii) the film is subjected to the reciprocity law failure. The reciprocity law failure is an effect which gives rise to a difference of the neutral density as a result of one exposure of I_1 and t_{E1} from that corresponding to the identical exposure but with ζI_1 and t_{E1}/ζ . ζ is a constant substantially different from unity. Therefore, in order to calibrate intensities of wide range, exposure times involved throughout the entire process of fim calibration

must be kept systematically close to one fixed value.

Actual plots of N.D. versus log E pertaining to any type of film show that there is a region where N.D. = const.log E, but as the exposure becomes very small or very large the "toe" or "shoulder" region develops each with a decreasing proportionality constant. The search for a suitable function of N.D. which becomes linear in log E for the entire range of the exposure resulted in the Seidel function defined as

$$S \equiv \log\left(10^{N.D.} - 1\right) = \log \frac{1-\theta_f}{\theta_f} \qquad (V.26)^{51}$$

Now that $S \propto \log E$, the calibration of the film for its spectral sensitivity can be done in the following manner:

i) Choose a spectrograph suitable for the spectral range of interest and set its entrance slit height at about 14 mm. The slit width can be set in such a way that $(s.w.)_{eff}$ is in the order of 10 $\overset{o}{A}$. Then place a step filter (a seven-step filter of rhodium evaporated on quartz; produced by Jarrell-Ash) right in front of the entrace slit. The relative coefficients of all seven steps must be calibrated beforehand because the density of each step is wavelength-dependent, especially in the ultraviolet region.

ii) Expose the film placed on the image plane by illuminating the entire entrace slit uniformly with a xenon flash lamp (or a spark gap in air). It is important that the

effective duration of the pulsed light source* is short in order to avoid the reciporcity law failure and in the present experiment it is set to be 30 μsec.

iii) Trace the exposed film along the length of the slit image by means of the densitometer. The film density corresponding to each step of the step filter is then numerically determined in terms of N.D. of ten reference neutral density filters** (Kodak Wratten Gelatin filter; N.D. varying from 0.1 to 1.0 in an increment of 0.1) by tracing the neutral density filters with the same densitometer. Calculate S for each of traced film densities (steps).

The use of the step filter is equivalent to having seven different light sources of known relative intensities, all with an identical exposure time. Denoting the flash lamp intensity at a given wavelength by I_L, the relative intensities seen by the film are $\theta_{S.F.} I_L$, where $\theta_{S.F.}$ stands for the relative transmission coefficients of the step filter. One may write

$$S = R(\lambda) \log E = R(\lambda) \log (a_{op} \theta_{S.F.} I_L t_E) \qquad (V.27)$$

a_{op} is a constant characteristic of the optical path. I_L and and t_E are constant also. The effective sensitivity of the

---

* Whether it is of a line radiation or continuum is immaterial as long as it has a wide, well distributed spectrum so that the sensitivity calibration at various wavelengths can be made.

** It is absolutely necessary to use only one set of neutral density filters consistently throughout the entire experiment.

film, $R(\lambda)$, can be found by plotting S versus log $\theta_{S.F.}$, i.e.,

$$R(\lambda) = \left.\frac{\Delta S}{\Delta \log \theta_{S.F.}}\right|_{\lambda} \qquad (V.28)$$

Since the exposure (E) found above by eq.'s (V.27) and (V.28) is in a relative scale and since the detail of a given optical path (shown symbolically as a_{op}) strongly influences the deviation of the resultant intensity seen by the film from the initial intensity of the radiator, the relative exposure scale and the entire optics involved must be calibrated by means of a known radiation standard. For this purpose the results of Euler[62] on the carbon arc have been used.

Euler observes that the radiant energy of the anode crater of a carbon arc stabilized just below the hissing point (with the current of about 11.5 amp) is that of a black body at 3995 ± 15 ^{o}K with its emissivity, ϵ_{ν}, varying with wavelength (ϵ_{ν} varies roughly from 0.69 to 0.76 over the wavelength range 2000 $\mathring{A}$ to 7000 $\mathring{A}$). By utilizing the same spectrograph and external optics in observing the radiation standard as used for shock tube exposures, we effectively cancel out all absorbing and scattering by the optics as well as difficulties with the solid angle into which the radiation is emitted. In order to make certain that $t_E^{arc} \approx t_E^{line}$, the rotating drum is used for the arc

exposure, the drum speed being nearly equal to that for shock tube exposures. A shutter is placed in the optical path to insure that no more than one revolution of the drum is used during the exposure.

Since the black body temperature is much lower than the shocked gas temperature, it is often necessary to increase the effective intensity of the arc in order to achieve a substantial blackening of the film. In view of the stringent restriction on the arc exposure time, this can be done by widening the entrance slit of the spectrograph because the arc is continuum radiation and $B(\nu, T_{arc})$ is rather a slowly varying function of ν .

The densitometer readings (traced along the λ-axis) of the film are converted to S values. We can write, using eq.'s (V.25) and (V.27),

$$S_\lambda^{arc} = R(\lambda) \log E_\lambda^{arc}$$

$$= R(\lambda) \log \left[a_{op} \Delta\nu^{arc} \epsilon_\nu B(\nu, T_{arc}) t_E^{arc} \right]$$

where $\Delta\nu^{arc}$ is the effective slit width in sec^{-1} on the image plane of the spectrograph. A comparison of the S value of the shock tube exposure at a given frequency with S_λ^{arc} completes the absolute calibration of the exposure scale:

$$\log \frac{E_\lambda^{line}}{E_\lambda^{arc}} = R(\lambda)^{-1} (S_\lambda^{line} - S_\lambda^{arc}) \quad ,$$

which gives rise, by virtue of definition (V.25),

$$I_\lambda^{line} = \int_{-\infty}^{\infty} I_\nu \, d\nu$$

$$= \left(\frac{E_\lambda^{line}}{E_\lambda^{arc}} \right) \frac{t_E^{arc}}{t_E^{line}} \Delta\nu^{arc} \epsilon_\nu B(\nu, T_{arc})$$

(V.29)

Each of t_E^{arc} and t_E^{line} can be found by dividing the height of the entrance slit image by the speed of the film mounted in the drum camera. Although we do not know absolute E_λ^{line} alone, since now the ratio $E_\lambda^{line}/E_\lambda^{line}$ obtained experimentally appears in eq. (V.29), we can find absolute I_λ^{line}.

In the region of wavelengths shorter than 2800 Å, the calibration of the exposure scale with the carbon arc encounters a difficulty in that $B(\nu, T_{arc})$ becomes so small* that the arc fails to produce an exposure necessary to yield a measurable film blackening (N.D. of 0.1 or greater) as long as one maintains to avoid the reciprocity law failure. This continues to be so even when $(s.w.)_{eff}$ is made as wide as 25 Å. In such a circumstance, an additional calibration of the film for its reciprocity law failure has proved to be very useful. Results show that the reciprocity law failure is wavelength- and intensity-dependent. Essential stages are the following: i) Expose a film strip with the carbon

---

* The value of $B(\bar{\nu}, T_{arc})$ drops from 5.045×10^4 at 5461-Å to 2.117×10^2 erg/cm^2-cm^{-1} -sec-sterad at 2500 Å.[53]

arc in the same manner as for the normal calibration but with an exposure time long enough to give rise to a significant blackening at each desired wavelength. ii) Use only one flash of the spark gap in air to expose another film strip (of the same kind as in step i)) through the seven-step filter, following the procedure used in measuring $R(\lambda)$. Repeat this with two, four, eight flashes and so forth, while keeping all other conditions identical. The net effect is that the exposure time is made to vary extensively, while the seven different intensities seen by the film remains unchanged. The range of the exposure time should cover the arc exposure time of step i). Then plot the traced N.D.'s corresponding to each fixed intensity as a function of exposure times and connect these points for each of the seven steps into a smooth curve.* iii) Locate among the family of curves obtained in stage ii) the measured N.D. corresponding to the integrated line intensity of the shock tube exposure at $t_E = t_E^{line}$. Then find from these calibration curves the new N.D. value which would have been the true N.D. value of the shock tube exposure, had it been that $t_E^{line} = t_E^{arc}$. Using $(S_\lambda^{line})_{corrected}$ thus evaluated, one can obtain I_λ^{line} via eq. (V.29).

The above method is quite laborious but helps to extend significantly the scope of photographic photometry in shock tube spectroscopy into a spectral range which had been completely left out in the past.

---

* One should notice that they are not straight lines but curves with diminishing slopes with increasing exposure times.

5. Measured Oscillator Strengths

Fig. 22 shows a typical shock tube run. A wave speed picture and the time-resolved spectrum together with densitometer tracings of four spectrum lines along the time axis are arranged in such a way that they all share one common time axis. This is a shock in a Ne-Hg-$Si(CH_3)_4$ mixture, their concentrations of which are indicated on the figure. As was said earlier, a small but quite definite amount of silane is necessary, to provide with its luminous line the essential measurement of the primary shock speed. Also shown are the numerical values specifying the equilibrium state of the shocked gas. It should be noticed that for each line the spectral intensity from the region behind the $n = 2^{nd}$ shock rapidly rises to a plateau without showing any sign of radiation overshoot, and this plateau is maintained until the $n = 3^{rd}$ shock is generated at the interface. This indicates that the local thermodynamic equilibrium is reached behind the $n = 2^{nd}$ shock and the role of impurities is negligible. Furthermore, the rise of the intensity to a plateau takes place simultaneously for all lines which originate from widely scattered levels above the first excited state ($6p^3P_o^o$), confirming the notion put forth earlier (Chapter IV) that the process of ionization and excitation takes place via the intermediate step of excitation to $6p^3P_o^o$.

This period of intensity plateau behind the $n = 2^{nd}$ shock is when the data toward gf-values are gathered. One evaluates J from the measured absolute intensity of a

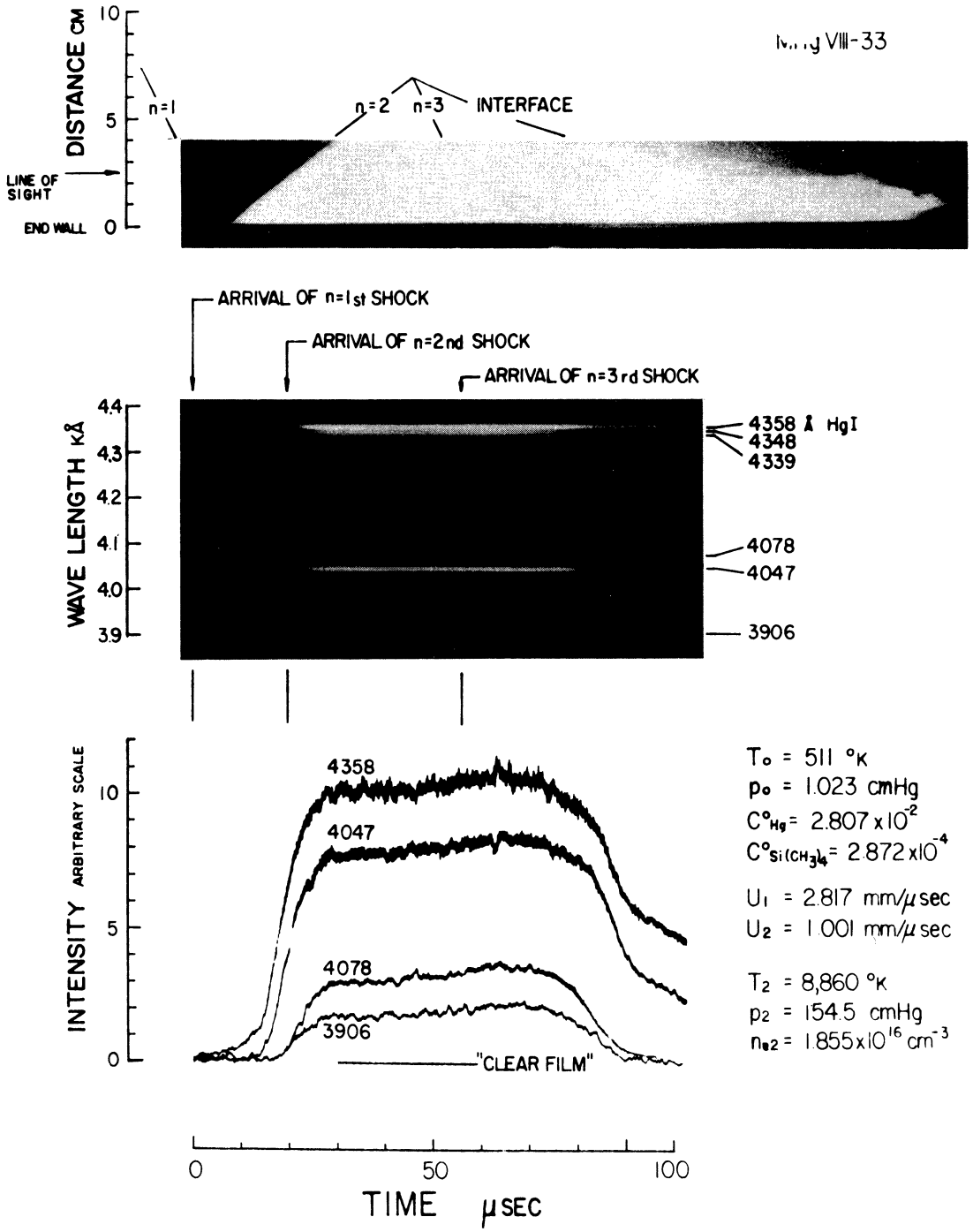

Figure 22. Wave speed picture and time-resolved spectrum (Series MHgVIII-33)

given line through eq. (V.24). $\mathcal{J}$ thus obtained turns out to be large for all neutral mercury lines dealt with in this investigation and ranges typically from 10 to 250 with only a few lines having $\mathcal{J} < 10$. Large values of $\mathcal{J}$ stem from the fact that the mercury concentration in neon is chosen rather large (more common concentrations of emitters in the bath of inert gas are in the region of 0.01 to 0.5%) in order to keep the uncertainty in measuring the partial pressure of mercury gas small.

In order to aid the evaluation of n_j appearing in eq. (V.23) (see eq. (V.14) also), the fractional population*

$g_j e^{-\frac{E_j}{kT}} / Z(p,T)$ has been calculated for seventeen different levels as a function of temperatures (the pressure dependence is so weak that in the temperature range of 7,000° to 17,000 °K one can not recognize it), and it is plotted in Fig. 23. The levels are indicated in terms of respective wave numbers measured from the ground state of neutral mercury.

In determining the optical depth α, it should be pointed out that $\Delta\nu_L'$ and $\Delta\nu_D$ (see eq. (II.17), (II.19), and (II.21)) both vary with wavelengths and with shock strengths. $\Delta\nu_D$ can be computed from eq. (V.17) with the aid of a shock calculation. Considering the fact that the emitting atoms (mercury) are much smaller in numbers than the foreign atoms

---

* It is at this stage that the cut-off in the divergent partition function ($Z_{Ei,z}$) mentioned earlier is important.

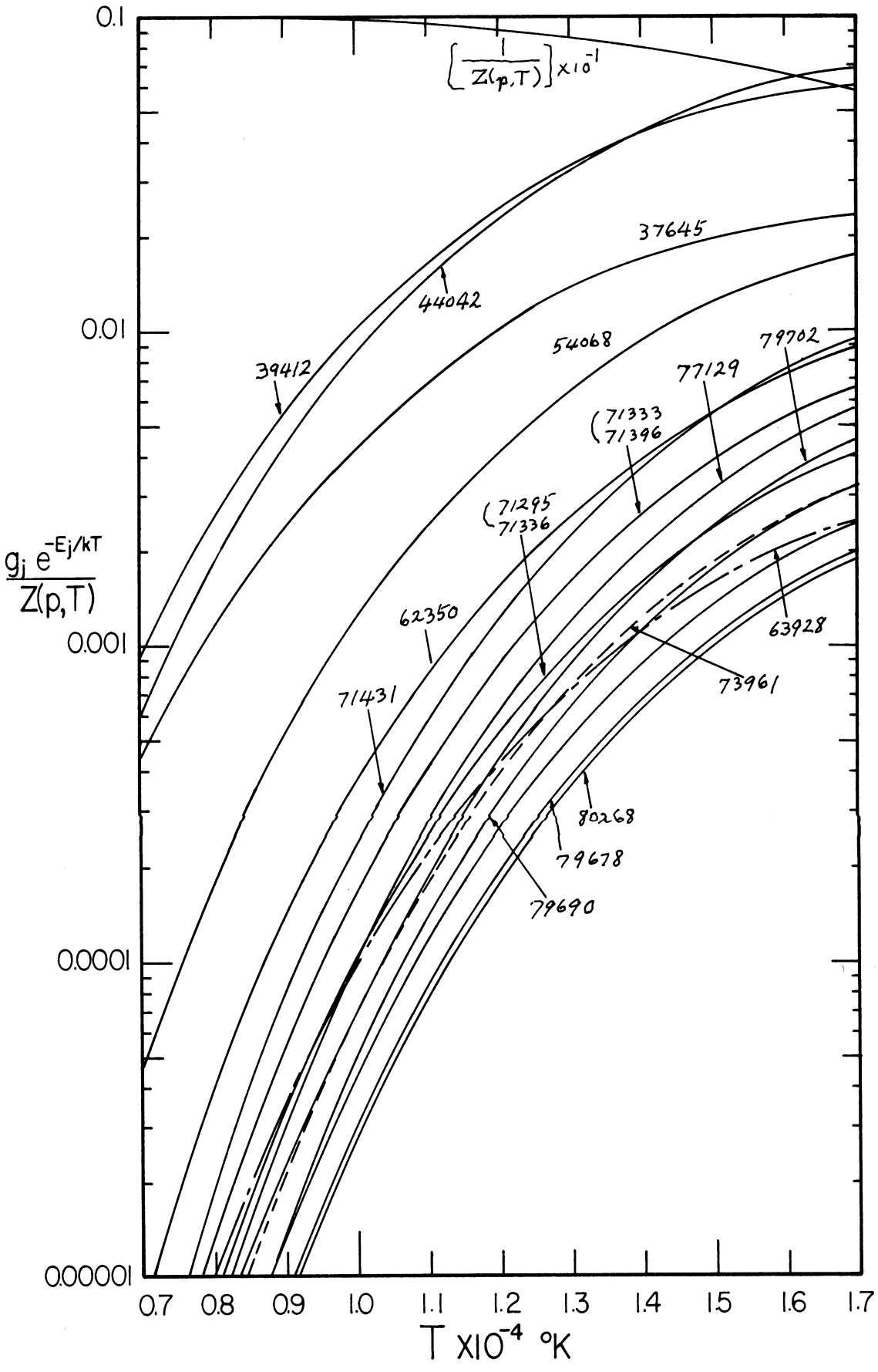

Figure 23. Fractional population of mercury atoms in excited levels as a function of temperature

(neon) surrounding them, one can write

$$\frac{1}{t_{coll.}} = n_p \bar{v}_r \pi \bar{r}_\lambda^2 \qquad (V.30)$$

where n_p, v_r, and $\bar{r}_\lambda^2$ are the number density of perturbers (neon), the average relative speed between emitters and perturbers, and the optical cross section (of the broadening collision) for a line with wavelength λ. $\bar{r}_\lambda^2$ is a constant for a given combination of emitters and perturbers and has to be measured. It is possible then to evaluate $\Delta\nu_L$ from eq. (V.18). On the other hand, a calculation of $\Delta\nu_L'$ is not simple because the adjusted optical cross section is no longer constant due to the contribution from the Stark broadening which depends on the charge density in the plasma. Instead, we will utilize the method of Hinnov and Hedwig Kohn in the flame spectroscopy.[54,55]

Hinnov[54] calculated the theoretical intensity density graph, which is a plot of log $\mathcal{J}$ versus the common logarithm of a quantity

$$ra = \frac{e^2 w}{mc} \frac{n_j f_{jj'}}{\Delta\nu_D}$$

with a as parameter. Just as was the case in the curves of growth, each curve in the intensity density graph has an asymptote of slope 1 for a very small concentration of emitters and another of slope 1/2 for a very large concentra-

tion. Hinnov shows that when these two asymptotes for a given α are extrapolated, the point of intersection furnishes the optical depth, i.e.,

$$\mathcal{J}_{\text{intersection}} = 2\alpha \qquad \text{(V.31)}$$

Noting that $r\alpha$ = const f (C^o), C^o being the concentration of the emitter for given temperature and emitting species. One can very well establish an experimental intensity-concentration graph by measuring $\mathcal{J}$ for widely varying C^o with an otherwise constant plasma condition. Hinnov and Kohn[55] proceed to demonstrate that such an experimental intensity-concentration graph can indeed be superimposed on the theoretical intensity-density graph precisely within experimental accuracy, and consequently this superposition furnishes the value of α by fixing the pair of asymptotes corresponding to the experimental conditions.

In applying this method to the shock tube spectroscopy, one must recognize the difficulty with keeping the temperature constant throughout while varying the mercury concentration. And because of the contribution to $\Delta\nu_L'$ from the Stark broadening, α is dependent on the mercury concentration. Thus the method of intensity-concentration graph appears impractical in the present situation.

A close examination of the theoretical intensity-density graph reveals that the greater the value of α, the more abrupt the transition from the low density asymptote to the high density asymptote becomes and that for $\alpha < 2$ the

asymptotic region (of high density) begins with $\mathcal{J}$ becoming 10 or greater. It is then possible to locate the high density asymptote with only one value of $\mathcal{J}$ that is greater than 10, provided that its position relative to the low density asymptote can be established, which in turn calls for the knowledge of $f_{jj'}$. At this moment we propose to use an iterative method, which yields satisfactory results within a few steps due to the fact that all cases considered lie in the asymptotic part of the curves of growth (see Fig. 21). The following steps of iteration can be used for this purpose: i) Guess $a^{(o)}$ for a given line, whose $\mathcal{J}$ is measured, and determine an $f_{jj'}^{(o)}$ from the curves of growth, ii) locate a point in the theoretical intensity-density graph with $\mathcal{J}_{\text{measured}}$ and $r^{(o)}\, a^{(o)}$ and draw a straight line of slope 1/2 through the point until it intersects the low density asymptote, iii) find therefore an improved $a^{(1)}$ via eq. (V.31) and iv) repeat steps i) to iii) with $a^{(1)}$ until $a^{(n)}$ falls within an acceptable range of $a^{(n-1)}$. The steps ii) and iii) are equivalent to manipulating the relation

$$\frac{\mathcal{J}_{\text{measured}}}{3.221\; r^{(n-1)} a^{(n-1)}} \longrightarrow a^{(n)} \qquad \text{(V.32)}$$

The optical cross sections of the combined profile, evaluated from the values of a thus found, show as expected, a dependence on the mercury concentration and temperature owing to the contribution from the Stark broadening. For

the resonance line of 2537 Å, the result of Kunze[57] on the optical cross section ($\bar{r}_\lambda^2 = 35.7$ Å^2 for mercury in neon) is used to evaluate a because the Stark broadening is expected to be extremely small for this line.

Table VI lists the measured lines of neutral mercury. Column 1 gives the wavelengths, columns 2 and 3 the low level designation and its term value in cm^{-1}, and columns 4 and 5 the same data for the higher level. A HgI term diagram with spectral transitions is shown in Fig. 24. In Table VII the measured gf-values of HgI lines are summarized together with results from earlier measurements by Ladenburg and Wolfsohn[56], Schouten and Smit[45], and Corliss and Bozman[46]. For lines which are difficult to separate, the combined gf-values are given as indicated with brackets.

The uncertainty in our measured gf-values (last column of Table VII) stems from uncertainties in i) measured shock speeds (the maximum error is 2%), ii) measured absolute line intensities (4% at most for all lines with $\lambda > 2800$ Å), and iii) estimated value of a (5%). The error in the absolute line intensity results in twice as large an error in the gf-value. For lines of $\lambda < 2800$ Å, there is an additional uncertainty of about 4% in the final gf-values arrising from the calibration of reciprocity law failure (see Section 4).

It should be said that earlier results by Schouten and Smit and by Corliss and Bozman were obtained by measuring at first the relative gf-values of emission lines from the copper-elctrode arcs and readjusting them to the known

Table VI

Measured Spectral Lines of HgI

λ air Å	Classification			
	low (j)	$E_j(cm^{-1})$	high (j')	$E_{j'}(cm^{-1})$
5790.66	$6p\,^1P_1^o$	54068.78	$6d\,^1D_2$	71333.18
5789.66	$6p\,^1P_1^o$	54068.78	$6d\,^3D_1$	71336.16
5769.60	$6p\,^1P_1^o$	54068.78	$6d\,^3D_2$	71396.22
5460.73	$6p\,^3P_2^o$	44042.98	$7s\,^3S_1$	62350.46
4358.33	$6p\,^3P_1^o$	39412.30	$7s\,^3S_1$	62350.46
4347.50	$6p\,^1P^o$	54068.78	$7d\,^1D_2$	77064.10
4339.22	$6p\,^1P_1^o$	54068.78	$7d\,^3D_2$	77107.92
4077.83	$6p\,^3P_1^o$	39412.30	$7s\,^1S_o$	63928.24
4046.57	$6p\,^3P_o^o$	37645.08	$7s\,^3S_1$	62350.46
3906.37	$6p\,^1P_1^o$	54068.78	$8d\,^1D_2$	79660.79
3903.64	$6p\,^1P_1^o$	54068.78	$8d\,^3D_1$	79678.71
3901.87	$6p\,^1P_1^o$	54068.78	$8d\,^3D_2$	79690.30
3663.28	$6p\,^3P_2^o$	44042.98	$6d\,^1D_2$	71333.18
3662.88	$6p\,^3P_2^o$	44042.98	$6d\,^3D_1$	71336.16
3654.84	$6p\,^3P_2^o$	44042.98	$6d\,^3D_2$	71396.22
3650.15	$6p\,^3P_2^o$	44042.98	$6d\,^3D_3$	71431.31
3341.48	$6p\,^3P_2^o$	44042.98	$8s\,^3S_1$	73961.30
3131.84	$6p\,^3P_1^o$	39412.30	$6d\,^1D_2$	71333.18
3131.55	$6p\,^3P_1^o$	39412.30	$6d\,^3D_1$	71336.16
3125.67	$6p\,^3P_1^o$	39412.30	$6d\,^3D_2$	71396.22

Table VI: continued

λ air Å	Classification			
	low (j)	$E_j(cm^{-1})$	high (j')	$E_{j'}(cm^{-1})$
3027.49	$6p^3P^o_2$	44042.98	$7d^1D_2$	77064.10
3025.61	$6p^3P^o_2$	44042.98	$7d^3D_1$	77084.63
3023.48	$6p^3P^o_2$	44042.98	$7d^3D_2$	77107.92
3021.50	$6p^3P^o_2$	44042.98	$7d^3D_3$	77129.54
2967.54	$6p^3P_o$	37645.08	$6d^1D_2$	71333.18
2967.28	$6p^3P_o$	37645.08	$6d^3D_1$	71336.16
2925.41	$6p^3P^o_2$	44042.98	$9s^3S_1$	78216.26
2893.60	$6p^3P^o_1$	39412.30	$8s^3S_1$	73961.30
2806.77	$6p^3P^o_2$	44042.98	$8d^1D_2$	79660.79
2805.35	$6p^3P^o_2$	44042.98	$8d^3D_1$	79678.71
2804.44	$6p^3P^o_2$	44042.98	$8d^3D_2$	79690.30
2803.47	$6p^3P^o_2$	44042.98	$8d^3D_3$	79702.63
2752.78	$6p^3P^o_o$	37645.08	$8s^3S_1$	73961.30
2655.13	$6p^3P^o_1$	39412.30	$7d^1D_2$	77064.10
2653.68	$6p^3P^o_1$	39412.30	$7d^3D_1$	77084.63
2652.04	$6p^3P^o_1$	39412.30	$7d^3D_2$	77107.92
2536.52	$6s^{21}S_o$	0	$6p^3P^o_1$	39412.30

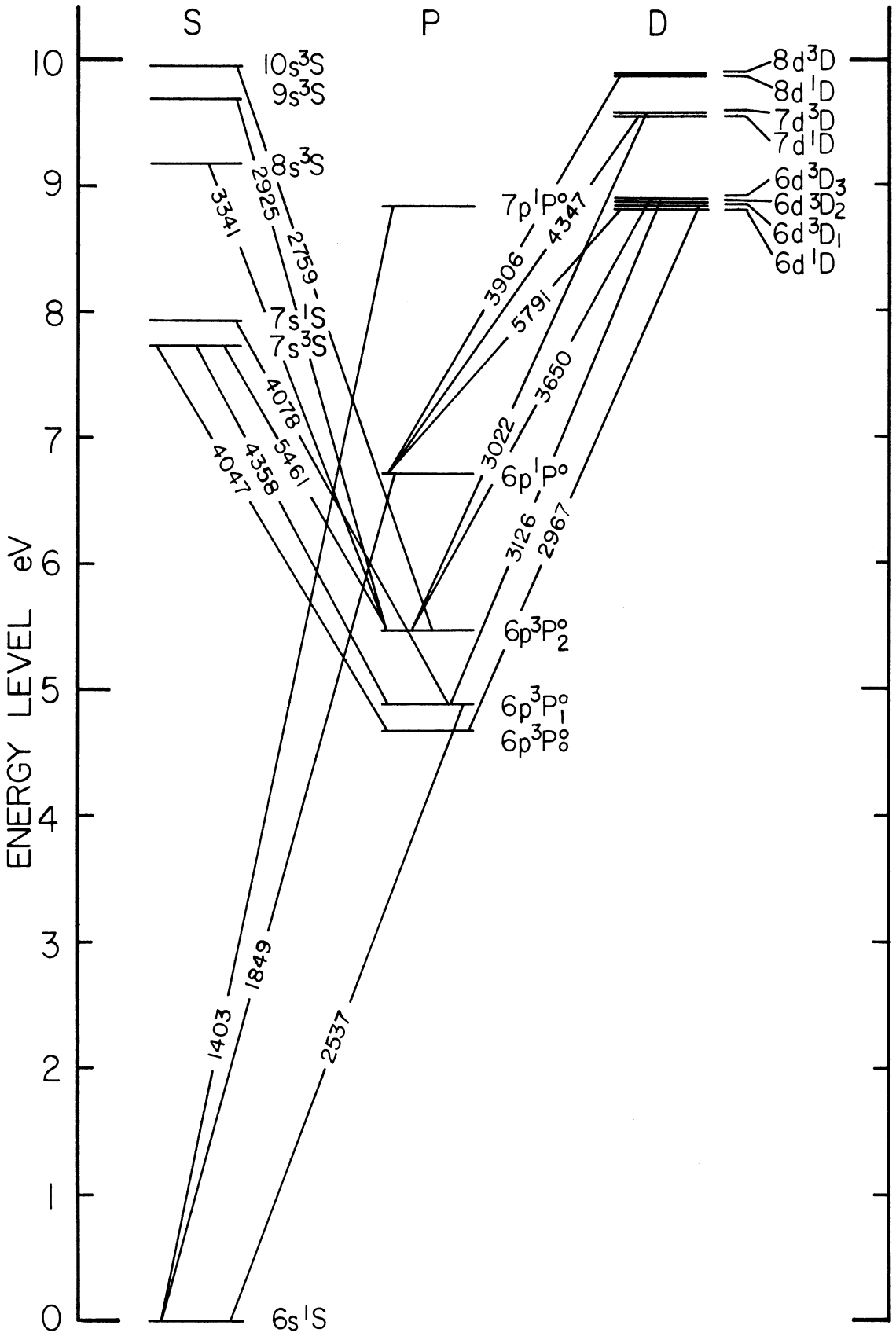

Figure 24. HgI term diagram

Table VII

Measured Absolute gf-Values of HgI

λ air Å	Ladenburg and Wolfsohn	Schouten and Smit	Corliss and Bozman	Present Work
5790.66		3.217	4.539	9.4 ± 1.4
5789.66				
5769.60		3.544	3.827	10.0 ± 1.5
5460.73		4.918	33.82	2.83 ± 0.44
4358.33		2.335	21.36	2.72 ± 0.41
4347.50				0.47 ± 0.07
4339.22				0.19 ± 0.03
4077.83		0.084	0.570	0.021 ± 0.003
4046.57		0.761	7.832	1.69 ± 0.25
3906.37				0.10 ± 0.01
3903.64				
3901.87				
3663.28		0.805	1.1	0.36 ± 0.05
3662.88			0.37	
3654.84			1.4	0.61 ± 0.09
3650.15		7.830	13	5.66 ± 0.85
3341.48			0.22	0.08 ± 0.01
3131.84		0.038	0.819	1.97 ± 0.29
3131.55			0.819	
3125.67			0.979	

Table VII: continued

λ air Å	Ladenburg and Wolfsohn	Schouten and Smit	Corliss and Bozman	Present Work
3027.49				1.67 ± 0.25
3025.61				
3023.48				
3021.50			0.481	
2967.54		0.238		0.23 ± 0.03
2967.28			2.58	
2925.41				0.037 ± 0.006
2893.60			0.205	0.046 ± 0.007
2806.77				2.60 ± 0.39
2805.35				
2804.44				
2803.47				
2752.78			0.107	0.041 ± 0.008
2655.13				6.90 ± 1.3
2653.68				
2652.04				
2536.52	0.0255	0.027	0.303	0.021 ± 0.005

absolute gf-value of one line (e.g., 2537 Å), while in the present investigation an absolute gf-value has been measured individually for each line. The result on the resonance line (2537 Å) by Ladenburg and Wolfsohn is considered very accurate and was obtained by means of the "hook method" (an absorption method involving the anomalous dispersion in the neighborhood of a resonance line). It also compares fairly well with a theoretical value of $gf_{2537} = 0.028$ by Garstang[58]. In view of the quite involved process of the present measurement on this resonance line, the present result appears most satisfactory. Present results on other lines differ considerably from those earlier ones and this discrepancy is mainly due to the lack of local thermodynamic equilibrium on the part of arc measurements and the inhomogeneity in the temperature and density across the arc.

In performing the measurements on the resonance line (2537 Å), a special care was needed in order to prevent the line reversal and to depress the continuum radiation. The most satisfying run was obtained by making the shock as weak as possible without violating the requirements necessary to achieve local thermodynamic equilibrium behind the $n = 2^{nd}$ shock and by using the smallest mercury concentration that can be tolerated within the frame work of photographic photometry.

CHAPTER VI

SUMMARY AND CONSIDERATION OF RELATED FUTURE RESEARCHES

In this present dissertation, an extensive investigation of various problems in the heated shock tube, starting from its construction, has been presented. It largely consists of numerical calculations on shocked mercury (and neon-mercury mixtures) over a very wide range of shock strengths, experiments on the overall performance of the heated shock tube as a new fluid dynamical device, a study of the approach toward the ionization equilibrium in shocked mercury, and finally the measurements of absolute oscillator strengths of neutral mercury lines.

In presenting the shock theory in Chapter II, it has been pointed out that usual three laws of conservation hold true not only across a primary shock but also across each of all reflected shocks. Subsequently a set of very general shock relations has been derived for an n^{th} shock only with an additional assertion that the n^{th} shock speed and thermodynamic state ahead of the shock are known, without making any assumption on the mechanism of reflected shock generation. This modification was motivated by the persistent failure of the usual reflected shock theory in predicting the reflected ($n = 2$) shock speed from a known primary shock speed, which results in a noticeable disagreement between T_2 (calculated) and T_2 (measured), and it indeed showed a substantial improvement in providing the equilibrium tempera-

ture T_2 when applied to the previous line reversal data by Charatis.[16]

The shock relations coupled with the ionization equilibrium relations written out from the general law of mass action have been numerically evaluated for primary shocks in mercury and mercury-neon mixtures, and respective Rankine-Hugoniot curves have been obtained. Their value remains mostly academic at the moment because of the limitation of attainable shock strengths on the part of the laboratory practice, but never the less the influence of first two successive ionizations upon the density ratio (ρ_1/ρ_o) is shown very clearly. Due to an overlap in two degrees of successive ionizations, a complete return of ρ_1/ρ_o to an ideal (purely translational) value was absent.

It would be of great interest if at least the first maximum in ρ_1/ρ_o can be experimentally observed. This appears extremely difficult for gases such as mercury and xenon even with an aid of explosives as driving gas because of severe boundary layer growth, ever increasing in degree with increasing shock strengths as long as the ionization is "active". However, in the cesium gas the possibility of such an investigation seems rather favorable because the first ionization potential is so small that a nearly complete first ionization can be achieved in the shock tube without any complication arising from the second ionization.

The equation of state in ionized mercury has also been evaluated for temperatures from 5,000° to 30,000 °K and pressures from 50 to 5,000 cm Hg, together with the

electronic partition function, the effective electronic degrees of freedom and the degrees of ionization, all irrespective of shock relations.

The novel observation of the reflected (n = 2) shock bifurcation in the monatomic gas of mercury has been described in detail in Chapter III, together with the shock tube performance. It has been fully demonstrated, with experiments and through a proposal of a "γ-model" of shock bifurcation, that an "active" ionization behind the primary shock is responsible for a fast growth of boundary layer in mercury, which in turn causes the bifurcation. An additional check of the γ-model was made in xenon also. By virtue of the γ-model, a special attention is called again to the cesium gas as a prospective shock medium because the cesium gas behaves very much like an ideal gas between the first and second stages of ionization, as shown with a theoretical calculation of γ.

One may point out that the fact that γ can become smaller than 5/3 is physically equivalent to the fact that the density ratio (ρ_1 / ρ_0) exceeds the ideal limit, both arising from "active" ionizations. However, it has not been determined whether the indication which the density ratio $\rho_1 / \rho_0 > 4$ may have on the question of shock difurcation is consistent with the fact that for γ_1 less than approximately 1.5 the reflected shock bifurcation is most likely to take place either in monatomic gases or in polyatomic gases, and this remains to be seen through a reinterpretation of the

previous experiments on bifurcation in polyatomic gases.

It has been pointed out that the boundary layer profile in the primary flow can be obtained by a detailed study of the change in bifurcated shock profile as a function of time.

It can be concluded that the flow (equilibrium zone) behind the shocks of n = 1 and 2 are not suitable for the quantitative spectroscopic source if the reflected (n = 2) shock is bifurcated, as was the case for all shocks in mercury (strong enough to have the luminosity in the equilibrium region). For all spectroscopic measurements it has been made certain that the bifurcation is absent by reducing the mercury concentration in neon and the equilibrium temperature behind the primary shock.

The usual failure of the ideal shock tube theory in predicting the shock strength at the end of the tube has been found also present in the heated shock tube and this again upgrades the adequacy of the shock theory developed in Chapter II even further.

The measurement of ionizational relaxation times in shocked mercury has shown that the measured activation energy of ionization coincides with the resonance energy of neutral mercury in the temperature regime of $7,300^{\circ}$ to $11,000\ ^{\circ}K$, indicating that each process of ionization (the atom-atom process and the electron-atom process) consists of two steps. For electron densities of 2.80×10^{16} to $4.20 \times 10^{17}\ cm^{-3}$ the relaxation time is found to be independent of pressure, and this tendency is identified as a characteristic of the

electron-atom process through reinterpreting the previous results on argon, krypton, xenon, and cesium, and comparing them with the present result. This, together with an apparent lack of any additional period attributable to the atom-atom process, has led us to the conclusion that the approach toward the ionization equilibrium in shocked mercury takes place mainly through the electron-atom process. Additional measurements with shocks in mercury-neon mixtures confirmed this conclusion. Consequently, in this electron density regime the most favorable mechanism of providing the electrons necessary in initiating the electron-atom process appears to be that of photo-excitation and -ionization.

Such a claim on the role of photo-processes may seem difficult to be tested directly in the shock tube without a sufficient information on the cross sections of photo-excitation and -ionization. An experiment with shocks in a medium containing some free electrons ahead of the arrival of shock may give rise to a better understanding of the way initial electrons are made available and it can be done, for instance, by spraying a very small amount of radioactive material.[60] Also it is suggested here that an independent experiment on the photo-excitation and -ionization be done by means of an atomic beam through a continuum radiation field. Such an investigation will be particularly interesting in view of the fact that the cross sections of photo-excitation and -ionization can be estimated from the absolute gf-values.[59]

The notion of the two-step process can be further examined by accurately studying the time-resolved profile of

the resonance lines (2537 Å in the case of neutral mercury) in comparison with the profiles of other lines originating from higher levels. For lines of widely scattered higher levels, such a comparison has been made and it has shown a distinctive behavior of indiscriminatory excitation among such levels, again favoring the two-step process.

The heated shock tube has been seen to be particularly suitable for the investigation of the approach toward equilibrium in view of the fact that the impurity concentration can be reduced by thorough baking and pumping to such a level that its influence upon the excitation process becomes negligible. Indeed, the radiation overshoot has been absent in all cases of mercury and mercury-neon mixtures, unless an additive such as tetramethylsilane is added in the shocked zone to a level which amounts to approximately 10% of the mercury concentration. It is reasoned that in cases with the radiation overshoot present the electrons contributed by impurity atoms during the period of relaxation are responsible for the temporary overpopulations in the excited states of neutral mercury. It is also thought probable that the atomic species in excited states arising from dissociating tetramethylsilane play a similar role to that of impurity-originated electrons. In this respect an investigation of the phenomenon of ionizational relaxation with shocks in a medium that consists of the gas of the main interests and one (or two) other monatomic gas (monatomic for the sake of simplicity), which has highly populated levels that match well with the first excited states in the main gas, appears quite profit-

able—that is, the presence and absence of such a gas may result in different relaxation times.

The absolute gf-values of 37 neutral mercury lines have been determined through measurements with shocks in Ne-Hg-$Si(CH_3)_4$ mixtures, using the method of curves of growth. Usual photographic photometry was used for absolute intensity measurements for lines with $\lambda > 2800$ Å. For lines with $\lambda < 2800$ Å a modified photographic photometry has been devised, which involves an additional calibration of the film for its reciprocity law failure. Results on gf-values (Table VII) have uncertainties varying from 15 to 20%. In view of the fact that the mercury concentration is rather large and in turn the line intensities are high, the optical depth of the shocked gas had to be determined unambiguously, and the method of Hinnov and Kohn has been employed for this purpose.

Using a semi-empirical method of Kobzev and Norman,[59] the photo-excitation cross sections for the series $6p^3P_2^o$ — n^3S_1 can be estimated from measured gf-values as follows: $\sigma_j(\nu_{jj'}) = 2.7 \times 10^{-17}$ cm^2 for $\lambda = 5461$ Å (n = 7), 9.7×10^{-19} for 3341 Å (n = 8), and 1.9×10^{-19} for 2925 Å (n = 9). By extrapolating these values of $\sigma_j(\nu_{jj'})$ to the series limit, one finds the photoionization cross section for $6p^3P_2^o$ —I.P. to be 1.0×10^{-19} cm^2. This result can be compared with direct experimental measurement of the photo-ionization cross section.

It has been demonstrated through discussions in Chapters IV and V that the heated shocks tube can be used adequately for quantitative spectroscopic measurements on metallic elements which either are evaporable at the shock tube temperature (up to 400 ^{o}C) or can be made available in the gaseous phase by virtue of metallo-organic compounds that are not necessarily volatile at room temperature. More experiments with the heated shock tube on atomic constants of heavy elements, which are useful for laboratory plasma diagnosis as well as for an astrophysical application, are highly recommended.

APPENDIX A

LOWERING OF IONIZATION POTENTIALS

According to Fermi[61] an atom in a gas of a given pressure is allowed to have only a limited volume, thus making the number of physically allowed electron orbits finite. This makes it possible to have a finite value of the electronic partition function.

Experimentally it is seen that the series limits of hydrogen-like spectra are depressed, the spectrum remaining normal up to a certain quantum number, after which the lines merge into a continuum even before the series limit when the pressure and the charge density are decreased.[62] Inglis and Teller[63] took the Stark broadening as the most important mechanism of level spreading and found the cut-off quantum number by equating the energy difference between two neighboring levels to the spreading of corresponding energy level. In view of the fact that the Stark broadening is a longer range interaction than direct collisions, the Inglis-Teller cut-off is much deeper than the Fermi cut-off.

Taking the screening of a charge in the plasma by neighboring charged particles into account, the lowering of ionization potential of eq. (II.30) known as the Debye-Hückel formula is obtained.[64,65] This cut-off lies in between the criteria of Fermi and Inglis-Teller as expected. The Debye-Hückel cut-off is valid only when the number of electrons per Debye sphere is less than one. For higher density plasma

one may use the result by Ecker and Kröll.[66] There is now a rather widely accepted notion that the partition function cut-off is not exactly identical to the lowering of ionization potential.[67]

The effect of the partition function cut-off on the equations of ionization equilibrium is very small due to the fact that only the ratio of two partition functions of an atom and its ion (or the first and second ions and so forth) appears in the equations.* The change in the degrees of ionization as one changes from the use of a Fermi cut-off to an Inglis-Teller cut-off is less than a percent while the partition functions of the two cut-offs differ from each other often by more than 20% at a modernately high temperature. Consequently, its influence of the cut-off upon the shock calculation is small. But it becomes important when one tries to calculate the upper level populations which are necessary for quantitative spectroscopy, because there one is no longer dealing with the ratio of partition functions but with an absolute value of an individual partition function.

---

* We have made extensive numerical tests to see the effect of different cut-offs for both helium and lithium with conveniently rearranged energy levels for the sake of clarity.

APPENDIX B

DERIVATION OF γ FOR IONIZED MONATOMIC GASES

Let us at first consider a simple case of a monatomic gas, A, with only one internal level that coincides with its ionization potential. One can write from eq. (V.7)

$$e = \frac{p}{\rho} + \frac{\alpha_1}{m_A} \chi_I \tag{B.1}$$

where the equation of state is

$$\frac{p}{\rho} = (1+\alpha_1) \frac{kT}{m_A} \tag{B.2}$$

The specific heat at a constant volume is then written as

$$C_v = \frac{\partial e}{\partial T}$$

$$= \frac{3}{2}(1+\alpha_1)\frac{k}{m_A} + \left(\frac{3}{2}\frac{k}{m_A}T + \frac{\chi_I}{m_A}\right)\frac{\partial \alpha_1}{\partial T} \tag{B.3}$$

From eq. (V.34) one obtains

$$\frac{\alpha_1^2}{1-\alpha_1^2} = \text{const.} \frac{T^{5/2}}{p} e^{-\frac{\chi_I}{kT}}$$

by putting $Z_{EII}/Z_{EI} = 1$. Differentiating eq. (B.4) with respect to T and rearranging it, one arrives at

$$\frac{\partial \alpha_1}{\partial T} = \frac{1}{2}\alpha_1(1-\alpha_1^2)\left(\frac{5}{2}+\frac{\chi_I}{kT}\right)\frac{1}{T} \qquad (B.5)$$

On the other hand, the specific enthalpy of this system is from eq. (V.4)

$$h = \frac{5}{2}\frac{p}{\rho} + \frac{\alpha_1}{m_A}\chi_I \qquad (B.6)$$

which gives rise to the specific heat at a constant pressure

$$C_p = \frac{\partial h}{\partial T}$$

$$= \frac{5}{2}(1+\alpha_1)\frac{k}{m_A} + \left(\frac{5}{2}\frac{k}{m_A}T + \frac{\chi_I}{m_A}\right)\frac{\partial \alpha_1}{\partial T} \qquad (B.7)$$

The specific heat ratio, γ , is then found from eq.'s (B.3), (B.7), and (B.5) to be

$$\gamma \equiv \frac{C_p}{C_V} = \frac{5+\alpha_1(1-\alpha_1)\left(\frac{5}{2}+\frac{\chi_I}{kT}\right)^2}{3+\alpha_1(1-\alpha_1)\left(\frac{3}{2}+\frac{\chi_I}{kT}\right)\left(\frac{5}{2}+\frac{\chi_I}{kT}\right)} \qquad (B.8)$$

Eq. (B.8) amounts to a chemical approximation of the specific heat ratio.[39]

Now we consider a more detail expression of γ for a real monatomic gas, A, with two stages of ionizations taken into account. Internal electronic levels are also excitable. From eq. (II.7) we get

$$e = (1+\alpha_1+\alpha_1\alpha_2)\frac{kT}{m_A}\left[\frac{3}{2}+(1-\alpha_1)f_{EI}+\alpha_1(1-\alpha_2)f_{EII}\right.$$
$$\left.+\alpha_1\alpha_2 f_{EIII}\right]+\frac{\alpha_1}{m_A}\chi_I+\frac{\alpha_1\alpha_2}{m_A}\chi_{II} \qquad (B.9)$$

In differentiating eq. (B.9) with respect to T to find C , one encounters the derivatives $\frac{\partial\alpha_1}{\partial T}$, $\frac{\partial\alpha_2}{\partial T}$, $\frac{\partial f_{EI}}{\partial T}$, $\frac{\partial f_{EII}}{\partial T}$, and $\frac{\partial f_{EIII}}{\partial T}$.

From eq. (II. 34) one obtains

$$\frac{\partial\alpha_1}{\partial T} \cong \frac{1}{2}\alpha_1(1-\alpha_1^2)\left(\frac{5}{2}+\frac{\chi_I}{kT}+\frac{f_{EII}}{2}+\frac{f_{EI}}{2}\right)\frac{1}{T} , \qquad (B.10)$$

where it is assumed that $\alpha_2 = 0$, and

$$\frac{\partial}{\partial T}\left(\frac{Z_{EII}}{Z_{EI}}\right) = \frac{1}{2T}\left(f_{EII}-f_{EI}\right)\frac{Z_{EII}}{Z_{EI}} \qquad (B.11)$$

Similarly, from eq. (II.35) one finds

$$\frac{\partial \alpha_2}{\partial T} \cong \frac{\alpha_2(2+\alpha_2)(1-\alpha_2^2)}{2(1+2\alpha_2)} \left(\frac{5}{2} + \frac{\chi_{II}}{kT} + \frac{1}{2} f_{EII} - \frac{1}{2} f_{EIII} \right) \frac{1}{T} \tag{B.12}$$

where it is asserted that $\alpha_1 = 1$.

Recalling the definition of f_{Ez}, z = I, II, III --- (see eq. (II.9)), it can be shown that

$$\frac{\partial f_{Ez}}{\partial T} = \frac{f_{Ez}}{T} + 2T \frac{\partial^2}{\partial T^2} \left[\ln \left(\sum_j^{n^*} g_j e^{-\frac{E_j}{kT}} \right) \right] \tag{B.13}$$

where n^* stands for the cut-off quantum number. The second term on the right hand side of eq. (B. 13) becomes

$$\begin{aligned} & -\frac{f_{Ez}}{T^2} - \frac{2 f_{Ez}}{T^2} + \frac{1}{T^2} \left\langle \left(\frac{2E}{kT} \right)^2 \right\rangle \\ & \cong -\frac{2}{T^2} f_{Ez} \quad , \end{aligned} \tag{B.14}$$

where it is assumed that

$$\left| f_{Ez}^2 - \left\langle \left(\frac{2E}{kT} \right)^2 \right\rangle \right| \ll f_{Ez} \tag{B.15}$$

[68]

Therefore one can write, with eq.'s (B.10) through (B.14),

$$
\begin{aligned}
C_V \cong\ & \frac{3}{2}\left(1+\alpha_1+\alpha_1\alpha_2\right)\frac{k}{m_A} \\
& + \frac{1}{2}\alpha_1\left(1-\alpha_1^2\right)\frac{k}{m_A}\left(\frac{5}{2}+\frac{\chi_I}{kT}+\frac{f_{EII}}{2}-\frac{f_{EI}}{2}\right)\Big[\frac{3}{2}\left(1+\alpha_2\right) \\
& - \left(2\alpha_1-\alpha_2+2\alpha_1\alpha_2\right)f_{EI}+\left(1+2\alpha_1\right)\left(1-\alpha_2\right)f_{EII} \\
& + \left(\alpha_2+2\alpha_1\alpha_2+2\alpha_1\alpha_2^2\right)f_{EIII}+\frac{\chi_I}{kT}+\frac{\chi_{II}}{kT}\alpha_2\Big] \\
& + \frac{1}{2}\alpha_1\alpha_2\frac{\left(2+\alpha_2\right)\left(1-\alpha_2^2\right)}{1+2\alpha_2}\left(\frac{5}{2}+\frac{\chi_{II}}{kT}+\frac{f_{EIII}}{2}-\frac{f_{EII}}{2}\right)\Big[\frac{3}{2} \\
& + \left(1-\alpha_1\right)f_{EI}-\left(1+2\alpha_1\alpha_2\right)f_{EII} \\
& + \left(1+\alpha_1+\alpha_1\alpha_2\right)f_{EIII}+\frac{\chi_{II}}{kT}\Big]
\end{aligned}
\tag{B.16}
$$

C_p can be found in a similar manner and it gives rise to eq. (III.4) with eq. (B.16). Eq. (III.4) can be reduced to eq. (B.8) by asserting that $\alpha_2 = 0$ and $f_{Ez} = 0$. γ thus found is a strong function of α_1 and α_2, which in turn depends on T and p. The contribution coming from f_{Ez} is rather small.

REFERENCES

1. Vielle, P., Comptes Rendus 129, (1899).

2. Geiger, F. W. and Mautz, C. W., "The Shock Tube as an Instrument for the Investigation of Transonic and Supersonic Flow Patterns", University of Michigan Engineering Research Institute and U. S. Navy Department Office of Naval Research Report, Contract No. N6-ONR-232 (1949).

3. Cowan, G. R. and Hornig, D. F., Phys. Rev. 75, 1294 (1949).

4. Chen, C. J. and Emrich, R. J., Phys. Fluids 6, 1 (1963).

5. Reynolds, G. T., "A Preliminary Study of Plane Waves Formed by Bursting Diaphragms in a Tube", PSRD Report No. 1519 (1943).

6. Ladenburg, R. W., et al., editors, Vol. 9 of High Speed Aerodynamics and Jet Propulsion (Princeton University Press, Princeton, New Jersey, (1954), p. 26-78.

7. Payman, W., Shepherd, W. F. C., et al., Proc. Ray. Soc. A186, 293 (1946).

8. Kovasznay, L. S. G., Rev. Sci. Instr. 20, 696 (1949).

9. Hollyer, Jr., R. N., Hunting, A. C., Laporte, O., Schwarcz, E. H., and Turner, E. B., Phys. Rev. 87, 911 (1952).

10. Resler, E. L., Lin, S. C., and Kantrowitz, A., J. App. Phys. 23, 1390 (1952).

11. Shreffler, G. and Christian, R. H., J. App. Phys. 25, 324 (1954).

12. Turner, E. B., "The Production of Very High Temperature in the Shock Tube with an Application to the Study of Spectral Line Broadening", Ph.D. Thesis, Univeristy of Michigan (1956).

13. Laporte, O., "High Temperature Shock Waves", Combustion and Propulsion, Third AGARD Colloquim (Pergamon Press, New York, 1958), p. 499.

14. Doherty, L. R., "The Measurement of Absolute Spectral Line Strengths with the Shock Tube", Ph.D. Thesis, University of Michigan (1962).

15. Wilkerson, T. D., "The Use of the Shock Tube as a Spectroscopic Source with an Application to the Measurement of gf-Values for Lines of Neutral and Singly Ionized Chromium", Ph.D. Thesis, University of Michigan (1961).

16. Charatis, G., "Shock Tube Determination of Chromium gf-Values", Ph.D. Thesis, University of Michigan (1961).

17. Brown, W. A., "Oscillator Strengths of Lead Spectral Lines: A Shock Tube Measurement", Ph.D. Thesis, University of Michigan (1964).

18. Griem, H. R., Kolb, A. C., and Shen, K. Y., Astrophys. J. (January, 1962) p. 272.

19. Nicholls, R. W., Parkinson, W. H., and Reeves, E. M., Applied Optics 2, 919 (1963).

20. Schardin, H., Physik. Zeitschr. 33, 60 (1932).

21. Bleakney, W. and Emrich, R. J., Sec. J, Vol. 8 of High Speed Aerodynamics and Jet Propulsion (Princeton University Press, Princeton, N. J., 1961), p. 600.

22. Koerniche, E., Zeitschr. Phys. 33, 219 (1925).

23. Fowler, R. G., et al., Phys. Rev. 82, 879 (1951).

24. Kolb, A. C., Phys. Rev. 107, 345 (1957).

25. Koopman, D. W., "Performance Studies and Neon II Line Strength Measurements with an Electrically Driven Shock Tube", Ph. D. Thesis, University of Michigan (1963).

26. Eckerle, K. K. and McWhirter, W. P., Phys. Fluids 9, 81 (1966).

27. Isler, R. C. and Kerr, D. E., Phys. Fluids 8, 1176 (1965); Phys. Fluids 9 1879 (1966).

28. Wiese W., et al, Phys. Fluids 4, 250 (1961).

29. Griem, H. R., Kolb, A. C., and McLean, E. A., Phys. Fluids 9, 628 (1966).

30. Kim, Y. W., "Development of Heated Shock Tube", Final Report to U. S. Air Force Office of Scientific Research, Grant AF-AFOSR-934-66 (1967).

31. Kim, Y. W. and Laporte, O., "Construction of a Shock Tube for Metallic Vapors", 6th International Symposium on Shock Tubes, Freiburg, Germany, March 11-14 (1967).

32. Courant, R. and Frederichs, K. O., Supersonic Flow and Shock Waves Ch. I (Interscience, New York, 1948).

33. Bond, J. W., Phys. Rev. 105, 1683 (1957).

34. Landau, L. D. and Lifshitz, E. M., Statistical Physics Ch. X (Addison-Wesley, Reading, Mass. 1958).

35. Hollyer, Jr., R. N., "A Study of Attenuation in the Shock Tube", Ph.D. Thesis, University of Michigan (1953).

36. Mark, H., J. Aero. Sci. 24, 304 (1957).

37. Strehlow, R. A. and Cohen, A., J. Chem. Phys. 28, 983 (1958).

38. Byron, S. and Rott, N.,"Proceedings of 1961 Heat Transfer and Fluid Mechanics Institute"(Stanford University Press, Stanford, Calif., 1961), p.38.

39. Laporte, O., Unpublished note on "High Temperature Gases", (1955).

40. Petschek, H. E., "Approach to Equilibrium Ionization behind Strong Shock Waves in Argon", Ph.D. Thesis, Cornell University (1955).

41. Harwell, K. E. and Jahn, R. G., Phys. Fluids 7, 214 (1964).

42. Haught, A. F., Phys. Fluids 5, 1337 (1962).

43. Moiseiwitsch, B. L. and Smith, S. J., Rev. Mod. Phys. 40, 238 (1968).

44. Bleakney, W., Phys. Rev. 35, 139 (1930).

45. Schouten, J. W. and Smit, J. A., Physica 10, 661 (1943).

46. Corliss, C. H. and Bozman, W. R., Experimental Transition Probabilities for Spectral Lines of Seventy Elements NBS Monograph 53 (1962).

47. Roth, W. L., J. Am. Chem. Soc. 69, 474 (1947).

48. Long, L. H., Pure and Applied Chem. 2, 62 (1961).

49. Chandraseklar, S., Radiative Transfer (Dover Publications, New York, 1960).

50. Moore, C. E., Vol. III of Atomic Energy Levels NBS Circular 467 (1958).

51. Crosswhite, H. M. and Dieke, G. H., "Simplified Techniques for Calibrating Photographic Emulsions", Bumble Bee Series Report No. 202, Johns Hopkins University (1953).

52. Euler, J., Annalen der Physik 11, 203 (1953).

53. Ferriso, C. C., "Blackbody Radiation Tables", General Dynamics, Space Science Laboratory Report AE62-0862 (1962).

54. Hinnov, E., J. Optic. Soc. 47, 151 (1957).

55. Hinnov, E. and Kohn, H., J. Optic. Soc. 47, 156 (1957).

56. Ladenburg, R. and Wolfsohn, G., Zeitschr. Phys. 63, 616 (1930).

57. Kunze, P., Annalen der Physik 8, 500 (1931).

58. Garstang, R. H., J. Optic. Soc. 52, 845 (1962).

59. Kobzev, G. A. and Norman, G. E., High Temperature 4, 449 (1966).

60. Laporte, O., Private communication (1968).

61. Fermi, E., Zeitschr. Phys. 26, 54 (1924).

62. Mohler, F., Astrophys. J. 90, 429 (1939).

63. Inglis, D. R. and Teller, E., Astrophys. J. 90, 439 (1939).

64. Debye, P. and Hückel, E., Physik. Zeitschr. 24, 187 (1923).

65. Griem, H. R., Phys. Rev., 128, 997 (1962).

66. Ecker, G. and Kröll, W., Phys. Fluids 6, 62 (1963).

67. Cooper, J., editor, "Proceedings of Workshop Conference on the Lowering of the Ionization Potential and Related Problems of the Equilibrium Plasma", JILA Report No. 79, University of Colorado (1966).

68. Hill, T. L., Introduction to Statistical Thermodynamics Ch. II, (Addison-Wesley Publishing Co., Reading, Mass., 1962), p. 33.

69. van der Held, E. M. F., Zeitschr. Phys. 70, 508 (1931).

70. Penner, S. S. and Kavanaugh, R. W., J. Opt. Soc. 43, 385 (1953).

DISTRIBUTION LIST

Dr. Joseph F. Masi
Chief, Propulsion Division (SREP)
Air Force Office of Scientific Research
1400 Wilson Boulevard
Arlington, Virginia 22209 (25 copies)

Prof. Hannes Alfvén
Institutionen for Plasmaphysik
Kungl Telsniska Hagskalan
Stockholm 70, Sweden

Allegany Ballistics Laboratory
ATTN: Librarian
Hercules Powder Company
Cumberland, Maryland 21501

Prof. L. H. Aller
Department of Astronomy
University of California
Los Angeles, California

Dr. Ralph A. Alpher
General Electric Research Laboratory
Schenectady, New York

Dr. J. R. Banister
Sandia Laboratory
Albuquerque, New Mexico

Dr. W. L. Barr
Lawrence Radiation Laboratory
P. O. Box 808
Livermore, California

Dr. S. H. Bauer
Department of Chemistry
Cornell University
Ithaca, New York 14850

Dr. Charles W. Beckett, Jr.
Ass't. Division Chief for Thermodynamics
Heat Division
Room 107, West Building
National Bureau of Standards
Washington, D. C.

Dr. Paul Bender
Department of Chemistry
University of Wisconsin
Madison, Wisconsin 53706

Dr. F. D. Bennett
EBL, Ballistics Research Laboratories
Aberdeen, Maryland

Dr. Peter G. Bergmann
Department of Physics
Syracuse University
Syracuse, New York

Dr. R. S. Berry
Department of Chemistry
University of Chicago
Chicago, Illinois

Dr. Daniel A. Bershader
Department of Aeronautics and
and Astronautics
Stanford University
Palo Alto, California

La Bibliothèque
Centre de Formation en Aérodynamique
Expérimentale
72, Chaussée de Waterloo
Rhode-Saint-Genèse (Bruxelles), Belgique

Prof. Walker Bleakney
Department of Physics
Princeton University
Princeton, New Jersey

Distribution List (Continued)

Dr. J. W. Bond, Jr.
Aerospace Corporation
P. O. Box 95085
Los Angeles, California

Dr. John N. Bradley
Department of Chemistry
University of Essex
Wivenhoe Park
Colchester, Essex, U. K.

Dr. Edward L. Brady
Chief, Office of Standard Reference Data
Adm. A-538
National Bureau of Standards
Washington, D. C. 20234

Dr. J. Brewer
Midwest Research Division
Kansas City, Missouri 64110

Dr. Leo Brewer
Department of Chemistry
University of California
Berkeley, California 94700

Dr. W. A. Brown
52-10
Lockheed Palo Alto Research Lab.
Lockheed Missiles and Space Co.
Palo Alto, California

Dr. Alfred Buchler
Arthur D. Little, Inc.
Acorn Park
Cambridge, Massachusetts 02140

Prof. J. M. Bergers
Institute for Fluid Dynamics and Applied Mathematics
University of Maryland
College Park, Maryland

Dr. S. R. Byron
Applied Research Laboratory
Aeronutronic Division
Ford Motor Company
Newport Beach, California

Dr. Hartwell F. Calcote
AeroChem Research Laboratories, Inc.
P. O. Box 12
Princeton, New Jersey 08540

Dr. T. S. Chang
Box 12447
Raleigh, North Carolina

Dr. J. F. Clarke
Department of Aerodynamics
College of Aeronautics
Cranfield, Bedford, U. K.

Prof. J. L. Climenhaga
Department of Physics
University of Victoria
Victoria, B.C., Canada

Dr. F. H. Coensgen
Lawrence Radiation Laboratory
P. O. Box 808
Livermore, California

Dr. J. Cooper
JILA
University of Colorado
Boulder, Colorado

Dr. C. H. Corliss
National Bureau of Standards
Washington, D. C.

Mr. James P. Coughlin
Dept. 4940, Bldg. 0525
P. O. Box 1947
Aerojet-General Corporation
Sacramento, California 95809

Dr. E. C. Curtis
North American Aviation
Rocketdyne Division
Canoga Park, California 91304

Prof. R. N. Cox
Department of Physics
The City University
St. John Street
London E.C. 1, U. K.

Dr. Lowell R. Doherty
Department of Astronomy
University of Wisconsin
Madison, Wisconsin

Dr. Donald R. Douslin
Petroleum Research Center
U. S. Bureau of Mines
Bartlesville, Oklahoma 74004

Dr. Russell E. Duff
Lawrence Radiation Laboratory
P. O. Box 808
Livermore, California

Prof. E. John Eastmond
Department of Physics
Brigham Young University
Provo, Utah

Prof. B. Edlén
Department of Physics
University of Lund
Lund, Sweden

Dr. G. H. Elste
Department of Astronomy
The University of Michigan
Ann Arbor, Michigan

Prof. Raymond J. Emrich
Department of Physics
Lehigh University
Bethlehem, Pennsylvania

Mr. Milton Farber
Space Sciences, Inc.
1120 S. Gabriel Blvd.
San Gabriel, California 91776

Mr. Ludwig Fasolino
National Research Corporation
70 Memorial Drive
Cambridge, Massachusetts 02142

Dr. R. G. Fowler
Department of Physics
University of Oklahoma
Norman, Oklahoma

Prof. P. A. Franken
Department of Physics
The University of Michigan
Ann Arbor, Michigan

Dr. A. Frohn
Lehrstuhl für Mechanick
Technischen Hochschule Aachen
Aachen, Germany

Prof. W. R. S. Garton
Spectroscopy Department
Imperial College of Science and
Technology
London University
London S. W. 7, U. K.

Prof. A. G. Gaydon
Department of Chemical Engineering and
Chemical Technology
Imperial College
London S. W. 7, U. K.

Prof. Irvine I. Glass
Institute for Aerospace Studies
University of Toronto
Toronto 5, Canada

Dr. Per Gloersen
General Electric Space Sciences Lab.
P. O. Box 8555
Philadelphia, Pennsylvania

Prof. Leo Goldberg
Department of Astronomy
Harvard University
Cambridge, Massachusetts

Mr. Sanford Gordon
Lewis Laboratories (Mail Stop 6-1)
National Aeronautics and Space
Administration
Cleveland, Ohio 44135

Dr. B. Gottlieb
Forrestal Research Center
Princeton University
Princeton, New Jersey

Prof. E. F. Greene
Department of Chemistry
Brown University
Providence 12, Rhode Island

Dr. J. L. Greenstein
Mt. Wilson and Palomar Observatories
California Institute of Technology
Pasadena, California

Prof. H. R. Griem
Department of Physics
University of Maryland
College Park, Maryland

Dr. Philipp Gross
Fulmer Research Institute, Lt'd.
Stoke Poges, Buckinghamshire
England

Dr. R. A. Gross
Department of Engineering
236 Seeley W. Mudd
Columbia University
New York, New York

Guggenheim Aeronautical Laboratory
California Institute of Technology
Pasadena, California

Dr. A. F. Haught
United Aircraft Research Laboratories
400 Main Street
East Hartford, Conn.

Dr. K. E. Harwell
Department of Aerospace Engineering
Auburn University
Auburn, Alabama

Mr. Charles B. Henderson
Atlantic Research Corporation
Shirley Highway at Edsall Road
Alexandria, Virginia 22300

Dr. A. Hertzberg
Cornell Aeronautical Laboratory, Inc.
P. O. Box 235
Buffalo, New York

Dr. Donald L. Hildenbrand
Douglas Advanced Research Lab.
Douglas Aircraft Company
Huntington Beach, California 92646

Dr. R. M. Hill
Department of Atomic Physics
University of Newcastle
Newcastle-on-Tyne, U. K.

Prof. D. W. Holder
Department of Engineering Science
University of Oxford
Parks Road
Oxford, U. K.

Distribution List (Continued)

Dr. N. Hollyer, Jr.
Research Laboratory
General Motors Corporation
Warren, Michigan

Dr. A. C. Hunting
Aerospace Division
Boeing Company
Seattle, Washington

Prof. Isao Imai
Department of Physics
University of Tokyo
Tokyo, Japan

Dr. K. Keith Innes
Department of Chemistry
Vanderbilt University
Nashville, Tennessee 37203

Mr. Roland D. Jackel
Office of Naval Research
Code, 429
Department of the Navy
Washington, D. C. 20360

Dr. R. G. Jahn
Department of Aerospace and
Mechanical Sciences
Princeton University
Princeton, New Jersey 08540

Prof. N. H. Johannesen
Department of the Mechanics of Fluids
University of Manchester
Manchester 13, U. K.

Dr. Walter R. Johnson
Department of Physics
University of Notre Dame
Notre Dame, Indiana 46556

Prof. H. Jones
Department of Mathematics
Imperial College
Exhibition Rd.
London S. W. 7, U. K.

Dr. Arthur Kantrowitz
AVCO-Everett Research Laboratory
2385 Revere Beach Parkway
Everett, Massachusetts 02149

Dr. J. Kaufman
Martin Company
RIAS Division
Baltimore, Maryland 21227

Prof. D. E. Kerr
Department of Physics
Johns Hopkins University
Baltimore, Maryland

Dr. K. G. Kessler
National Bureau of Standards
Washington, D. C. 20234

Dr. Chul Soo Kim
Department of Astronomy and Meteorology
Seoul National University
Seoul, Korea

Prof. R. B. King
Department of Physics
California Institute of Technology
Pasadena, California

Dr. Bennett Kivel
AVCO-Everett Research Laboratory
2385 Revere Beach Parkway
Everett, Massachusetts

Dr. Alan C. Kolb
Center for Plasma Physics
U. S. Naval Research Laboratory
Washington 25, D. C.

Distribution List (Continued)

Dr. D. W. Koopman
Institute for Fluid Dynamics and
Applied Mathematics
University of Maryland
College Park, Maryland

Prof. L. S. G. Kovasznay
Johns Hopkins University
Aeronautics Building
Charles and 34th Streets
Baltimore, Maryland

Prof. Lester Kraus
Department of Electrical Engineering
Drexel Institute of Technology
Philadelphia, Pennsylvania 19104

Prof. A. M. Kuethe
Department of Aerospace Engineering
The University of Michigan
Ann Arbor, Michigan

Prof. P. Kusch
Department of Physics
Columbia University
New York, New York 10027

Dr. M. Lapp
General Electric Research and
Development Center
P. O. Box 8, Bldg. K-1
Schenectady, New York 12301

Prof. W. Leidenfrost
Purdue University
Mechanical Engineering Department
Lafayette, Indiana 47907

Prof. H. W. Liepman
Department of Aeronautics
California Institute of Technology
Pasadena, California

Dr. Shao-Chi Lin
Department of Engineering Physics
University of California at San Diego
P. O. Box 109
La Jolla, California 92038

Dr. M. J. Linevsky
General Electric Company
Missiles and Space Division
Philadelphia, Pennsylvania 19101

Prof. G. M. Lilley
Department of Aeronautics and
Astronautics
The University
Southampton, Hauts., U. K.

Prof. W. Lochte-Holtgreven
Institut für Experimentalphysik
Universität Kiel
Olshausenstrasse 40-60
23 Kiel, Germany

Prof. S. A. B. Luthander
Institionen for Flygteknik
Kungl Tekniska Hagskalan
Stockholm 70, Sweden

Mrs. Mary McCormic
Chemical Propulsion Information Agency
Applied Physics Laboratory
8621 Georgia Avenue
Silver Spring, Maryland 20910

Dr. R. O. MacLaren
United Technology Corporation
Research and Advanced Technology Div.
Sunnyvale, California 94086

Dr. R. W. P. McWhirter
C.T.R. Division, H-7
AERE Harwell
Berkshire, U. K.

Distribution List (Continued)

Dr. David E. Mann
ARPA/BMD
Rm. 2B267, The Pentagon
Washington, D. C. 20301

Prof. H. Margenau
Department of Physics
Yale University
New Haven, Connecticut

Dr. John Margrave
Department of Chemistry
Rice University
Houston, Texas 77001

Dr. C. W. Mautz
General Atomic Division
General Dynamics Corporation
Box 608
San Diego, California

Dr. Walter G. May
Esso Research and Engineering Co.
P. O. Box 8
Linden, New Jersey 07036

Prof. D. H. Menzel
Harvard College Observatory
60 Garden Street
Cambridge, Massachusetts

Dr. Roland E. Meyerott
Physical Science Laboratory
Lockheed Missiles and Space Division
Palo Alto, California

Dr. Thomas A. Milne
Midwest Research Institute
425 Volker Boulevard
Kansas City, Missouri 64110

Dr. E. Montroll
Department of Physics
University of Rochester
Rochester, New York 14627

Dr. Kurt Mueller
Rocketdyne Division of North American Aviation
6633 Canoga Avenue
Canoga Park, California 91303

Mr. John W. Murrin
Bureau of Naval Weapons
Code: RMMP-22
Department of the Navy
Washington, D. C. 20360

Dr. Robert Odom
Propulsion Laboratory
Code: AMSMI-RKC
Army Missile Command
Redstone Arsenal, Alabama 35808

Dr. U. P. Oppenheim
Technion Research and Development Foundation Ltd.
Haifa, Israel

Prof. Donald E. Osterbrock
Washburn Observatory
University of Wisconsin
Madison, Wisconsin

Dr. W. H. Parkinson
Harvard College Observatory
60 Garden Street
Cambridge, Massachusetts

Dr. S. S. Penner
Department of Aerospace and Engineering Sciences
University of California at San Diego
La Jolla, California 92037

Prof. R. W. Perry
Department of Aerospace Engineering
Polytechnique Institute of Brooklyn
Brooklyn, New York 11201

Prof. C. W. Peters
Department of Physics
The University of Michigan
Ann Arbor, Michigan

Dr. H. E. Petschek
AVCO-Everett Research Laboratory
2385 Revere Beach Parkway
Everett, Massachusetts

Dr. J. Pomerantz
Air Force Office of Scientific Research
Arlington, Virginia

Dr. Norman Potter
Aeronutronic Division of Ford Motor Co.
Research Laboratories
Ford Road
Newport Beach, California 92660

Mr. Theodore W. Price
Jet Propulsion Laboratory
4800 Oak Grove Drive
Pasadena, California 91103

Dr. Harold Prophet
Dow Chemical Company
Thermal Laboratory, Bldg. 1707
Midland, Michigan 48640

Dr. E. J. Prosen
Chief, Thermochemistry Section
Chemistry Division
National Bureau of Standards
Washington, D. C. 20234

Dr. George B. Rathmann
Central Research Laboratories
Minnesota Mining and Manufacturing Co.
2301 Hudson Road
St. Paul, Minnesota 55119

Prof. E. L. Resler
Graduate School of Aeronautical
Engineering
Cornell University
Ithaca, New York

Dr. J. R. Roberts
Plasma Spectroscopy Section
National Bureau of Standards
Washington, D. C.

Dr. Mary F. Romig
Rand Corporation
1700 Main Street
Santa Monica, California 90406

Dr. Walter Roth
Xerox Corporation
P. O. Box 1540
Rochester, New York 14603

Dr. Leroy Schieler
Aerospace Corporation
P. O. Box 95085
Los Angeles, California 90045

Scientific and Technical Information
Facility
ATTN: NASA Representative (SAK/DL)
P. O. Box 5700
Bethesda, Maryland 20014 (2 cys)

Dr. D. Schafield
Division of Quantum Meterology
National Physical Laboratory
Teddington, Middlesex, U. K.

Distribution List (Continued)

Dr. F. R. Scott
J. J. Hopkins Laboratory for Pure and Applied Science
General Atomic Division
General Dynamics Corporation
P. O. Box 608
San Diego, California

Mr. Curtis C. Selph
AFRPL (RPCL)
Air Force Systems Command
Edwards, California 93523

Dr. C. Howard Shomate
Physical Chemistry Branch
Research Department (Code 5058)
U. S. Naval Ordnance Test Station
China Lake, California 93557

Prof. K. M. Siegel
Department of Electrical Engineering
The University of Michigan
Ann Arbor, Michigan

Dr. H. A. Skinner
Department of Chemistry
University of Manchester
Manchester 13, England

Dr. M. M. Slawsky
Air Force Office of Scientific Research
Arlington, Virginia

Dr. Z. I. Slawsky
U. S. Naval Ordnance Laboratory
White Oak, Maryland 21503

Prof. A. Slettebak
Department of Astronomy
Ohio State University
Columbus, Ohio

Dr. W. R. Smith
Department of Physics
Lehigh University
Bethlehem, Pennsylvania

Dr. Jean Smolderen
Institute von Karman de Dynanamique des Fluides
72, Chausee de Waterloo
Rhode-Saint-Genese, Belgique

Dr. Alan Snelson
IITRI
10 West 35th Street
Chicago, Illinois 60616

Prof. D. B. Spalding
Department of Heat Transfer and Combustion
Imperial College of Science and Technology
London S. W. 7, U. K.

Dr. Edward A. Spiegel
Department of Physics
New York University
New York, New York 10003

Prof. Lyman Spitzer
Department of Astronomy
Princeton University
Princeton, New Jersey

Dr. G. N. Spokes
Stanford Research Institute
333 Ravenswood Ave.
Menlo Park, California 94025

Dr. David R. Squire
Army Research Office
Box CM, Duke Station
Durham, North Carolina 27706

Prof. R. A. Strehlow
Department of Aeronautical Engineering
University of Illinois
Urbana, Illinois 61601

Prof. B. Strömgren
Astronomy Department
Princeton University
Princeton, New Jersey

Dr. Daniel R. Stull
Thermal Research Laboratory
1707 Building
The Dow Chemical Company
Midland, Michigan 48640 (2 cys)

Dr. Stig Sunner, Director
Thermochemistry Laboratory
Tornavagen 13
Lund, Sweden

Dr. Robert E. Torley
American Cynamid Company
Stamford Research Laboratories
1937 West Main Street
Stamford, Connecticut 06901

Dr. Eugene B. Turner
Aerospace Corporation
P. O. Box 95085
Los Angeles, California

The Library of the Observatory
The University of Michigan
Ann Arbor, Michigan

The Library
United Aircraft Corporation
400 Main Street
East Hartford, Connecticut

Prof. Jacques Valensi
Région Academique d'Aix-Marseille
Institut de Centre d'Universite
1 Rue Honnorat
Marseille-3e, France

Dr. B. Vodar
Laboratoire de Bellevue
CNRS
1 Place A. Briand
92 Bellevue, France

Dr. Guy Waddington
National Academy of Sciences
2101 Constitution Avenue, N. W.
Washington, D. C. 20418

Dr. G. W. Wares
Space Physics Laboratory
Air Force Cambridge Research Lab.
Hanscom Field
Bedford, Massachusetts 01730

Dr. Stewart Way
Westinghouse Research and Development Center
Beulah Road
Pittsburgh, Pennsylvania 15235

Prof. H. D. Weymann
Department of Mechanical and Aerospace Sciences
University of Rochester
Rochester, New York 14627

Dr. E. P. Wheaton
Research and Development Division
Lockheed Missiles and Space Company
Sunnyvale, California 94088

Dr. David White
Department of Chemistry
Ohio State University
Columbus, Ohio 43200

Distribution List (Concluded)

Dr. Donald R. White
Research and Development Center
General Electric Company
Schenectady, New York

Prof. G. B. Whitham
Department of Mathematics
California Institute of Technology
Pasadena, California 91109

Dr. W. L. Wiese
Plasma Spectroscopy Section
National Bureau of Standards
Washington, D. C.

Dr. Stephen S. Wise
United Aircraft Corporation
Research Labs.
400 Main Street
East Hartford, Connecticut 06118

Dr. W. A. Wildhack
National Bureau of Standards
Washington 25, D. C.

Dr. T. D. Wilkerson
Institute for Fluid Dynamics and
Applied Mathematics
University of Maryland
College Park, Maryland

Mr. Jules J. Wittebort
Code: ASRCPT
Thermo-Physics Branch
Directorate of Materials and
Processes, ASD
Wright-Patterson AFB, Ohio 45433

Prof. M. H. Wrubel
Department of Astronomy
Indiana University
Bloomington, Indiana 47401

Dr. Walter Wurster
Cornell Aeronautical Laboratory, Inc.
4455 Genesee St.
Buffalo, New York 14221

Prof. A. D. Young
Department of Engineering
Queen Mary College
Mile End Road
London E. 1, U. K.

Unclassified

Security Classification

DOCUMENT CONTROL DATA - R & D

(Security classification of title, body of abstract and indexing annotation must be entered when the overall report is classified)

1. ORIGINATING ACTIVITY (Corporate author)	2a. REPORT SECURITY CLASSIFICATION
The University of Michigan Ann Arbor, Michigan	Unclassified
	2b. GROUP N/A

3. REPORT TITLE

Ionized Mercury Gas in the Heated Shock Tube: The Measurement of Relaxation Times and Absolute Intensities

4. DESCRIPTIVE NOTES (Type of report and inclusive dates)

Final Report

5. AUTHOR(S) (First name, middle initial, last name)

Yong W. Kim and Otto Laporte

6. REPORT DATE	7a. TOTAL NO. OF PAGES	7b. NO. OF REFS
August, 1968	150	70

8a. CONTRACT OR GRANT NO.	9a. ORIGINATOR'S REPORT NUMBER(S)
Grant No. AF-AFOSR-934-67	
b. PROJECT NO.	01095-1-F
c.	9b. OTHER REPORT NO(S) (Any other numbers that may be assigned this report)
d.	

10. DISTRIBUTION STATEMENT

11. SUPPLEMENTARY NOTES	12. SPONSORING MILITARY ACTIVITY
	AF Office of Scientific Research 1400 Wilson Blvd. Arlington, Virginia 22209

13. ABSTRACT

A heated shock tube has been constructed as a new fluid-dynamical device, in order to study strong shocks in the mercury gas, to investigate the ionizational relaxation phenomenon, and to utilize the shock tube flow as a spectroscopic source.

Extensive theoretical calculations of the Rankine-Hugoniot relation in mercury and mercury-neon mixtures have been performed for a wide range of shock strengths, with various stages of ionization fully taken into account.

A performance study of the heated shock tube has been made. A novel observation of the reflected shock bifurcation in the monatomic gas of mercury has been made, and a detailed quantitative analysis of bifurcated shocks is presented.

The activation energy of ionization in shocked mercury gas is found to coincide with the resonance energy of neutral mercury in the temperature regime of 7,300° to 11,000°K.

The absolute gf-values have been measured in the heated shock tube for 37 neutral mercury lines, using the method of curves of growth.

Related future researches are suggested.

DD FORM 1 NOV 68 1473

Unclassified

Security Classification

14. KEY WORDS	LINK A		LINK B		LINK C	
	ROLE	WT	ROLE	WT	ROLE	WT
Heated shock tube						
Mercury plasma						
Reflected shock bifurcation						
Ionizational relaxation						
Rankine-Hugoniot relation for mercury						
gf-values of HgI lines						